# Linear and non-linear properties of light

Square Gradient Bragg scattering in dielectric waveguides (Part I) and
two-color folded-sandwich entangled photon pair source for quantum teleportation (Part II)

DISSERTATION

zur Erlangung des akademischen Grades
d o c t o r  r e r u m  n a t u r a l i u m
(Dr. rer. nat.)
im Fach Physik

eingereicht am 12. November 2015 an der

Mathematisch-Naturwissenschaftlichen Fakultät
der Humboldt-Universität zu Berlin

von

Dipl.-Phys. Otto Dietz


Präsident der Humboldt-Universität zu Berlin
Prof. Dr. Jan-Hendrik Olbertz

Dekan der Mathematisch Naturwissenschaftlichen Faktultät
Prof. Dr. Elmar Kulke

Gutachter

1. Prof. Dr. Oliver Benson
2. Prof. Achim Peters, PhD
3. Prof. Dr. Wolfram Pernice

Tag der mündlichen Prüfung: 12.02.2016

## Abbreviations

| | |
|---|---|
| APD | single photon avalanche photo diode |
| BS | beam splitter (non-polarizing) |
| CM | curved mirror |
| CW | continuous wave |
| DFG | difference frequency generation |
| DM | dichroic mirror |
| PBS | polarizing beam splitter |
| PEC | perfect electric conductor |
| rms | root mean square |
| SFG | sum frequency generation |
| SGS | square gradient scattering mechanism, see [IMR06] |
| SHG | second harmonic generation |
| SPDC | spontaneous parametric down conversion |
| SST | (Statistical) Surface Scattering Theory, see references in [DSK+12] |
| ppLN | periodically poled $LiNbO_3$ |

# Abstract

Any optical experiment, any optical technology is only about one thing: Manipulating the properties of light through interaction with matter. This thesis will address two important issues in this broad context, in the linear and in the non-linear regime.

In Part I, the well-known Bragg reflection is revised. Bragg reflection takes place whenever light interacts with a periodic structure. The famous Bragg condition relates the lattice spacing in a crystal to the wavelength which is effectively reflected by that lattice. In this thesis the Bragg reflection in dielectric waveguides is investigated. It is shown that the Bragg condition is not sufficient to describe the scattering situation in waveguides with corrugated boundaries. It is demonstrated, analytically and numerically, that corrugated boundaries cause a new type of reflection condition, which goes beyond the Bragg picture. This scattering mechanism, the Square Gradient Bragg Scattering, is known from statistical scattering approaches. It is connected to the curvature of the boundary and has a strong influence on the wave propagation in these systems. Here the first general theory for Square Gradient Bragg Scattering is presented, which allows for making predictions for single corrugated waveguides with arbitrary boundaries.

Another important property of light is investigated in Part II of this thesis: The entanglement of two photons. Entanglement is a counter-intuitive phenomenon, because it has no classical analogy. It especially violates our assumption of local realism, because distant particles seemingly act on each other instantaneously. In this thesis a new tunable and portable source of photon pairs is designed. The photon pairs are created in non-linear crystals, but their entanglement is enforced in a purely geometrical manner. This geometrical approach makes the setup tunable. This is where the new design supersedes its predecessor, which will be discussed in detail. The entanglement of the generated photons is demonstrated experimentally.

# Zusammenfassung

Alle optischen Systeme haben den gleichen Zweck: Sie manipulieren Eigenschaften des Lichts, durch Interaktion mit Materie. In dieser Arbeit werden zwei wichtige Teilaspekte aus diesem Kontext untersucht, im linearen und im nicht-linearen Bereich.

In Teil I werden die bekannten Bragg-Reflexionen in neuem Licht betrachtet. Bragg Reflexion findet statt, wenn Licht mit einem periodischen Medium interagiert. Die Bragg-Bedingung verknüpft den Gitterabstand in einem Kristall mit der Wellenlänge, die von ihm reflektiert wird. In dieser Arbeit werden die Bragg Reflexionen in gewellten Wellenleitern untersucht. Es wird gezeigt, dass die Bragg-Bedingung nicht ausreicht, um die Streuung in diesen Wellenleitern zu verstehen. Es wird numerisch und analytisch demonstriert, dass unebene Ränder eine neue Reflexionsbedingung schaffen, die über das einfache Bragg-Bild hinausgeht. Dieser Streueffekt, der *Square Gradient Bragg*-Mechanismus ist aus statistischen Streuansätzen bekannt. Er hängt mit der Krümmung des Randes zusammen und hat einen starken Einfluss auf die Wellenleitung in diesen Systemen. In dieser Arbeit wird die erste allgemeine Theorie für den *Square Gradient Bragg* Streumechanismus vorgestellt, die es ermöglicht, Voraussagen für einzelne Wellenleiter mit beliebig deformierten Rändern zu treffen.

Eine weitere wichtige Eigenschaft des Lichts wird in Teil II dieser Arbeit untersucht: Die Verschränkung zwischen zwei Photonen. Verschränkung ist ein intuitiv nicht verständliches Phänomen, weil es in der uns umgebenden klassischen Welt kein Analogon hat. Insbesondere verletzt es unsere implizite Annahme eines lokalen Realismus, weil voneinander entfernte Teilchen scheinbar instantan miteinander wechselwirken können. In dieser Arbeit wird eine neue und verstimmbare Quelle für verschränkte Photonen entworfen. Die Photonenpaare werden in nicht-linearen Kristallen erzeugt, aber ihre Verschränkung wird rein geometrisch erzwungen. Dieser geometrische Ansatz erlaubt es, die Frequenz der Photonen einzustellen. Hier übertrifft diese neue Quelle ihre Vorgänger, die ausführlich besprochen werden. Die Verschränkung der erzeugten Photonen wird experimentell nachgewiesen.

# Contents

# 1. Preface to Part I and II

Light-matter interaction is the central theme of this work. It connects the otherwise disjunct topics of this thesis. This preface acts as an overview that aims to locate both topics in the broader research landscape.

Light that passes a dielectric material induces a polarization. That is, negative and positive charges in the material are driven apart. These separated charges change the effective field in the medium. The effective field, the displacement field, is given by

$$D = \epsilon E \tag{1.0.1}$$

where $E$ is the electric, i.e., light, field and $\epsilon = \epsilon_0 \epsilon_r$ is the product of the electric constant and the relative permitivity of the medium.

The first part of this thesis focuses on the effect of a small perturbation of the permitivity $\epsilon$, such that

$$D = (\epsilon + \Delta\epsilon)E \tag{1.0.2}$$

The $\Delta\epsilon E$ is interpreted as new source term. This source term can transfer energy between different modes of the electric field. It is said that $\Delta\epsilon$ couples two modes.

In Part I of this thesis, this coupling mode theory will be used to show that our present picture of wave scattering in corrugated dielectric waveguides is incomplete. The *Square Gradient Bragg* scattering mechanism is derived to complete the picture. This scattering mechanism is known from statistical scattering approaches [IMR06] where it has been derived for ensembles of random systems. Here, a general theory of the Square Gradient Bragg mechanism is proposed, that allows, for the first time, to predict this scattering mechanism in individual systems. It is general in the sense that it is no longer bound to the statistical assumptions of its statistical predecessor. Furthermore, the results of the statistical theory are included in this approach.

So far, scattering in corrugated dielectric waveguides has been intensively studied [YY03]. But studies were restricted to scattering due to lattices. This means that boundary corrugations in waveguides have been regarded as a special kind of lattice scattering effects. These studies did not take into effect the curvature of the boundaries.

In the second part of this thesis, higher order contributions to the polarization will be investigated. The displacement field can be separated into the part that is due to vacuum ($\epsilon_0 E$) and the part that is only due to the material ($\epsilon - \epsilon_0)E$.

$$D = \epsilon_0 E + (\epsilon - \epsilon_0)E \tag{1.0.3}$$
$$= \epsilon_0 E + \epsilon_0(\epsilon_r - 1)E \tag{1.0.4}$$

The constant of the material contribution is called susceptibility $\chi = \epsilon_r - 1$

$$= \epsilon_0 E + \epsilon_0 \chi E \tag{1.0.5}$$

and the entire material contribution is called polarization $P$

$$= \epsilon_0 E + P \tag{1.0.6}$$

In the linear case

$$P = \epsilon_0 \chi E \tag{1.0.7}$$

but with stronger optical fields, higher contributions take effect

$$P = \epsilon_0 \chi E + \epsilon_0 \chi^{(2)} E^2 + \epsilon_0 \chi^{(3)} E^3 + \cdots \tag{1.0.8}$$

The $\chi^{(i)}$ are the non-linear coefficients. The linear polarization can couple modes of the same frequency. The non-linear coefficients are able to mix modes of different frequencies. This effect will be used in Part II to create photon pairs in a non-linear crystal. A special geometry, the *geometrical folded-sandwich*, will yield entangled photons. This source of entangled photons is designed for quantum interface application, where quantum information is communicated between different quantum systems via teleportation.

# Part I.

# Square Gradient Bragg scattering in dielectric waveguides

# 2. Introduction

Wave scattering is a phenomenon which occurs literally everywhere in nature. Understanding the propagation of sea waves or intergalactic gravitational waves entails understanding how scattering influences the transport of these waves. In general, this is a difficult question. Theoretical descriptions exist only for a small number of systems. Regular systems, such as regular lattices are easy to describe, because scattering occurs repeatedly after equal times or distances. In non-regular (or even random) systems the situation is far more complex.

One of the central concepts in wave propagation in periodic systems is Bragg scattering [BB13]. Bragg scattering is mediated by the lattice vector $\beta_{lat}$. It occurs when the longitudinal component of the wave vector of the incident ($\beta_{in}$) and scattered wave ($\beta_{scat}$) fulfill the *Bragg condition*

$$\beta_{in} - \beta_{scat} = m\beta_{lat} \tag{2.0.1}$$

where $m$ denotes the order of the Bragg reflection. In this work the focus will be on waveguide structures with corrugated boundaries as shown in Fig. 2.1. Here, the corrugated boundaries act like a lattice, where scattering takes place. The Bragg scattering in such structures can be calculated in a straightforward manner (e.g., in coupled mode theory [YY03; Kog75]). This work focuses on systems with sinusoidal boundaries, because they are believed to exhibit only a single order Bragg reflection ($m = 1$). The reason for this is that their Fourier series of the sinusoidal boundary consists of only one (positive) coefficient. In Part I of this thesis it is shown that this is not true. It will turn out that even these simple systems feature effects that so far escaped our attention. These effects are easily confused with higher order Bragg resonances. The central question of this part of the thesis is thus: “Is our Bragg scattering picture complete?”.

This question is important, because Bragg scattering serves as starting point for numerical design of variety of optical instruments and optical components in integrated optics [WR90; KSM+15]. But for a numerical design, it is important to know which resonances do, in principle, exist. In this work it will be shown that there are additional

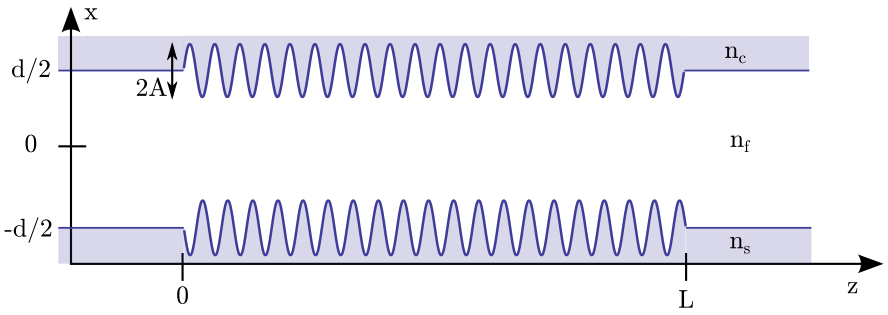


Figure 2.1.: Model of a rough boundary waveguide. The wiggled, rough, boundary profile is given by a normalized, zero-mean profile function $\xi(z)$, such that the boundaries are at $\pm\left(\frac{d}{2} + \sigma\xi(z)\right)$, where $d$ is the mean distance between the boundaries and $\sigma$ is the standard deviation or root mean square (rms) of the boundary.

reflection resonances which were so far unexpected in dielectric waveguides. These resonances are important for many systems in a variety of communities, where corrugated waveguides are employed in very different applications, such as optical filtering [WR90], grating couplers [FKS+74], group-velocity control [TIS+08], phase-matching in nonlinear materials [LZD+14], and distributed feedback laser [KS72].

A statistical approach by Izrailev et al. [IMR06] revealed that for very peculiar systems there exists a new scattering mechanism, the *Square Gradient scattering* mechanism. However, the predictive power of the theory is restricted by strong theoretical assumptions. This new scattering mechanism is by far not as general as ordinary Bragg scattering, due to several problems in the theory. First, it is derived using ensemble averages. This means that it makes predictions for ensembles of systems only. Second, it is only valid for very special boundary functions, namely Gaussian random processes. In previous attempts [DSK+12] to experimentally investigate this theory a lot of effort was made to construct such random-process-like boundary. As a third limitation, the theory is derived for hollow, perfectly electric conducting waveguides only. Last but not least, the derivation is lengthy and complicated, which obscures the physical meaning of the newly derived scattering mechanism.

Summarizing, there are several open questions concerning the Square Gradient scattering, namely: Is this a general mechanism or is it only due to correlations in Gaussian random processes? In other words: Does the mechanism appear in a variety of system, just like Bragg scattering is a universal phenomenon? And, even more basic: What is its relation to Bragg scattering?

The aim of this work is to answer these questions. It will be shown that the Square Gradient scattering mechanism is a general scattering mechanism which is caused by the curvature of arbitrary (as opposed to statistical) boundaries in a variety of systems (as opposed to ensembles of peculiar systems).

It can be derived for boundaries just as Bragg scattering for periodic systems. Therefore throughout this thesis, the mechanism will be called Square Gradient Bragg (SG-Bragg) scattering.

In Part I of this thesis a general theory of SG-Bragg scattering is developed. By applying a coordinate transformation which was successfully used in the statistical approach [IMR06] the results of the statistical approach are recovered in a coupled mode framework. Due to drastically relaxed assumptions about the statistical nature of the boundary the theory presented here covers not only statistically rough surfaces, but arbitrary corrugated boundaries. It is therefore the first general theory of SG-Bragg scattering.

To understand the limitation of the statistical approach, this work will start with an overview of previous statistical work. To pave the way for the coupled mode approach the basic concept of wave propagation in waveguides is introduced in Sec. 4. Under very relaxed theoretical assumptions, the derivation of SG-Bragg scattering will be given in Sec. 5. Special care will be taken to understand why common textbook approaches failed to predict the SG-Bragg scattering mechanism in Sec. 5.2.1. To ensure that SG-Bragg scattering is indeed a generalization of the statistical approach [IMR06], it will be shown that results from the statistical approach follows directly from the coupled mode approach, as a special limiting case in Sec. 5.3.1.

The results of this part of the thesis are reported in [DKN+15] (accepted for publication in Physical Review A).

# 3. Previous work

## 3.1. Statistical approach

The statistical surface scattering theory (SST) was put forward by F.M. Izrailev, N.M. Makarov and M. Rendón in a series of articles [IMR06; RIM07; RMI11; RM12]. To understand the setting in which this theory was developed the concept of localization will be discussed in the following.

Localization is a effect that occurs in random systems. Classical particles that move trough random systems will be scattered back and forth and with certain probability they will reach any place in the system. It is said, they diffuse through the system. P. W. Anderson [And58] noticed that this is not the case for waves that propagate through certain random systems. He found out that the diffusion of the wave comes to hold in one-dimensional (1d) and two-dimensional (2d) systems. The wave is thus localized to a certain domain of the system. This localization is understood as the exponential decay of the wave in space. The transmittance can thus be described by the localization length.

A careful analysis reveals that the localization length depends on the correlation function of the disorder (see Reference in [DKHH+12]). More precisely, it depends on the Fourier transformation of the correlation function of the disorder. This means the correlation of the disorder defines the transmission properties of the system. Thus, the localization length is a function of the wavelength. It is in principle possible to have systems that have very long localization length (they are transparent) at some wavelength, while having vanishing localization length (they are opaque) at other wavelength.

The study of disordered systems started due to the need to understand general features of complex systems. Because of its huge success, it can nowadays be used the other way around. Systems are created with certain random properties to exhibit special effects. For example, recently the (transverse) Anderson localization was used to demonstrate enhanced image transport through a disordered fiber [KFK+14].

The SST describes ensembles of quasi-one-dimensional systems. Mathematically

these systems can be treated as two-dimensional stripes [Duf01]. Such a stripe is shown in Fig. 2.1. The stripe features a wiggled, or rough, profile, denoted by the profile function $\xi(x)$. $\xi$ itself is assumed to be given by a statistically homogeneous and isotropic Gaussian process [RMI11]. This is the first problem of SST. The statistical assumptions about $\xi$ are that strong that it seems impossible to generate systems with desired transmission properties without violating these assumptions. This is one of two major issues that are investigated and resolved in this part of the thesis, later on.

In the following the Fourier transformation $\mathcal{FT}(f)$ is defined in its asymmetric form

$$\mathcal{FT}(f(z)) = \int f(z) \exp(-ikz)\, dz \tag{3.1.1}$$

$$\mathcal{FT}^{-1}(f_k) = \frac{1}{2\pi} \int f_k \exp(ikz)\, dk \tag{3.1.2}$$

and will be abbreviated $\mathcal{FT}(f) = f_k$, if convenient.

The authors of SST derived a relationship between the localization length $L_n^{(loc)}$ and the Fourier transformation of the ensemble averaged correlation function $C$ of the boundary, i.e.,

$$W(k) = \mathcal{FT}(C[\xi]) \tag{3.1.3}$$

Surprisingly they showed that not only the correlation function of the boundary influences the localization length (a fact that is known for simple 1d models already [DKHH+12]). They noticed that the curvature of the boundary enters the localization length as well. They found that the localization length depends not only on $W$, but on the derivative of the profile, $\xi'$, more precisely on

$$S(\beta) = \frac{1}{2}\mathcal{FT}\left(C[\xi'^2] + \mathrm{Var}[\xi'^2]^2\right). \tag{3.1.4}$$

where $\mathrm{Var}[\cdot]$ denotes the variance.

In summary, they derived expression for the localization length $L_n^{(\mathrm{loc})}$ for the $n$'th mode. The localization length is connected to the transmittance (or conductance) of a sample. As discussed above, the localization length is defined as the length scale on which the exponential decay takes place, namely

$$\langle T_n \rangle \sim exp\left(-\alpha L / L_n^{(\mathrm{loc})}\right) \tag{3.1.5}$$

where $\alpha$ is a proportionality factor and $\langle\cdot\rangle$ denotes ensemble averaging.

A huge drawback of the statistical approach is that it is not a priori clear how the ensemble average has to be performed. Two different exponential factors $\alpha$ can arise for different averaging methods. The two averaging procedures discussed in [Bee97] yield the typical transmittance

$$\langle T_n \rangle_{typ} = exp\left(-2L/L_n^{(\mathrm{loc})}\right) \tag{3.1.6}$$

and the average transmittance that differs by a factor of four inside the exponential function

$$\langle T_n \rangle_{avg} \sim exp\left(-L/2L_n^{(\mathrm{loc})}\right) \tag{3.1.7}$$

In theory it is possible to tell apart certain typical realizations from certain average ensembles. But given a real system it is not clear which transmittance gives correct results. Consequently, it is difficult to derive valid predictions for ensembles of systems.

However the promise of a new scattering mechanism should cause sufficient curiosity to take a deeper look into SST. The theory yields expressions for the backscattering length which is connected to the localization length by

$$L_n^{(b)} = \frac{1}{2} L_n^{(\mathrm{loc})}$$

This relation holds for single mode transport without inter-mode scattering. The SST yielded analytical expressions for the backscattering length [RMI11]. It was shown that the backscattering length involves two different contributions,

$$\frac{1}{L_n^{(b)}} = \frac{1}{L_n^{(b),(AS)}} + \frac{1}{L_n^{(b),(SGS)}} \,. \tag{3.1.8}$$

The Amplitude scattering (AS) and the Square Gradient scattering (SGS),

$$\frac{1}{L_n^{(b),(AS)}} = \frac{\sigma^2}{d^6} \frac{4\pi^4 n^4}{\beta_n^2} W(2\beta_n) \tag{3.1.9}$$

$$\frac{1}{L_n^{(b),(SGS)}} = \frac{\sigma^4}{d^4} \frac{(3+\pi^2 n^2)^2}{18\beta_n^2} S(2\beta_n) \tag{3.1.10}$$

where $d$ is the waveguide width (see Fig. 2.1) and $\sigma^2$ is the root mean square (rms) of the boundary, $\beta_n$ is the longitudinal wavevector of the $n$'th mode, i.e., $n$ is the mode number.

The Amplitude scattering mechanism that is known from 1d random samples, has a

direct connection to Bragg scattering. The relationship between Amplitude scattering and Bragg scattering is very carefully discussed by S. John [Joh87; Joh91]. Note that he used the term localization instead of Amplitude scattering, because further contributions to the localization length (like SGS) were unknown at that time. The term Bragg scattering is used for sharp reflection resonances, which are forbidden (transmission) energy levels, comparable to band gaps in solid state. These sharp resonances exist only in non-random infinite samples. As soon as there is randomness, or the sample becomes finite, the Bragg resonances smear out. The resonances cease to be sharp and become pseudo gaps that are populated by localized states. This transition can be seen directly from the theory derived in this part of the thesis.

Two problems of SST have been raised in this introduction. The first problem are the statistical assumptions about the disorder. The second problem is that the theory involves ensemble averages. Both problems are connected, since the ensemble averages are made over ensembles that share the same statistical features. In the next section this problem will be discussed in detail, and a possible solution will be sketched.

## 3.2. From statistical ensembles to single realizations

The correlation function of a homogeneous function $f$ is defined as

$$C[f](z) = \langle f(0)f(z)\rangle \tag{3.2.1}$$

Here, the $\langle . \rangle$ denotes statistical averaging over different realization of $f(z)$. Does this mean that the features of the SGS term do only appear in ensembles of systems? One could object that for sufficient length the samples become ergodic, so that the ensemble average can be replaced by an average over a single sample. However, this implies that with growing length the sample does not change its statistical properties. This again is an assumption that is often fulfilled for random samples only.

In a single system the Wiener-Khinchin theorem [Wei] connects the Fourier transformation of a correlation function to the power spectrum of it's underlying function, such that

$$\mathcal{FT}\left(C_f\right) = |f_k|^2 \tag{3.2.2}$$

With this relationship, one could try to express Eq. (3.1.3) as

$$W(\beta) = |\xi_k|^2 \tag{3.2.3}$$

which would then be a expression for $W$ for a single system. And indeed the power spectrum $|\xi_k|^2$ was shown to cause localization in single systems [DKS+11]. Having used this non-stringent transition from statistical ensembles to single systems it is tempting to imagine the same for the SGS mechanism. It is thus plausible to expect the SGS mechanism to influence single systems as well. In this thesis a stringent derivation of the single system SGS mechanism will be provided in Sec. 5. To see how a expression for a single system could look like, the SGS term will now be further simplified.

The SGS-Term $S(\beta)$ involves the correlation function of the square of the derivative of the boundary function $\xi'^2$. The variance, Var$[f]$, is defined as the mean of square minus mean squared

$$Var[f] = \frac{1}{L}\int_0^L f(x)^2 dx - \left(\frac{1}{L}\int_0^L f(x)dx\right)^2 \tag{3.2.4}$$

The Variance of $\xi'^2$ is constant, and thus it's Fourier transform is a $\delta$-function centered at $k = 0$.

It was shown in [DSK+12] that SGS leads to broad and strong scattering at $k = 0$, even when neglecting the variance. Therefore additional $\delta$-like contributions to the localization length will be negligible. Thus Eq. (3.1.4) can be approximated as

$$S(k) = \frac{1}{2}\mathcal{FT}\left(C[\xi'^2]\right) + \frac{1}{2}\mathcal{FT}\left(\text{Var}[\xi'^2]^2\right) \tag{3.2.5}$$

$$= \frac{1}{2}\mathcal{FT}\left(C[\xi'^2]\right) + \delta(k)\ldots \tag{3.2.6}$$

$$\approx \frac{1}{2}\mathcal{FT}\left(C[\xi'^2]\right) \tag{3.2.7}$$

When replacing the ensemble correlation function with the correlation function of a single sample, the Wiener-Khinchin theorem can again be applied

$$S(k) = \frac{1}{2}\mathcal{FT}\left(C[\xi'^2]\right) \tag{3.2.8}$$

$$= \frac{1}{2}|\mathcal{FT}\left(\xi'^2\right)|^2 \tag{3.2.9}$$

Eq. (3.2.3) and Eq. (3.2.9) are the single system variant of Eq. (3.1.3) and Eq. (3.1.4), respectively. This shows what expression one might expect, when deriving a theory for single systems. The transition from statistical ensembles to single systems sketched in this section suggests that it is worthwhile to explore the influence of the Square

Gradient Scattering mechanism in single systems. This is, to translate the findings for random ensembles to arbitrary, individual, “real world” systems.

# 4. Modes in waveguides

There are waveguides for many different waves, such as visible light waves, microwaves, sound waves, and water waves. Each kind of wave is investigated by its own community, even though the physical phenomenon can be very similar. This is due to the similarity in the underlying wave equation. For microwaves and light, the equation is in fact the same, because these waves are electromagnetic radiation described by the Maxwell's equations. For systems with less than three dimensions, i.e., thin films or narrow waveguides, there is even an equivalence between the electromagnetic wave equation and the Schrödinger equation [Stö10]. This means that findings for the electromagnetic wave equation hold for light, microwaves and even single-particle matter waves.

Under two assumptions the wave equation follows from the source-free (electric current density $J = 0$ and electric charge density $\rho = 0$) Maxwell's equations

$$\nabla \times E = -\frac{\partial}{\partial t} B = -\mu \frac{\partial}{\partial t} H \tag{4.0.1}$$

$$\nabla \times H = \frac{\partial}{\partial t} D = \epsilon \frac{\partial}{\partial t} E \tag{4.0.2}$$

$$\nabla \cdot D = 0 \tag{4.0.3}$$

$$\nabla \cdot B = 0 \tag{4.0.4}$$

$$\tag{4.0.5}$$

where $E, H, D$ and $B$ are functions of time $t$ and space $x, y, z$. In the following optical frequencies are considered and thus the permiability $\mu$ is approximately $\mu_0$.

The first assumption is, that the electric field is only transversal. That is, it consists only of TE-modes such that $E_x = E_z = 0$.

The second assumption is, that the electric and magnetic field are harmonic in time,

i.e.

$$E(r,t) = E(r)\exp(-i\omega t) \tag{4.0.6}$$

$$H(r,t) = H(r)\exp(-i\omega t) \tag{4.0.7}$$

Under these assumptions, the first Maxwell's equation reads

$$\nabla \times E = i\omega\mu H \tag{4.0.8}$$

a vector equation of which the $x$-component reads

$$\underbrace{\frac{\partial E_z}{\partial y}}_{=0} - \frac{\partial E_y}{\partial z} = i\omega\mu H_x \tag{4.0.9}$$

whose $z$-component is

$$\frac{\partial E_y}{\partial x} - \underbrace{\frac{\partial E_x}{\partial y}}_{=0} = i\omega\mu H_z \tag{4.0.10}$$

The second Maxwell's equation becomes

$$\nabla \times H = -i\omega\epsilon E \tag{4.0.11}$$

whose $y$-component is

$$\frac{\partial H_x}{\partial z} - \frac{\partial H_z}{\partial x} = -i\omega\epsilon E_y \tag{4.0.12}$$

Using $H_x$ from (4.0.9) and $H_z$ from (4.0.10) to substitute $H_x$ and $H_z$ in (4.0.12) yields

$$\left(\frac{\partial^2}{\partial x^2} + \frac{\partial^2}{\partial z^2}\right) E_y = -\omega^2\mu\epsilon E_y \tag{4.0.13}$$

In the case of a waveguide that is homogenous in $y$-direction, i.e. $\frac{\partial}{\partial y} = 0$ this can be written as

$$\left(\nabla^2 + \omega^2\mu\epsilon\right) E_y = 0 \tag{4.0.14}$$

## 4.1. Modes in hollow, perfectly electrically conducting (PEC) waveguides

The attenuation of modes in the waveguide is described as a function depending on the longitudinal wave vector. This longitudinal wave vector has different names in different communities. Here, the nomenclature of the dielectric waveguide community is adopted, thus the longitudinal wave vector is called $\beta$. This $\beta$ it is often referred to as the propagation constant. In the PEC-communities, the longitudinal wave vector is mostly written as the longitudinal component $k_{\parallel}$ of the wave vector $\vec{k}$. For a waveguide of refractive index $n_f$ with perfectly reflecting walls, $\beta$ is a simple function of $|\vec{k}|$, since $k_{\perp} = \frac{\pi m}{d}$ is simply a constant and thus

$$\beta = \sqrt{n_f^2 |\vec{k}|^2 - \left(\frac{\pi m}{d}\right)^2}. \tag{4.1.1}$$

$\beta$ can take any value from 0 to $\infty$. This means that $\vec{k}$ can have any orientation from transversal to nearly longitudinal. For any orientation the incident wave will be reflected, as depicted in Fig. 4.1 a). The mode in PEC waveguides will be zero at the boundaries, since they are conducting. The field vanishes everywhere ($E_m = 0$ in Eq. (4.2.14)) except inside the waveguide, between $x = -d/2$ and $x = d/2$

$$E_m = N \begin{cases} \cos\left(\frac{\pi m}{d}\right) & \text{for odd } m \\ \sin\left(\frac{\pi m}{d}\right) & \text{for even } m \end{cases} \tag{4.1.2}$$

with $N$ being the normalization, which will be discussed further below.

## 4.2. Modes in dielectric waveguides

In Fig. 4.1 b) the situation is different, there is no guided mode, i.e., no reflection of the incident wave for $\beta$ which are below the critical angle of internal reflection. However, for $\beta$ big enough to surmount the critical angle there will be a guided mode, as shown in Fig. 4.1 c). Obviously the behavior of the mode, i.e., the functional relationship between $|\vec{k}|$ and $\beta$, is quite different. In this section an expression similar to (4.1.1) will be derived for dielectric waveguides.

Let the amplitude of the reflected TE wave $E_r$ be given by [Ebe92]

$$E_r = E_i \exp(2i\Phi) \tag{4.2.1}$$

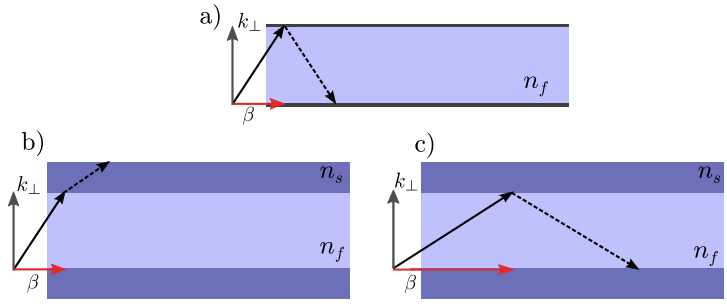


Figure 4.1.: Difference of guiding between dielectric and PEC waveguide. a) In the PEC case, the walls are reflecting ('hard walls'). Incident waves of any $\beta$ are reflected further into the waveguide, i.e., they are guided modes. b) Dielectric waveguides ($n_s < n_f$) will not reflect incident waves that are below the critical angle for internal reflection. c) Only waves above a certain angle will be reflected, and thus be guided.

where, $\Phi$ is given by

$$\Phi = \arctan \frac{\sqrt{n_f^2 \sin^2 \Theta_i - n_s^2}}{n_f \cos \Theta_i} \tag{4.2.2}$$

The angle $\Theta$ is the angle between $\vec{k}$ and the $k_y$-direction. The refractive indices $n_f$ and $n_s$ refers to waveguide and substrate, respectively. After reflection at the upper surface, as in Fig. 4.1 (c), the wave will be reflected at the lower surface (at distance $d$), accumulating another phase shift $\Phi$. For a guided mode this phase shift has to be a multiple of $2\pi$, yielding the condition (see Eq. (3.6) in [Ebe92])

$$2|\vec{k}|n_f d \cos \Theta - 4\Phi = 2\pi m, \tag{4.2.3}$$

Transversal propagation $\kappa$ and decay constants $\gamma$ can be defined to ease notation [Kog75].

$$\kappa_f^2 = n_f^2 k^2 - \beta^2 \tag{4.2.4}$$

$$\kappa_s^2 = n_s^2 k^2 - \beta^2 = -\gamma_s^2 \tag{4.2.5}$$

Note that $\kappa_{f/s}$ is the redefinition of $n_{f/s} k_\perp$. Therefore, it is not surprising that $\beta$ and $\kappa_{f/s}$ are perpendicular, when understood as elements of the wave vector, with

$$\kappa_f = k n_f \cos \Theta \tag{4.2.6}$$

$$\beta = k n_f \sin \Theta \tag{4.2.7}$$

Using these relationships (4.2.2) becomes

$$\Phi = \arctan \sqrt{\frac{1 - \left(\frac{n_s}{n_{eff}}\right)^2}{\left(\frac{n_f}{n_{eff}}\right)^2 - 1}} \tag{4.2.8}$$

and $\beta$, which is $\beta = \sqrt{n_f^2 k^2 - \kappa_f^2}$ can be combined with Eq. (4.2.3) yielding

$$\beta = \sqrt{n_f^2 k^2 - \left(\frac{\pi m + 2\Phi}{d}\right)^2}. \tag{4.2.9}$$

The propagation 'constant' $\beta$ is used to define the effective index of refraction $n_{eff} = \beta/|\vec{k}|$. The guided mode propagates as in a medium with refractive index $n_{eff}$. Comparing this result for $\beta$ and the definition of $\beta$ in the PEC case in Eq. (4.1.1) one notices that they are the same for $n_f = 1$ and $\Phi = 0$.

As indicated before, there are only certain allowed values for $\beta$. These can be found by plugging Eq. (4.2.2) into Eq. (4.2.3), which yields

$$2d\kappa_f - 4 \arctan \sqrt{\frac{1 - \left(\frac{n_s}{n_{eff}}\right)^2}{\left(\frac{n_f}{n_{eff}}\right)^2 - 1}} = 2\pi m \tag{4.2.10}$$

Solving this equation numerically yields the allowed $\beta$ for each mode $m$. These are denoted by $\beta_m$, the allowed modes in the dielectric waveguides. Fig. 4.2 shows a comparison of the first three modes for a dielectric and a PEC waveguide. It is apparent from the figure that $\beta$ for the dielectric waveguide is bound to $kn_s < \beta < kn_f$. In the PEC, $\beta$ is bound to $0 < \beta < k$. This is exactly what was expected and discussed in Fig. 4.1

Note that these results hold for the symmetric waveguide, where substrate and cover are the same. In the asymmetric case Eq. (4.2.3) changes to

$$2kn_f d \cos\Theta - 2\Phi_c - 2\Phi_s = 2\pi m \tag{4.2.11}$$

due to the different phase shifts $\Phi_c$ and $\Phi_s$ at the cover and the substrate interface, respectively. For simplicity a symmetric waveguide is assumed if not stated differently. The mode in the dielectric waveguide leaks into the substrate, where it decays

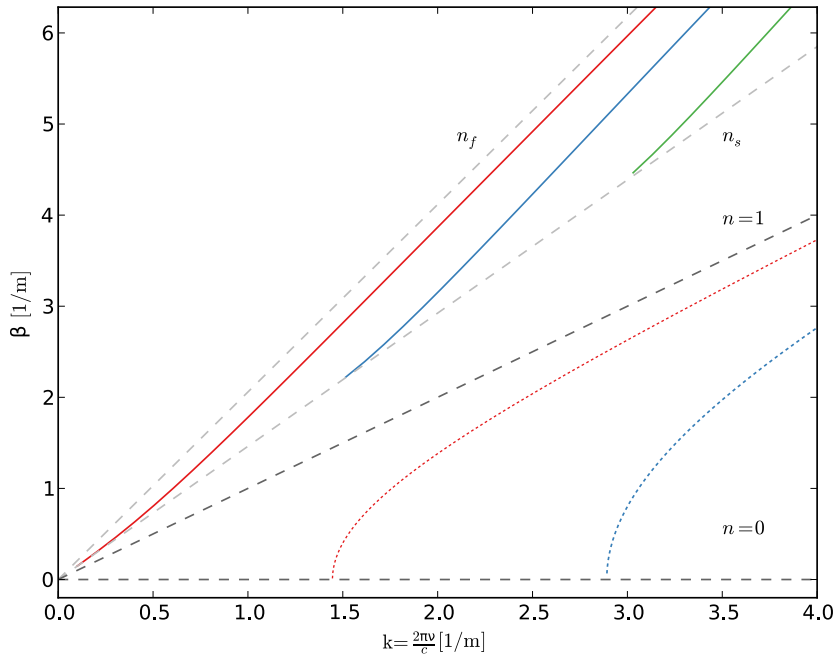


Figure 4.2.: First modes $m = 1$ (red, ——), $m = 2$ (blue, ——), $m = 3$ (green, ——) for a dielectric (solid) waveguide and a PEC-waveguide (dashed). The dielectric modes are between the gray dashed lines $\beta = kn_{f/s}$ that indicate the refractive indices for the film (inner) ($n_f = 1.46$) and the substrate (outer) ($n_s = 2.05$) material. The PEC modes are between the gray dashed line $\beta = kn$, for $n = 1$ (air) and the (unphysical) $n = 0$ line. The $n = 0$ refractive index is displayed to point out that it is a lower bound just as $n_s$. The width of both waveguides is $d = 1.5\mu$m (compare geometry of the sample with Fig. 2.1 for the case of $\sigma = 0$, i.e., no boundary corrugation).

exponentially:

$$E_m = E_s \exp\left(\gamma_s \left(x + \frac{d}{2}\right)\right) \qquad \text{for } x \leq -d/2 \tag{4.2.12}$$

$$E_m = E_s \exp\left(-\gamma_s \left(x - \frac{d}{2}\right)\right) \qquad \text{for } x \geq d/2 \tag{4.2.13}$$

Within the film it is, as in the PEC waveguide, given by a Sine or Cosine.

$$E_m = E_f \begin{cases} \cos(\kappa_f x) & \text{for odd } m \\ \sin(\kappa_f x) & \text{for even } m \end{cases} \qquad \text{for } -d/2 < x < d/2 \tag{4.2.14}$$

The mode is continuous across the interface, as depicted in Fig. 4.3. Therefore the amplitudes are connected by

$$E_f^2(n_f^2 - n_{eff}^2) = E_s^2(n_f^2 - n_s^2) \tag{4.2.15}$$

or in terms of the propagation constants

$$E_f^2\kappa_f^2 = E_s^2(\kappa_f^2 + \gamma_s^2) \tag{4.2.16}$$

While $E_s$ can be derived from $E_f$ for given $n_s, n_f, n_{eff}$, the value of $E_f$ can be chosen arbitrarily. It is convenient to normalize $E_f$ in such a way that the power flow per unit width is 1 W/m

$$P = \frac{2}{u}\int_{-\infty}^{\infty} dx E_y H_x^* \stackrel{!}{=} 1 \text{ W/m} \tag{4.2.17}$$

Where $E_y$ is the entire mode, as defined in Eq. (4.2.14), constructed piecewise from the $E_s$ and $E_f$. The normalization $u$ was introduced to account for different normalizations used in the literature, ranging from $u = 1$ [Kog75] to $u = 4$ [YY03]. For TE modes it follows from the Maxwell's equation 4.0.1 that

$$H_x = -\frac{\beta}{\omega\mu} E_y \tag{4.2.18}$$

and thus

$$\frac{2\beta}{u\omega\mu}\int dx E_y^2 = 1 \text{ W/m} \tag{4.2.19}$$

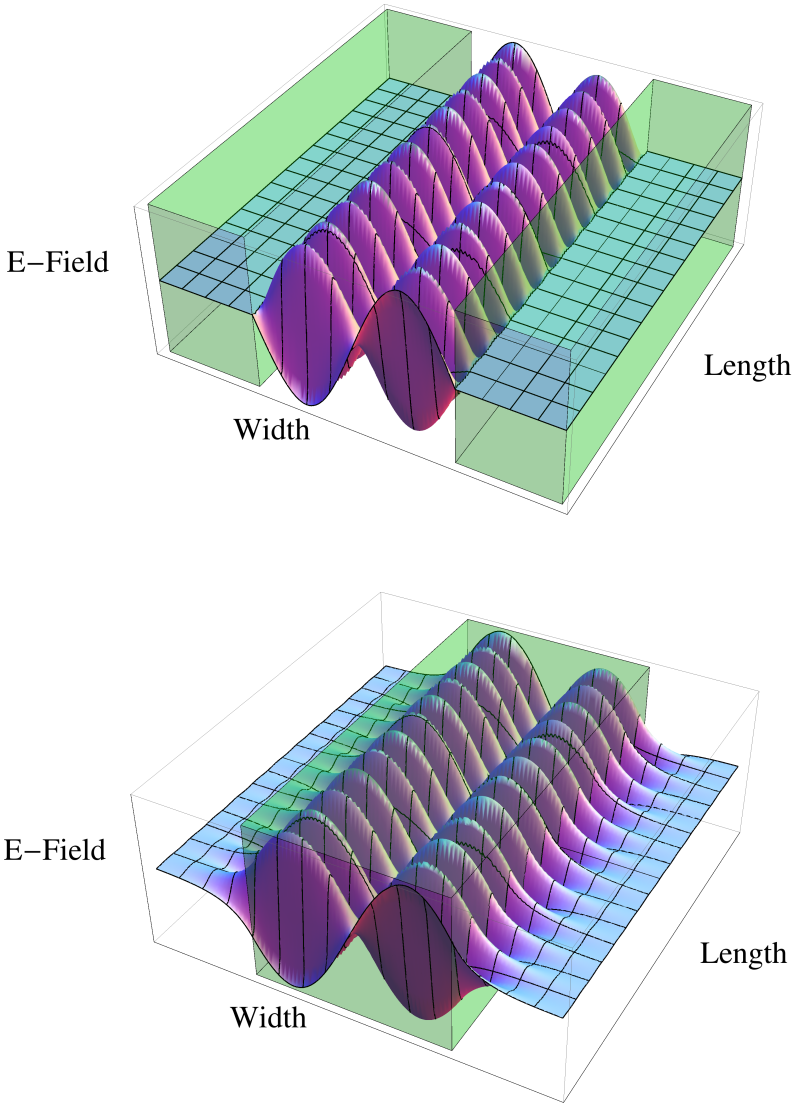


Figure 4.3.: Second Mode in PEC (upper) and dielectric waveguide (lower), with arbitrary dimensions. The opaque green box indicates the material of higher contrast. In the upper panel this is the conducting wall of the hollow PEC waveguide, where the E-Field vanishes at the boundaries. In the lower panel, it indicates the dielectric material of the waveguide. Here, the wave is guided by the material, but can penetrate into the outer, lower contrast material.

Solving this integral with the appropriate mode $E_y$ yields the normalization for the two different fields

$$\frac{2\beta}{u\omega\mu}\frac{1}{2}\left(E_f^2\left(d \pm \frac{\sin(d\kappa_f)}{\kappa_f}\right) + E_s^2\frac{2}{\gamma_s}\right) = 1 \text{ W/m} \tag{4.2.20}$$

Using the relationship Eq. (4.2.16) of $E_f$ and $E_s$ it follows that

$$E_f^2 = \frac{u\omega\mu}{\beta}\left(d \pm \frac{\sin(d\kappa_f)}{\kappa_f} + \frac{n_f^2 - n_{eff}^2}{n_f^2 - n_c^2}\frac{2}{\gamma_s}\right)^{-1} \text{ W/m} \tag{4.2.21}$$

In the same manner the normalization for the PEC waveguide is calculated

$$\frac{2\beta}{u\omega\mu}\int dx E_y^2 = 1 \text{ W/m} \tag{4.2.22}$$

$$\frac{2\beta}{u\omega\mu}\frac{1}{2}E_f^2 d = 1 \text{ W/m} \tag{4.2.23}$$

which yields $N^2 = E_f^2 = \frac{u\omega\mu}{\beta d}$ W/m. Here, only non-magnetic materials are considered, therefore $\mu = \mu_0$. For the PEC waveguide (filled with air), the refractive index is a constant $n = 1$ and therefore $\epsilon = \epsilon_0$. Thus for the PEC one can write

$$E_f^2 = \frac{p\mu\omega}{\beta d}\text{W/m} = p\sqrt{\frac{\mu_0}{\epsilon_0}}\frac{1}{n_{eff}d}\text{W/m} \tag{4.2.24}$$

For dielectric waveguides the normalization Eq. (4.2.21) is sometimes [Kog75] approximated by assuming $\epsilon_0 = \epsilon$ and $E_f \approx E_s$using $d_{eff} = d + \frac{2}{\gamma_c}$as

$$E_f^2 = \frac{u\omega\mu}{\beta d_{eff}}\text{W/m} = p\sqrt{\frac{\mu_0}{\epsilon_0}}\frac{1}{n_{eff}d_{eff}}\text{W/m} \tag{4.2.25}$$

This approximation is especially useful in high contrast waveguides and whenever the guided mode is well confined inside the dielectric waveguide. It shows the similarity between guided modes in PEC and dielectric waveguide. However, throughout this work the proper normalization Eq. (4.2.21) is used.

# 5. Coupled mode approach

In this section a general derivation of the Square Gradient (SG) Bragg scattering mechanism is presented. The boundary disorder will be treated within the coupled-mode framework. At first the concepts of the coupled-mode approach is explained. Then, a text-book [YY03] approach for rough boundaries is investigated. It will turn out that this approach yield Bragg scattering, but fails to come up with the SG-Bragg contribution. The results of this chapter are described in [DKN+15] (accepted for publication at Physical Review A).

## 5.1. Coupled mode basics

Starting from the wave Eq. (4.0.14) for an unperturbed dielectric waveguide, derived in [YY03],

$$\left[\nabla^2 + \omega^2\mu\epsilon\right] E_l(x,y)e^{i(\omega t-\beta_l z)} = 0 \tag{5.1.1}$$

one can treat small disorder with a perturbation approach, such that the entire boundary perturbation is modeled as a change of the dielectric function $\epsilon_0(x,y)$. The dielectric functions (which includes the dielectric constant $\epsilon_0$) defines the dielectric waveguide without boundary corrugation, i.e., $\sigma = A = 0$ in Fig. 2.1. The boundary corrugation now enters the equation as $\Delta\epsilon(x,y,z)$,

$$\left[\nabla^2 + \omega^2\mu(\epsilon_0(x,y) + \Delta\epsilon(x,y,z))\right] E(x,y,z) = 0. \tag{5.1.2}$$

The fields $E$ are no longer solutions of the Maxwell's equations for the unperturbed waveguide, but can be expressed as a linear combination of those

$$E = \sum_l A_l(z)E_l(x,y)e^{i(\omega t-\beta_l z)} \tag{5.1.3}$$

Inserting Eq. (5.1.3) into Eq. (5.1.2), and applying Eq. (5.1.1) yields

$$\sum_l \left[\frac{d^2}{dz^2}A_l - 2i\beta_l\frac{d}{dz}A_l\right] E_l(x,y)e^{-i\beta_l z} = -\omega^2\mu\sum_l A_l\Delta\epsilon E_l(x,y)e^{-i\beta_l z}. \tag{5.1.4}$$

Note that left hand side and right hand side have been separated to emphasize that the term $\sim \Delta\epsilon E_l = \Delta P$ is identified as the perturbation polarization. This means the dielectric perturbation is interpreted as a source term. The physical meaning is that the coupling between two different modes ($k$ and $l$, see below) is mediated by the dielectric perturbation $\Delta\epsilon$.

Assuming that the changes in the amplitudes are slow enough, such that $\frac{d^2}{dz^2}A_l << 2\beta_l \frac{d}{dz}A_l$, the first term can be neglected. Multiplying $\int dxdyE_k^*$ from the right and using the orthogonality $\int dxdyE_k^* E_l = \delta_{km}\frac{n\omega\mu}{2|\beta_k|}$ (compare Eq. (4.2.19)) yields

$$\sum_l -\frac{u\omega\mu}{2|\beta_k|}\delta_{km} 2i\beta_l \frac{d}{dz}A_l e^{-i\beta_l z} = -\omega^2\mu \sum_l \Delta\epsilon A_l E_l(x,y) e^{-i\beta_l z} \tag{5.1.5}$$

This simplifies to

$$\frac{d}{dz}A_k = -i\frac{\beta_k}{|\beta_k|}\sum_l C_{kl} A_l e^{i(\beta_k-\beta_l)z} \tag{5.1.6}$$

The coupling coefficient is

$$C_{kl} = \frac{\omega}{u}\int dxdy E_k \Delta\epsilon E_l \tag{5.1.7}$$

At this point the derivation in many textbooks [YY03; Ebe92; Kog75] continues with the Fourier expansion of $\Delta\epsilon$. This is assuming a infinite periodic perturbation. In this case the perturbation can be written as

$$\Delta\epsilon = \sum_{m\neq 0} \epsilon_m(x,y) e^{-im\frac{2\pi}{\Lambda}z} \tag{5.1.8}$$

However, the perturbation is only integrated perpendicular to the direction of propagation. This means that the coupling is calculated for slices of the waveguide. Formally this can be done with step like boundaries [YY03] or sinusoidal disorder [Ebe92; Kog75]. Unfortunately this means that all these different types of disorders are approximated slicewise, i.e., as stratified disorder only.

## 5.2. Beyond stratified perturbation: Coupled mode theory for boundary perturbation

The perturbation $\Delta\epsilon$ for a waveguide of width $w(z)$ ($\langle w \rangle = d$) with refractive index of $n_f$ in a substrate with refractive index $n_s$ is often [YY03; Ebe92; Kog75] given in the following way

$$\Delta\epsilon = \begin{cases} n_f^2 - n_s^2 & , w(z) > x > d \\ n_s^2 - n_f^2 & , w(z) < x < d \end{cases} \tag{5.2.1}$$

In this form $\Delta\epsilon$ is difficult to expand into a Fourier series. However, a coordinate transformation allows one to obtain a closed form for $\Delta\epsilon$. The coordinate transformation is

$$(x, y, z) \rightarrow (\frac{w(\tilde{z})}{d}\tilde{x}, \tilde{y}, \tilde{z}) \tag{5.2.2}$$

where $w(\tilde{z}) = d + 2\sigma\xi(\tilde{z})$ is the width of the waveguide, and $\xi$ the boundary roughness function as shown in Fig. 2.1. It transforms the waveguide in such a way that the interface is flat at $\tilde{x} = d$. This is a transformation very similar to the transformation used in [IMR06]. When transforming

$$\left[\nabla^2 + \omega^2\mu\left(\epsilon_0(x, y) + \Delta\epsilon(x, y, z)\right)\right] E(x, y, z) = 0 \tag{5.2.3}$$

the perturbation $\Delta\epsilon$ vanishes, due to the flattened interface:

$$\left[\widetilde{\nabla}^2 + \omega^2\mu\tilde{\epsilon}_0(\tilde{x}, \tilde{y})\right] E(\tilde{x}, \tilde{y}, \tilde{z}) = 0 \tag{5.2.4}$$

However the Laplacian contains additional terms. These additional terms are derived in the following. For some function $f(\tilde{x}, \tilde{y}, \tilde{z})$ one obtains (with auxiliary labels $A$ and $B$)

$$\frac{\partial}{\partial x}f = \left(\frac{\partial\tilde{x}}{\partial x}\frac{\partial}{\partial\tilde{x}} + \frac{\partial\tilde{y}}{\partial x}\frac{\partial}{\partial\tilde{y}} + \frac{\partial\tilde{z}}{\partial x}\frac{\partial}{\partial\tilde{z}}\right)f = \left(\frac{\partial\tilde{x}}{\partial x}\frac{\partial}{\partial\tilde{x}}\right)f = \frac{d}{w}\frac{\partial}{\partial\tilde{x}}f \tag{5.2.5}$$

$$\frac{\partial}{\partial y}f = \left(\frac{\partial\tilde{x}}{\partial y}\frac{\partial}{\partial\tilde{x}} + \frac{\partial\tilde{y}}{\partial y}\frac{\partial}{\partial\tilde{y}} + \frac{\partial\tilde{z}}{\partial y}\frac{\partial}{\partial\tilde{z}}\right)f = \frac{\partial}{\partial\tilde{y}}f \tag{5.2.6}$$

$$\frac{\partial}{\partial z}f = \left(\frac{\partial\tilde{x}}{\partial z}\frac{\partial}{\partial\tilde{x}} + \frac{\partial\tilde{y}}{\partial z}\frac{\partial}{\partial\tilde{y}} + \frac{\partial\tilde{z}}{\partial z}\frac{\partial}{\partial\tilde{z}}\right)f = \left(\frac{\partial\tilde{x}}{\partial z}\frac{\partial}{\partial\tilde{x}} + \frac{\partial}{\partial\tilde{z}}\right)f \tag{5.2.7}$$

$$= \left(\frac{dx\sigma}{-w(\tilde{z})^2}\frac{\partial\xi}{\partial\tilde{z}}\frac{\partial}{\partial\tilde{x}} + \frac{\partial}{\partial\tilde{z}}\right)f = \left(\underbrace{\tilde{x}\frac{\sigma}{-w(\tilde{z})}\frac{\partial\xi}{\partial\tilde{z}}\frac{\partial}{\partial\tilde{x}}}_{A} + \underbrace{\frac{\partial}{\partial\tilde{z}}}_{B}\right)f \tag{5.2.8}$$

Applying the derivation twice yields

$$\frac{\partial^2}{\partial x^2}f = \frac{d^2}{w^2}\frac{\partial^2}{\partial\tilde{x}^2}f \tag{5.2.9}$$

$$\frac{\partial^2}{\partial y^2}f = \frac{\partial^2}{\partial\tilde{y}^2}f \tag{5.2.10}$$

$$\frac{\partial^2}{\partial z^2}f = \left(\underbrace{\tilde{x}\frac{\sigma^2}{w^2}\left(\frac{\partial\xi}{\partial\tilde{z}}\right)^2\frac{\partial}{\partial\tilde{x}} + \tilde{x}^2\frac{\sigma^2}{w^2}\left(\frac{\partial\xi}{\partial\tilde{z}}\right)^2\frac{\partial^2}{\partial\tilde{x}^2}}_{A^2} + \underbrace{\frac{\partial^2}{\partial\tilde{z}^2}}_{B^2} + \underbrace{\tilde{x}\frac{\sigma}{-w}\frac{\partial\xi}{\partial\tilde{z}}\frac{\partial}{\partial\tilde{x}}\frac{\partial}{\partial\tilde{z}}}_{AB} + \underbrace{\frac{\partial}{\partial\tilde{z}}\tilde{x}\frac{\sigma}{-w(\tilde{z})}\frac{\partial\xi}{\partial\tilde{z}}\frac{\partial}{\partial\tilde{x}}}_{BA}\right)f \tag{5.2.11}$$

where the last term becomes

$$\frac{\partial}{\partial\tilde{z}}\tilde{x}\frac{\sigma}{-w(\tilde{z})}\frac{\partial\xi}{\partial\tilde{z}}\frac{\partial}{\partial\tilde{x}} \tag{5.2.12}$$

$$= \frac{\tilde{x}\sigma^2}{w^2}\left(\frac{\partial\xi}{\partial\tilde{z}}\right)^2\frac{\partial}{\partial\tilde{x}} + \frac{\tilde{x}\sigma^2}{w^2}\left(\frac{\partial\xi}{\partial\tilde{z}}\right)^2\frac{\partial}{\partial\tilde{x}} + \frac{\tilde{x}\sigma}{-w}\left(\frac{\partial^2\xi}{\partial\tilde{z}^2}\right)\frac{\partial}{\partial\tilde{x}} + \frac{\tilde{x}\sigma}{-w}\frac{\partial\xi}{\partial\tilde{z}}\frac{\partial}{\partial\tilde{z}}\frac{\partial}{\partial\tilde{x}} \tag{5.2.13}$$

Different types of derivatives of $\xi$ appear. Grouping these terms (using square

brackets to denote the index) yields

$$\tilde{\nabla}^2\,[0] = \frac{d^2}{w^2}\frac{\partial^2}{\partial\tilde{x}^2} + \frac{\partial^2}{\partial\tilde{y}^2} + \frac{\partial^2}{\partial\tilde{z}^2} \tag{5.2.14}$$

$$\tilde{\nabla}^2\left[\frac{\partial\xi}{\partial\tilde{z}}\right] = -\frac{\sigma}{w}\frac{\partial\xi}{\partial\tilde{z}}\tilde{x}\frac{\partial}{\partial\tilde{x}}\frac{\partial}{\partial\tilde{z}} - \frac{\sigma}{w}\frac{\partial\xi}{\partial\tilde{z}}\tilde{x}\frac{\partial}{\partial\tilde{z}}\frac{\partial}{\partial\tilde{x}} \tag{5.2.15}$$

$$\tilde{\nabla}^2\left[\left(\frac{\partial\xi}{\partial\tilde{z}}\right)^2\right] = \frac{\sigma^2}{w^2}\left(\frac{\partial\xi}{\partial\tilde{z}}\right)^2 3\tilde{x}\frac{\partial}{\partial\tilde{x}} + \frac{\sigma^2}{w^2}\left(\frac{\partial\xi}{\partial\tilde{z}}\right)^2\tilde{x}^2\frac{\partial^2}{\partial\tilde{x}^2} \tag{5.2.16}$$

$$\tilde{\nabla}^2\left[\frac{\partial^2\xi}{\partial\tilde{z}^2}\right] = -\frac{\sigma}{w}\left(\frac{\partial^2\xi}{\partial\tilde{z}^2}\right)\tilde{x}\frac{\partial}{\partial\tilde{x}} \tag{5.2.17}$$

The entire Laplacian can be rewritten, as indicated above:

$$\tilde{\nabla}^2 = \underbrace{\frac{\partial^2}{\partial\tilde{x}^2} + \frac{\partial^2}{\partial\tilde{y}^2} + \frac{\partial^2}{\partial\tilde{z}^2}}_{\tilde{\nabla}^2_{\mathrm{red}}} + \underbrace{\left(\left(\frac{d^2}{w^2} - 1\right)\frac{\partial^2}{\partial\tilde{x}^2} + \tilde{\nabla}^2\left[\frac{\partial\xi}{\partial\tilde{z}}\right] + \tilde{\nabla}^2\left[\left(\frac{\partial\xi}{\partial\tilde{z}}\right)^2\right] + \tilde{\nabla}^2\left[\frac{\partial^2\xi}{\partial\tilde{z}^2}\right]\right)}_{\omega^2\mu\Delta\tilde{\epsilon}} \tag{5.2.18}$$

These terms will now be interpreted as the new dielectric perturbation $\Delta\tilde{\epsilon}$. Let us write the Laplacian formally as a reduced Laplacian

$$\widetilde{\nabla}^2_{\mathrm{red}} = \frac{\partial^2}{\partial\tilde{x}^2} + \frac{\partial^2}{\partial\tilde{y}^2} + \frac{\partial^2}{\partial\tilde{z}^2} \tag{5.2.19}$$

plus the extra terms $\omega^2\mu\Delta\tilde{\epsilon}$:

$$\widetilde{\nabla}^2 = \widetilde{\nabla}^2_{\mathrm{red}} + \omega^2\mu\Delta\tilde{\epsilon} \tag{5.2.20}$$

yielding

$$\left[\widetilde{\nabla}^2_{\mathrm{red}} + \omega^2\mu\left(\tilde{\epsilon}_0(\tilde{x},\tilde{y}) + \Delta\tilde{\epsilon}\right)\right]E(\tilde{x},\tilde{y},\tilde{z}) = 0 \tag{5.2.21}$$

Where

$$\Delta\tilde{\epsilon} = \frac{1}{\omega^2\mu}\left(\left(\frac{d^2}{w^2} - 1\right)\frac{\partial^2}{\partial\tilde{x}^2} + \tilde{\nabla}^2\left[\frac{\partial\xi}{\partial\tilde{z}}\right] + \tilde{\nabla}^2\left[\left(\frac{\partial\xi}{\partial\tilde{z}}\right)^2\right] + \tilde{\nabla}^2\left[\frac{\partial^2\xi}{\partial\tilde{z}^2}\right]\right) \tag{5.2.22}$$

is comprised of several terms. These terms will be discussed in the following sections.

Note that the transformed unperturbed equation

$$\left[\widetilde{\nabla}^2_{\mathrm{red}} + \omega^2\mu\tilde{\epsilon}_0(\tilde{x},\tilde{y})\right] E_m(\tilde{x},\tilde{y})e^{i(\omega t-\beta_m\tilde{z})} = 0 \tag{5.2.23}$$

is solved by the same Eigenfunctions as Eq. (4.0.14) derived in Sec. 4, only that $x \to \tilde{x}$, i.e., $E_m(\tilde{x},\tilde{y})e^{i(\omega t-\beta_m\tilde{z})}$.

### 5.2.1. Stratified disorder approximation

As discussed above, all previous approaches have only considered the first term on the right side of Eq. (5.2.22) which is independent of the derivative of $\xi$. In this case the dielectric perturbation simplifies as follows:

$$\Delta\tilde{\epsilon} = \frac{1}{\omega^2\mu}\left(\frac{d^2}{w^2} - 1\right)\frac{\partial^2}{\partial\tilde{x}^2} \tag{5.2.24}$$

The coupling coefficient from Eq. (5.1.7) becomes

$$C_{kl} = \frac{\omega}{p}\int\int d\tilde{x}d\tilde{y}\left|\frac{w}{d}\right|\tilde{E}_k\Delta\tilde{\epsilon}\tilde{E}_l i \tag{5.2.25}$$

where the prefactor is the Jacobian $dxdy = d\tilde{x}d\tilde{y}\left|\frac{w}{d}\right|$. Note that the $\tilde{E}_k$, are the undisturbed modes of the transformed system, with $\Delta\tilde{\epsilon} = 0$ in Eq. (5.2.23). Undisturbed means that $w(\tilde{z}) = d = \text{const}$. Therefore the undisturbed and the disturbed equation are equivalent up to a substitution $x \to \tilde{x}$. Therefore, the $\tilde{E}_k$'s as solutions of the transformed equation can be generated from the $E_k$'s (derived in Sec. 4) by substitution $x \to \tilde{x}$.

The function $\left(\frac{d^2}{w^2} - 1\right)$ is periodic in $\tilde{z}$, due to $w(\tilde{z})$, and has the same periodicity as $\xi$. The same holds for the function when multiplied with the Jacobian $\left(\frac{d}{w} - \frac{w}{d}\right)$. It can thus be expanded into a Fourier series (Eq. (5.1.8)). Note, that the expansion is done *after* neglecting (for the time being) all other terms in $\Delta\tilde{\epsilon}$, especially those with a with derivatives of $\xi$. Previous approaches obscured this simplification, by performing the expansion without mentioning the implicit neglect of these terms [Kog75; Ebe92].

Now the coupling coefficient in this *stratified approximation* can be calculated as

$$C_{kl} = \frac{1}{u\omega\mu} \int\int \left|\frac{w}{d}\right| d\tilde{x}d\tilde{y}\tilde{E}_k \left(\frac{d^2}{w^2} - 1\right) \frac{\partial^2}{\partial\tilde{x}^2}\tilde{E}_l \tag{5.2.26}$$

$$= \left(\frac{d}{w} - \frac{w}{d}\right) \underbrace{\frac{1}{u\omega\mu} \int\int d\tilde{x}d\tilde{y}\tilde{E}_k \frac{\partial^2}{\partial\tilde{x}^2}\tilde{E}_l}_{=I_{kl}^{(b)}} \tag{5.2.27}$$

Here, the integral named $I_{kl}^{(b)}$ is independent of the boundary and thus of little interest in the following. The prefactor, that will be called $p(z)$, can be further simplified, by approximating $\left(\frac{d}{w} - \frac{w}{d}\right) = -4\frac{\sigma}{d}\xi\frac{d+\sigma\xi}{d+2\sigma\xi} \approx -4\frac{\sigma}{d}\xi$. With this:

$$C_{kl} \approx \underbrace{-4\frac{\sigma}{d}\xi}_{=p(z)} I_{kl}^{(b)} \tag{5.2.28}$$

$$= p(z)\, I_{kl}^{(b)} \tag{5.2.29}$$

$$= \sum_m p_m^{(b)}\, I_{kl}^{(b)} e^{-im\frac{2\pi}{\Lambda}\tilde{z}} \tag{5.2.30}$$

$$= \sum_m \hat{C}_{kl} e^{-im\frac{2\pi}{\Lambda}\tilde{z}} \tag{5.2.31}$$

where $\hat{C}_{kl} = p_m^{(b)} I_{kl}^{(b)}$. The coupling coefficient without hat, denotes the coupling coefficient after expanding the prefactor $p$, i.e., $C_{kl} = p(z) I_{kl}^{(b)}$. To show that Bragg scattering can be derived from this expression, the derivation of Yariv and Yeh [YY03] is used. To analyze small changes in the amplitude $A(z)$ in Eq. (5.1.4), $dA$ is integrated over a length $s$, which is long compared to the periodicity of the disorder $\Lambda$ (which was introduced in Eq. (5.1.8)):

$$dA_k \sim \sum_l \sum_m \int_s dz C_{kl} A_l e^{i(\beta_k - \beta_l - m\frac{2\pi}{\Lambda})z} \tag{5.2.32}$$

As long as the Bragg condition

$$\beta_k - \beta_l = m\frac{2\pi}{\Lambda} \tag{5.2.33}$$

is not satisfied, the integral in Eq. (5.2.32) will vanish, due to the oscillations of the exponential function. A vanishing coupling coefficient obliviously means that there is no coupling between the modes. It can be seen that the Bragg scattering follows directly from the periodicity of $\Delta\tilde{\epsilon}$. Consequently, the Bragg scattering is a direct

result of the stratified approximation. This approximation in the transformed system is in perfect agreement with the previous text book approaches [YY03].

Note, that the index $m$ does not enumerate the different orders of Bragg reflection known from simple periodic lattices. The index relates to the expansion of the perturbation. For example, a simple sinusoidal boundary will sum over $m = \pm 1$ only. In both cases the Bragg condition is fulfilled for the same frequency, only the direction of both, incoming and reflected mode is reversed. Consequently there is only a single Bragg condition.

### 5.2.2. Solutions to the coupled mode equations

In the last sections general properties of the coupling equation (5.1.6) were investigated. Now a solution for the Bragg scattering situation is discussed [YY03]. To facilitate reading, Eq. (5.1.6) is repeated:

$$\frac{d}{dz}A_k = -i\frac{\beta_k}{|\beta_k|}\sum_l C_{kl}A_l e^{i(\beta_k-\beta_l)z} \tag{5.2.34}$$

Let's assume only two modes, i.e. $k = 1, l = 2$. For backscattering both modes have opposite direction, thus $\beta_1 > 0 > \beta_2$. The prefactor $\frac{\beta_{1,2}}{|\beta_{1,2}|}$ becomes 1 and -1, respectively. After writing $C_{kl}$ as a Fourier transformation $\hat{C}_{kl}$, it can be noted that there is only a single coupling coefficient $\hat{C} = \hat{C}_{12}$, since $\hat{C}_{12} = \left(\hat{C}_{21}\right)^*$, where the asterisk denotes complex conjugation. Thus, the two coupled differential equation read

$$\frac{d}{dz}A_1 = -i\hat{C}e^{i\Delta\beta z}A_2 \tag{5.2.35}$$

$$\frac{d}{dz}A_2 = i\hat{C}^* e^{-i\Delta\beta z}A_1 \tag{5.2.36}$$

where $\Delta\beta = \beta_k - \beta_l - m\frac{2\pi}{\Lambda}$. To solve the equations, boundary conditions have to be imposed. The interaction of the modes is restricted to the disordered section of the waveguide, which is defined to range from $z = 0$ to $z = L$. The incident wave (propagating in positive $z$-direction) will be at its maximum, before the interaction, i.e., $A_1(0) = 1$. Reflection occurs only within the disordered section. Therefore, the reflected wave (propagating in negative $z$-direction) is zero at the end of the disordered

section, i.e., $A_2(L) = 0$. With these boundary conditions, the equations are solved by

$$A_1 = \exp\left(\frac{i\Delta\beta z}{2}\right) \frac{\left(s\cosh(s(L-z)) + \frac{1}{2}i\Delta\beta\sinh(s(L-z))\right)}{s\cosh(Ls) + \frac{1}{2}i\Delta\beta\sinh(Ls)} \tag{5.2.37}$$

$$A_2 = \frac{\exp\left(\frac{1}{2}(-i)\Delta\beta z\right)\left(-i\hat{C}^*\sinh(s(L-z))\right)}{s\cosh(Ls) + \frac{1}{2}i\Delta\beta\sinh(Ls)} \tag{5.2.38}$$

with $s^2 = \hat{C}^*\hat{C} - \frac{\Delta\beta}{2}$.

To investigate Bragg scattering, one is interested in the reflection. The reflection is given by

$$R = \left|\frac{A_2(0)}{A_1(0)}\right|^2 \tag{5.2.39}$$

$$= \left|\frac{\hat{C}\sinh(sL)}{s\cosh(sL) + \frac{1}{2}i\Delta\beta\sinh(sL)}\right|^2 \tag{5.2.40}$$

A typical example of a Bragg reflection is depicted in Fig. 5.1, for a value of $\hat{C} = 5$ [YY03]. The calculated reflectivity is high for values of $\Delta\beta$ around zero, i.e., when the Bragg condition is fulfilled. The width of the this Bragg reflection resonance is given by the strength of the coupling, the coupling coefficient $\hat{C}$. The coupling coefficient depends on the overlap of the two modes. Hence, Bragg scattering occurs when the Bragg condition is fulfilled *and* the two modes overlap.

In the Appendix (Sec. 8.1) it is shown that this approach, including coordinate transformation and stratified approximation, developed in this sections is in good agreement with previous experiments [FKS+74]. Thus, the next step is to investigate the terms that have so far being neglected in coupled mode theory.

### 5.2.3. Square Gradient (SG) Bragg approximation

In the last section it was shown that a dielectric perturbation with simple periodicity of $\Lambda$ will yield Bragg scattering. This is a well known result. However, in contrast to text book approaches it was shown that this simple approach covers only stratified disorder. What happens when going beyond this class of systems? Analyzing the periodicity of the perturbation was a good starting point, therefore a detailed analysis of the periodicity is the next step.

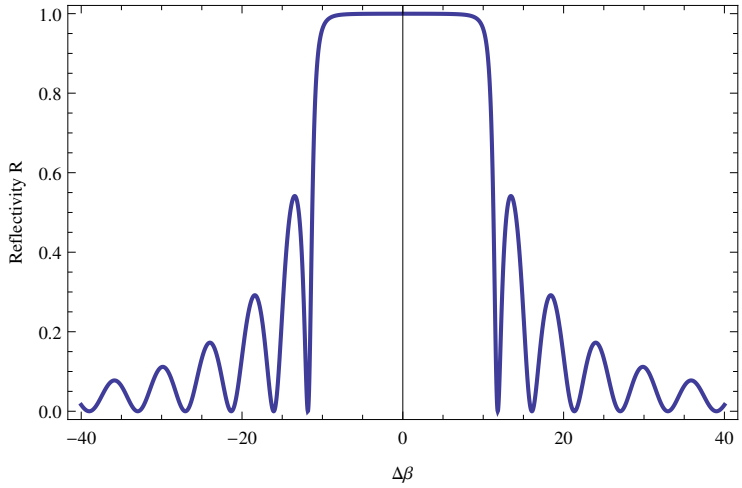


Figure 5.1.: Reflectivity calculated from the solution of the coupled mode equations for a single scattering mechanism Eq. (5.2.40) ($\hat{C} = 5, L = 1$).

When taking the derivative of the expansion in Eq. (5.1.8), it yields

$$\frac{\partial \Delta\epsilon}{\partial z} = \sum_{m\neq 0} \epsilon_m(x,y)(-im\frac{2\pi}{\Lambda})e^{-im\frac{2\pi}{\Lambda}z} \tag{5.2.41}$$

which shows that a periodic function and its derivative share the same periodicity. This is because the differential operator is linear. Therefore this is true for the second derivative as well. In contrast, the (obvious non-linear) square of a function can have a different periodicity. For example the square of sine has half the wavelength. This holds for every function which satisfies $f(x + \Lambda/2) = -f(x)$.

Using this fact, the terms of $\tilde{\nabla}^2$ in Eq. (5.2.22) can be rearranged according to their periodicity. The periodicity of all terms involving no square of the derivative of $\xi$ will have at most periodicity $\Lambda$, while the terms with square of the derivative of $\xi$ can have a different periodicity $\Lambda^{(sg)}$ than $\Lambda$. Formally, one can write:

$$\Delta\tilde{\epsilon} = \Delta\tilde{\epsilon}_{\Lambda} + \Delta\tilde{\epsilon}_{\Lambda^{(sg)}} \tag{5.2.42}$$

In this section the focus is on the terms with higher periodicity. These are given by

$$\Delta\tilde{\epsilon}_{\Lambda^{(sg)}} = \frac{1}{\omega^2\mu}\frac{\sigma^2}{w^2}\left(\frac{\partial\xi}{\partial\tilde{z}}\right)^2\left(3\tilde{x}\frac{\partial}{\partial\tilde{x}} + \tilde{x}^2\frac{\partial^2}{\partial\tilde{x}^2}\right) \tag{5.2.43}$$

and thus

$$C_{kl}^{(sg)} = \frac{\sigma^2}{wd}\left(\frac{\partial\xi}{\partial\tilde{z}}\right)^2 \underbrace{\frac{1}{u\omega\mu}\int d\tilde{x}d\tilde{y}\tilde{E}_k\left(3\tilde{x}\frac{\partial}{\partial\tilde{x}} + \tilde{x}^2\frac{\partial^2}{\partial\tilde{x}^2}\right)\tilde{E}_l}_{I_{kl}^{(sg)}} \tag{5.2.44}$$

As before, the part that does not depend on $\tilde{z}$ is summarized as $I_{kl}^{(sg)}$. The prefactor is governed by $\left(\frac{\partial\xi}{\partial\tilde{z}}\right)^2$, and thus $w$ can be approximated as $w = d$, yielding

$$\begin{aligned} C_{kl}^{(sg)} &\approx \underbrace{\frac{\sigma^2}{d^2}\left(\frac{\partial\xi}{\partial\tilde{z}}\right)^2}_{=p^{(sg)}(z)} I_{kl}^{(sg)} && (5.2.45)\\ &= p^{(sg)}(z)\, I_{kl}^{(b)} && (5.2.46)\\ &= \sum_m p_m^{(sg)}\, I_{kl}^{(b)} e^{-im\frac{2\pi}{\Lambda}\tilde{z}} && (5.2.47)\\ &= \hat{C}_{kl}^{(sg)}\Big|_{m=0} + \sum_{m\neq 0}\hat{C}_{kl}^{(sg)} e^{-im\frac{2\pi}{\Lambda^{(sg)}}\tilde{z}} && (5.2.48) \end{aligned}$$

The integral $I_{kl}^{(sg)}$ can be calculated when the particular shape of $\tilde{E}$'s is known, for example for TE and TM Modes. As before, the coupling coefficient is expanded according to its periodicity in $z$-direction. However, this time the periodicity is the periodicity of the square of the derivative of $\xi$. This is denoted with $\Lambda^{(sg)}$. Secondly, the expansion now features a constant term $C_{kl}^{(sg)}\Big|_{m=0}$. This term is not present in the expansion of $\xi$, since, following the definition, $\xi$ is mean free. However, a real valued function squared will be strictly positive, and thus have some finite mean.

The analysis of non vanishing contributions as in Eq. (5.2.32) will yield a new coupling condition, similar to the well known Bragg condition. The only difference is that the underlying periodicity is given by the derivative of the boundary, and not the boundary itself. This is the central result of this chapter.

### 5.2.4. Solutions to the coupled mode equations for two scattering mechanisms

Deriving the solutions for the coupled mode equations is simple, as long as there is only a Bragg scattering involved. This is the case in the stratified disorder approximation (Sec. 5.2.1).

In the Square Gradient approximation (Sec. 5.2.3) scattering contributions from

Bragg and Square Gradient scattering have to be taken into account. Consequently the coupled mode equations become more complicated.

Consider Eq. (5.1.6). For the single Bragg scattering mechanism, $C_{kl}$ is given by Eq. (5.2.26). In this section $C_{kl}$ is taken to be the sum of the two scattering mechanisms, discussed beforehand, namely Eq. (5.2.31) and Eq. (5.2.48). Again, it is assumed that there are only two mode $k = 1$ and $l = 2$. Then, the full coupled mode equation reads

$$\frac{d}{dz}A_1 = -i\left(\hat{C}e^{i\Delta\beta z} + \hat{C}^{(0)}e^{i\Delta\beta^{(0)}z} + \hat{C}^{(2)}e^{i\Delta\beta^{(2)}z}\right)A_2 \tag{5.2.49}$$

$$\frac{d}{dz}A_2 = i\left(\hat{C}^{*}e^{-i\Delta\beta z} + \hat{C}^{(0)^{*}}e^{-i\Delta\beta^{(0)}z} + \hat{C}^{(2)^{*}}e^{-i\Delta\beta^{(2)}z}\right)A_1 \tag{5.2.50}$$

with

$$\Delta\beta = \beta_k - \beta_l - m\frac{2\pi}{\Lambda} \tag{5.2.51}$$

$$\Delta\beta^{(2)} = \beta_k - \beta_l - m\frac{4\pi}{\Lambda} \tag{5.2.52}$$

$$\Delta\beta^{(0)} = \beta_k - \beta_l \tag{5.2.53}$$

Instead of solving the complete equation, things can be simplified. It was discussed along Eq. (5.1.6) that the amplitudes $A_k$ only vary close to the wavelength, where the Bragg condition is fulfilled. That is, Bragg scattering takes place only for $\Delta\beta \to 0$, while square gradient scattering can occur for $\Delta\beta^{(0)} \to 0$ and $\Delta\beta^{(2)} \to 0$.

Therefore, for each of the three conditions Eq. (5.2.51), Eq. (5.2.52), Eq. (5.2.53) one can separately construct a solution for the coupled mode equation. This means one solves the Eq. (5.2.50) for each of the 3 terms, while ignoring the two others. This yields three pairs of different solutions

$$A_1(\Delta\beta), A_2(\Delta\beta) \tag{5.2.54}$$

$$A_1(\Delta\beta^{(2)}), A_2(\Delta\beta^{(2)}) \tag{5.2.55}$$

$$A_1(\Delta\beta^{(0)}), A_2(\Delta\beta^{(0)}) \tag{5.2.56}$$

The reflectivity for the separate scattering mechanisms can then be approximated by

$$R^{tot} = \left|\frac{A_2(\Delta\beta)}{A_1(\Delta\beta)}\right|^2 + \left|\frac{A_2(\Delta\beta^{(0)})}{A_1(\Delta\beta^{(0)})}\right|^2 + \left|\frac{A_2(\Delta\beta^{(2)})}{A_1(\Delta\beta^{(2)})}\right|^2 \tag{5.2.57}$$

If the above assumptions are correct, it is should be possible to calculate the different

scattering mechanisms separately and afterwards combine them to yield a single expression for the reflectivity $R^{tot}$. Later in this thesis, a comparison to numerical data will show that this approach makes valid predictions.

## 5.3. Generalized coupled mode equations for arbitrary boundary profiles

The results derived in the coupled mode approach are already in good agreement with previous results. However, they are still restricted to periodic boundaries. In this sections it is shown how the results for arbitrary boundary profiles are obtained. Instead of expanding the dielectric perturbation in a Fourier series, it will now be represented as its Fourier transformation. This means the function $p^{(b)}(z)$ (see Eq. (5.2.30)) is no longer treated as a periodic function:

$$p^{(b)}(\tilde{z}) = \sum_m p_m^{(b)} e^{-im\frac{2\pi}{\Lambda}z} \rightarrow \int dg \hat{p}^{(b)}(g) e^{-igz} \tag{5.3.1}$$

To obtain the Bragg condition in the continuous case, the $dA_k$ is, as in Eq. (5.2.32), integrated over a small domain $s$ $C_{kl}$

$$dA_k = -i\frac{\beta_k}{|\beta_k|} \sum_l \int dg \hat{p}^{(b)}(g) \underbrace{\int_s dz\, I_{kl}^{(b)} A_l e^{i(\beta_k - \beta_l - g)z}}_{=0,\, \forall\, \beta_k - \beta_l \neq g} \tag{5.3.2}$$

The exponential function in the second integral oscillates and will thus be zero, as long as $\beta_k - \beta_l \neq g$. Therefore, the result can be approximated by

$$dA_k \approx -i\frac{\beta_k}{|\beta_k|} \sum_l \int dg \hat{p}^{(b)}(g) N\delta(\beta_k - \beta_l - g) \int_s dz\, I_{kl}^{(b)} A_l \tag{5.3.3}$$

$$= -i\frac{\beta_k}{|\beta_k|} \sum_l N\hat{p}^{(b)}(\beta_k - \beta_l) \int_s dz\, I_{kl}^{(b)} A_l \tag{5.3.4}$$

The normalization $N$ will be discussed below. This line of reasoning holds for both $p^{(b)}(g)$ for Bragg scattering and $p^{(sg)}(g)$ for SG-Bragg scattering. The coupling is proportional to $\hat{p}^{(b)}(\beta_k - \beta_l)$, or $\hat{p}^{(b)}(2\beta_k)$, in case of Bragg (back)scattering, where $\beta_k = -\beta_l$. Taking the derivative of Eq. (5.3.4) yields the generalized coupled mode equation

$$\frac{dA_k}{dz} = -i\frac{\beta_k}{|\beta_k|} \sum_l N\hat{p}^{(b)}(\beta_k - \beta_l) I_{kl}^{(b)} A_l \tag{5.3.5}$$

As before, solving this equation for two modes ($k = 1, l = 2$) and assuming contra-directional coupling, yields two solutions. These solutions yield the reflectivity

$$R = \left|\frac{A_2(0)}{A_1(0)}\right|^2 = \left|\tanh\left(N\hat{p}(\beta_1 - \beta_2)I_{kl}^{(b)}L\right)\right|^2 \tag{5.3.6}$$

To fix the normalization $N$, it is assumed that the generalized as well as the standard (infinite) coupled mode equation (5.2.36) yield the same result over a finite range L, when evaluating periodic boundaries. The maximum reflectivity for standard coupled mode theory is given by $R_{max} = \tanh(p_m I_{kl}^{(b)}L)^2$ [FKS+74]. Therefore, at the point of maximum reflectivity the normalization is fixed with $N\hat{p}^{(b)}(\beta_b) = p_1$, which yields $N = \frac{2\pi}{L}$.

### 5.3.1. Previous theory: Boundary roughness in PEC waveguides

In PEC waveguides the integrals $I_{kl}^{(b)/(sg)}$ (Eq. (5.2.44) and (5.2.26)) take a much simpler form, since the mode is confined inside the waveguide ($E_s = 0$). Furthermore $\kappa_f = \frac{\pi m}{d}$ and thus $\sin(d\kappa_f) = 0$ and $\cos(d\kappa_d) = 1$. The resulting integrals are solved in Appendix Sec. 8.1. The normalization in the PEC case yields $E_f^2 = \frac{u\omega\mu}{d\beta}$ as calculated in Eq. (4.2.24) . Hence, the analytic form of the coupling coefficients follows as

$$I_{kl}^{(b)} = -\frac{1}{2}\frac{\pi^2 n^2}{\beta d^2} \tag{5.3.7}$$

$$I_{kl}^{(sg)} = \frac{1}{6\beta}\left(3 + \pi^2 n^2\right) \qquad \text{for odd modes } m \tag{5.3.8}$$

$$I_{kl}^{(sg)} = -\frac{1}{6\beta}\left(3 - \frac{\pi^2 n^2}{4}\right) \qquad \text{for even modes } m \tag{5.3.9}$$

Now the above integrals are compared with the results derived within the previous theoretical approach [IMR06] (see [DSK+12] for a summary). In the previous approach, the author derived expression for the backscattering length $L_n^{(b),(AS)/(SGS)}$, for Amplitude (AS) and Square Gradient scattering (SGS). The amplitude scattering was coined due to its dependency on the amplitude of $\xi$. However, it is nothing but Bragg scattering. The backscattering length is connected to the transmittance of a sample of length L via $T \sim exp\left(\frac{L}{4L_n^{(b)}}\right)$. These expression have been introduced in Ch. 3. Here, the analytical expression for the backscattering length are repeated for

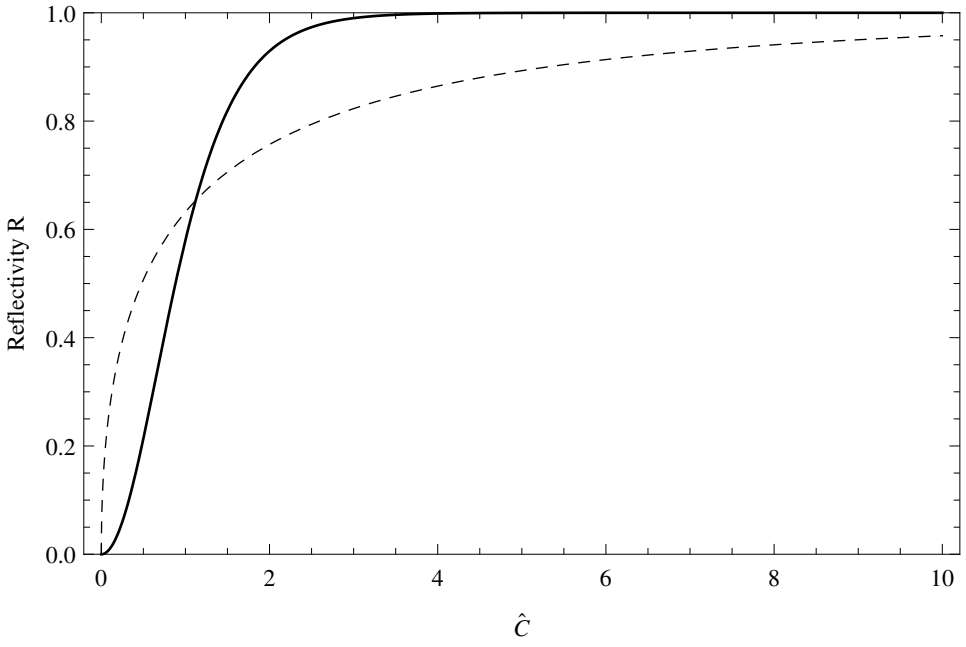


Figure 5.2.: Comparison of the functional behavior predicted in this this work ($\tanh(\hat{C})^2$, black, ——) and the predictions made in the surface scattering theory [DSK+12] ($1 - \exp(-\sqrt{\hat{C}})$, dashed black, - - -). .

convenience

$$\frac{1}{L_n^{(b),(AS)}} = \frac{\sigma^2}{d^6}\frac{4\pi^4 n^4}{\beta^2} W(2\beta)\,, \tag{5.3.10}$$

$$\frac{1}{L_n^{(b),(SG)}} = \frac{\sigma^4}{d^4}\frac{(3+\pi^2 n^2)^2}{18\beta^2} S(2\beta)\,. \tag{5.3.11}$$

From the definition of $p^{(b)/(sg)}$ in Eq. (5.2.30) and Eq. (5.2.47) it follows that

$$\left|\hat{p}^{(b)}(2\beta)\left(-\frac{d}{4\sigma}\right)\right|^2 = W(2\beta) \tag{5.3.12}$$

$$\left|\hat{p}^{(sg)}(2\beta)\left(\frac{d^2}{\sigma^2}\right)\right|^2 = S(2\beta) \tag{5.3.13}$$

It thus turns out that the coupling coefficients $\hat{C}^{(b)/(sg)} = \hat{p}^{(b)/(sg)} I_{kl}^{(b)/(sg)}$ can be written as

$$\frac{1}{L_n^{(b),(AS)}} = \left(\hat{C}^{(b)}\right)^2 \tag{5.3.14}$$

$$\frac{1}{L_n^{(b),(SGS)}} = \left(\hat{C}^{(sg)}\right)^2 \qquad \text{for odd modes } n \tag{5.3.15}$$

$$\tag{5.3.16}$$

Surprisingly, the square of the coupling coefficients $\hat{C}_{kl}^{(b)/(sg)}$ derived within the coupled mode approach are *identical* to the localization lengths derived within the statistical approach. This means that the approach presented in this work includes the previous results. However, since it was derived without any statistical assumptions about the disorder, it is the more general theory, which can be applied to many more systems that are not covered by the statistical approach.

The equality of the two quantities (the localization length and the coupling coefficient) should be investigated more closely, because there might be intimate connections between the coupled mode and the localization length framework. This is beyond the scope of this thesis.

Comparing the maximum reflectivity that can be calculated from Eq. (5.2.40) as $R = \tanh^2(\hat{C}L)$ with the transmission in the statistical (localization length) approach [DSK+12] $T = 1 - R = \exp(L/L_n^{(b)})$, one finds that the functional behavior of $\tanh^2(\hat{C})$ and $1 - \exp(\sqrt{\hat{C}})$ is qualitatively similar, as shown in Fig. 5.2. Comparing both

quantities for unit length $L = 1$ and small $\hat{C}$, $\frac{1}{L}$, one finds that

$$R = \tanh(\hat{C})^2 \approx \hat{C}^2 \tag{5.3.17}$$

$$R = 1 - \exp(-\frac{1}{L_n^{(b)}}) \approx \frac{1}{L_n^{(b)}} \tag{5.3.18}$$

and thus

$$\hat{C}^2 = \frac{1}{L_n^{(b)}} \tag{5.3.19}$$

There is evidence both quantities are different representations of the very same effect, namely coherent backscattering. That coherent backscattering is the origin of both effect is known [Joh87], but a strict relationship as presented here is unknown.

### 5.3.2. Impact of SG-Bragg scattering in sinusoidal boundary

In the previous sections the coupling integrals $I_{kl}^{(b)/(sg)}$ (Eq. (5.2.44) and (5.2.26)) were derived for a special case, the PEC waveguide, for comparison with previous theories. These integrals can can be calculated for dielectric waveguides as well, which is shown in the Appendix Sec. 8.1.

The results in the previous section were independent of the boundary profile. The boundary profile influences the prefactor $p^{(b)/(sg)}$ (Eq. (5.2.30) and (5.2.47)). In this section the prefactor is calculated for a special case of boundary profile, the sinusoidal boundary. This is done to better understand the influence of the Square Gradient Bragg scattering. Calculating the prefactor $p^{(b)/(sg)}$ for a given boundary is the last prerequisite for calculate the reflectivity in a dielectric waveguide.

Let the boundary of such a system be of the simplest possible form:

$$\xi(z) = \sin(k_b z)\mathrm{box}_0^L(x) \tag{5.3.20}$$

where $\mathrm{box}_0^L(x)$ is a box, or rectangular, function of length $L$ constructed via the Heaviside function $\Theta$, as $\mathrm{box}_0^L(x) = \Theta(x)\,(1 - \Theta(x - L))$. The wave vector of the boundary roughness $k_b$ should be chosen in such a way that $k_b L$ are multiples of $2\pi$ to ensure a continuous function.

To calculate $p^{(b)}$ (see Eq. (5.2.30)) and $p^{(sg)}$ (see Eq. (5.2.47)) the following ex-

pressions have to be calculated

$$\xi' = \sqrt{2}k_b \cos(k_b x)\mathrm{box}_0^L(x) + \sqrt{2}\sin(k_b x)\left(\delta(x) - \delta(x-L)\right) \tag{5.3.21}$$

$$\xi'^2 = 2k_b^2 \cos(k_b x)^2 \mathrm{box}_0^L(x)^2 \tag{5.3.22}$$

$$+ 2\sin(k_b x)^2 \left(\delta(x) - \delta(x-L)\right)^2 \tag{5.3.23}$$

$$+ 4k_b \cos(k_b x)\mathrm{box}_0^L(x)\sin(k_b x)\left(\delta(x) - \delta(x-L)\right) \tag{5.3.24}$$

Now the Fourier transformation of $\xi'^2$ has to be calculated. However for the chosen $k_b$ the second and the third term vanishes since

$$\int \sin(k_b x)\left(\delta(x) - \delta\left(x-L\right)\right)\exp(-ikx) = \sin(0)\exp(0) - \sin(k_b L)\exp(ikL) = 0 \tag{5.3.25}$$

Now using $\mathrm{box}_0^L(x)^2 = \mathrm{box}_0^L(x)$, the square of the cosine can be rewritten as a sum of two cosines

$$\mathcal{FT}\left(\xi'^2\right) = 2k_b^2 \mathcal{FT}\left(\cos(k_b x)^2 \mathrm{box}_0^L(x)^2\right) \tag{5.3.26}$$

$$= 2k_b^2 \mathcal{FT}\left(\left(\cos(0) + \cos(2k_b x)\right)\mathrm{box}_0^L(x)\right) \tag{5.3.27}$$

$$= 2k_b^2 \mathcal{FT}\left(\mathrm{box}_0^L(x)\right) + k_b^2 \mathcal{FT}\left(\cos(2k_b x)\mathrm{box}_0^L(x)\right) \tag{5.3.28}$$

The intermediate result in Fourier representation is

$$\mathcal{FT}\left(\xi\right) = \sqrt{2}\left|\mathcal{FT}\left(\sin(k_b x)\mathrm{box}_0^L(x)\right)\right|^2 \tag{5.3.29}$$

$$\mathcal{FT}\left(\xi'^2\right) = 2k_b^2\left|\mathcal{FT}\left(\mathrm{box}_0^L(x)\right) + \mathcal{FT}\left(\cos(2k_b x)\mathrm{box}_0^L(x)\right)\right|^2. \tag{5.3.30}$$

Using the convolution theorem

$$\mathcal{FT}\left(fg\right) = \mathcal{FT}\left(f\right) * \mathcal{FT}\left(g\right) \tag{5.3.31}$$

the result can be further simplified. The $(*)$ operator denotes a convolution. Particularly interesting for the present case is the convolution with a $\delta$-function, which evaluates to

$$f(x) * \delta(x-b) = f(x-b) \tag{5.3.32}$$

Shifting a function will add an additional phase factor to its Fourier transformation. Therefore, instead of evaluating the functions in Eq. (5.3.30) directly, they will be shifted to be centered around $x = 0$. The Fourier transformation of a centered box

function is given by

$$\mathcal{FT}\left(\mathrm{box}_{-L/2}^{L/2}(x)\right) = \frac{L}{2\pi}\,\mathrm{sinc}\left(\frac{\beta L}{2}\right) \tag{5.3.33}$$

and the Fourier transformation of the Cosine and Sine is given by

$$\mathcal{FT}\left(\sin k_b x\right) = \frac{i}{2}\delta(\beta + kb) - \frac{i}{2}\pi\delta(\beta - k_b) \tag{5.3.34}$$

$$\mathcal{FT}\left(\cos 2k_b x\right) = \frac{i}{2}\delta(\beta + 2k_b) + \frac{i}{2}\pi\delta(\beta - 2k_b) \tag{5.3.35}$$

Applying the convolution theorem and evaluating the $\delta$-functions the resulting expression reads

$$\mathcal{FT}\left(q\right) = \frac{L}{2\pi}\frac{i}{\sqrt{2}}\left(\mathrm{sinc}\left(\frac{1}{2}(\beta - k_b)L\right)\right. \tag{5.3.36}$$

$$\left. -\mathrm{sinc}\left(\frac{1}{2}(\beta + k_b)L\right)\right) \tag{5.3.37}$$

$$\mathcal{FT}\left(q'^2\right) = \frac{L}{\pi}k_b^2\left(\mathrm{sinc}\left(\frac{\beta L}{2}\right) + \frac{1}{2}\mathrm{sinc}\left(\frac{1}{2}(\beta - 2k_b)L\right)\right) \tag{5.3.38}$$

$$+ \frac{L}{\pi}k_b^2\left(\frac{1}{2}\mathrm{sinc}\left(\frac{1}{2}(\beta + 2k_b)L\right)\right) \tag{5.3.39}$$

Now one can neglect the last terms in both equations, because they contribute for negative $\beta$ only. An inversion of the sign of $\beta$ is an inversion of the direction of the wave vector. Therefore these terms come into play only when both, incident and reflected wave are reversed. When a scattering direction has been chosen, e.g. $\beta > 0$, scattering does not occur for $\beta < 0$.

With the definitions from Eq. (5.2.30)

$$\hat{p}^{(b)} = -4\frac{\sigma}{d}\mathcal{FT}\left(\xi\right) \tag{5.3.40}$$

$$= \frac{i}{\sqrt{2}}\left(\mathrm{sinc}\left(\frac{1}{2}(\beta - k_b)L\right)\right) \tag{5.3.41}$$

and the definition from Eq. (5.2.47)

$$\hat{p}^{(sg)} = \frac{\sigma^2}{d^2}\mathcal{FT}\left(\xi'^2\right) \tag{5.3.42}$$

$$= \frac{\sigma^2}{d^2}\frac{L}{\pi}k_b^2\left(\mathrm{sinc}\left(\frac{\beta L}{2}\right) + \frac{1}{2}\mathrm{sinc}\left(\frac{1}{2}(\beta - 2k_b)L\right)\right) \tag{5.3.43}$$

one ends up at the desired expressions. The expression for $\hat{p}^{(sg)}$ consists of two

different terms. The first term, responsible for scattering at $\beta = 0$ is nothing but the Fourier transformation of the box-function, i.e., the length of the boundary. The individual shape of the boundary has no influence for small $\beta$. The second term is responsible for scattering a $\beta = 2\beta_b x$.

Hence, in contrast to Bragg scattering, Square Gradient Bragg scattering is expected to cause scattering at two different wavelength. The scattering at $\beta = 0$ has already been observed experimentally in a PEC waveguide [DSK+12], where it was believed that it is caused by a special random shape of the boundary. The scattering at $\beta = 2\beta_b x$ has so far only been numerically observed for ensembles of PEC waveguides [DMBF+14]. The analytical foundations laid out in the recent sections suggest that the scattering is a universal phenomenon, which is present in individual waveguides.

## 5.4. Comparison of analytical results and numerical simulation

In this section the impact of Square Gradient Bragg scattering for a dielectric waveguide is investigated. The waveguide (shown in Fig. 5.3) is designed in such a way that it can easily be realized in an experiment. The sinusoidal boundary is given by the normalized boundary function $\xi = \sqrt{2}\sin(\frac{2\pi}{\Lambda}$. The corresponding $\hat{p}^{(b)}$ and $\hat{p}^{(sg)}$ were calculated in the previous section (Eq. (5.2.30) and (5.2.47)). Plugging these, and the material parameters given in Fig. 5.3, into Eq. (5.3.6), yields the reflectivity. In the present case there are two odd modes $n = 1, 3$. For each mode, there is scattering expected for the Bragg scattering mechanism as well as for the Square Gradient Bragg scattering mechanism. Therefore Eq. (5.3.6) yields 4 different terms: $R_{11}^{(b)}$ and $R_{11}^{(sg)}$ for Bragg and SG-Bragg scattering into the same (first) mode and $R_{13}^{(b)}$ and $R_{13}^{(sg)}$ for Bragg and SG-Bragg scattering from the first into the third mode.

The numerical simulations in the following sections were performed by Günter Kewes in cooperation with Oliver Neitzke [DKN+15]. They used a commercial finite element equation-solver (JCMwave). The Maxwell's equations were solved on a non-uniform 2d mesh. Convergence was ensured by varying the finite element degree.

The intensities of the modes for a) Bragg and b) SG-Bragg reflection resonances are shown in Fig. 5.3. The most apparent fact when comparing the modes is that for Bragg scattering the transversal widths of the maxima are nearly constant along the waveguide. This is a visualization of the fact that Bragg scattering is connected to the stratified scattering in a waveguide. A stratified lattice in a waveguide with flat boundaries would in principle yield the same reflection resonance. In contrast, the

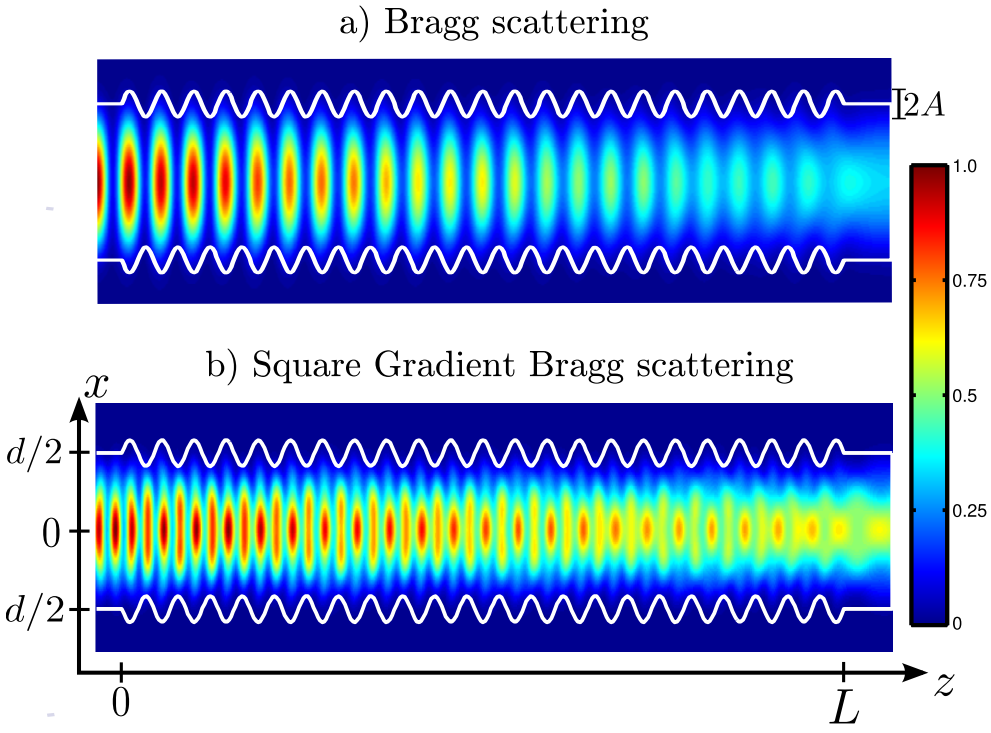


Figure 5.3.: Numerical simulation of the first mode. Modes (intensity $|E_y|^2$ in arbitrary units) at two different reflection resonances. a) Bragg scattering, corresponds to $R_{11}^{(b)}$ peak in Fig. 5.4 a). b) Square Gradient Bragg scattering, corresponds to $R_{11}^{(sg)}$ in Fig. 5.4 a). The (mean) width of the waveguide is $d = 450\,\text{nm}$, the length $L = 10d = 4.5\ \mu m$. The refractive index of the inner (outer) material is $n = 2$ ($n = 1$). The wavelength of the boundary oscillation is $\Lambda = 200$ nm, and its amplitude is $A = 37.5$ nm ($\sigma = 37.5\,\text{nm}/\sqrt{2}$).

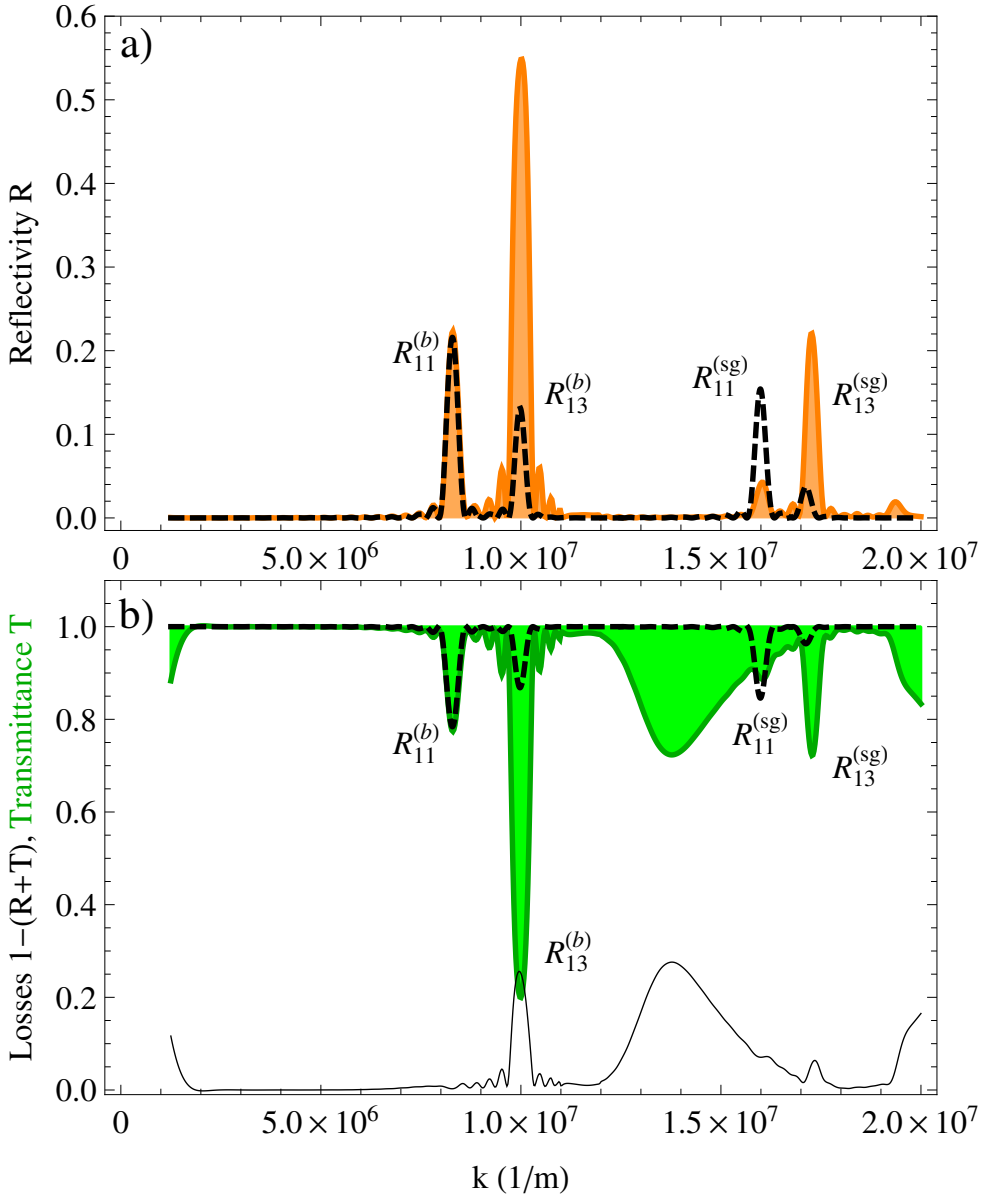


Figure 5.4.: a) Reflectivity of first mode through the dielectric waveguide shown in Fig. 5.3. Theoretical prediction (dashed black, - - -) calculate from Eq. (5.3.6) and (5.2.57) in comparison to numerical data (orange, ——). b) Analytically calculated transmission of the same mode (T=1-R, dashed black, - - -) compared to the numerically calculated transmission (green, ——). In addition the numerically calculated radiation loss is plotted as $1-(R+T)$ (black, ——).

intensity of the mode in Fig. 5.3 b) is modulated. That is, the widths of the maxima are alternating. The corrugated boundary imposes its deformation onto the mode.

### 5.4.1. Bragg scattering

The analytical predictions (orange, —) in comparison to the numerical simulation (dashed black, - - -) are shown in Fig. 5.4 a). For Bragg scattering into the same mode ($R_{11}^{(b)}$), there is a perfect agreement. Note, that this result was calculated with the coordinate transformation. This indicates that the coordinate transformation and the calculation are correct. For Bragg scattering into the third mode, the theory strongly *underestimates* the reflection resonance. This is surprising, because the strength of the reflection resonance depends on the overlap integral $I_{kl}^{(b)}$ (see Eq. (5.2.26)). The overlap integral has to be bigger for the *same* mode, compared to the overlap integral of two different modes.

These differences might be due to three mode coupling, which is discussed in Sec. 5.4.3. It is not very likely that these differences are caused by the two terms Eq. (5.2.15) and (5.2.17) that were neglected in derivation of this theory. These terms are active only at Bragg resonances. For SG-Bragg resonances $R_{13}^{(sg)}$ a comparable underestimation of the simulation is found. It is very likely that the same mechanism is responsible for both differences, at $R_{13}^{(b)}$ and $R_{13}^{(sg)}$. The neglect of the $\frac{\partial^2 A_k}{\partial z^2}$ might be a possible candidate, but a further investigation is outside the scope of this thesis. It is doubtful that the two-mode coupled mode approach is able to explain this derivation. Further effects like three-mode scattering and consecutive scattering chains involving different modes (as developed in [DMBF+14]) have to be taken into account to fully describe the scattering. For weaker perturbation the observed discrepancy may vanish, as shown in [DSK+12].

Note that the strength of the reflection resonance between the two modes ($R_{12}^{(c)}$) is twice as high as the reflection resonance in the same mode. This theoretically unexpected strength might have strong implications for applications. For example, Bragg mirrors, which are used in directional grating couplers (as in [KSM+15]) are always designed to reflect at the *same-mode* Bragg reflection resonance, i.e. $R_{11}^{(b)}$. It turns out that this is not the strongest reflection. In cases where the actual mode is not of interest, the efficiency of grating couplers can be enhanced by factor of two.

### 5.4.2. Square Gradient (SG) Bragg scattering

The situation for SG-Bragg scattering is similar. However, the reflection resonance $R_{11}^{(sg)}$ is *overestimated* by the theory. The actual simulated reflectivity for Bragg scattering is only around 25% of the predicted SG-Bragg scattering reflectivity. In the present system, SG-Bragg scattering seems to have little influence at first sight. But notice, that the reflectivity of the Bragg resonance is in total only around 20%. This system was not optimized for reflection resonances. In systems optimized for reflection, i.e., longer systems, the SG-Bragg reflection resonance is expected to increase accordingly.

As before, the reflection resonance from the first into the third mode is unexpectedly strong. In contrast to the unexpected strength of $R_{13}^{(b)}$, the neglected terms Eq. (5.2.15) and Eq. (5.2.17) of the Laplacian can be ruled out as possible reason in this case. Their periodicity, or, in other words, their independence of the square of $\xi$, inhibits their influence at the SG-Bragg frequencies. With the additional backscattering strength, the SG-Bragg scattering $R_{12}^{(sg)}$ becomes as strong as the $R_{11}^{(c)}$.

In all cases, the position of all four peaks is predicted with high accuracy. In conclusion, it can be stated that SG-Bragg reflection resonances are an important feature in corrugated dielectric waveguides. These new reflection resonances are comparable in size to the previously known Bragg resonances.

Note that this is the first direct observation of the new reflection resonances. Previous studies focused on the wavelength independent reflection resonance for small wavelength $\beta \to 0$ [DSK+12], and showed that there are additional reflection resonances when averaging over hundreds of very long systems [DMBF+14]. Both studies investigated PEC waveguides and were restricted by the statistical approach.

### 5.4.3. Reflection resonances in the transmission

The SG-Bragg scattering was investigated as reflection resonance. In order to investigate the influence of Bragg reflection resonances on transmission an independent numerical probe was inserted at the end of the waveguide to “measure” the transmission. For a lossless waveguide reflection and transmission are connected via

$$R + T = 1 \tag{5.4.1}$$

In the dielectric waveguide waves can scatter out of the waveguide, thus $R + T < 1$. In Fig. 5.4 b) the numerical transmission (green, —) is shown. To quantify the losses, i.e., scattering out of the waveguide, the quantity $R + T$ is plotted (black, —), which

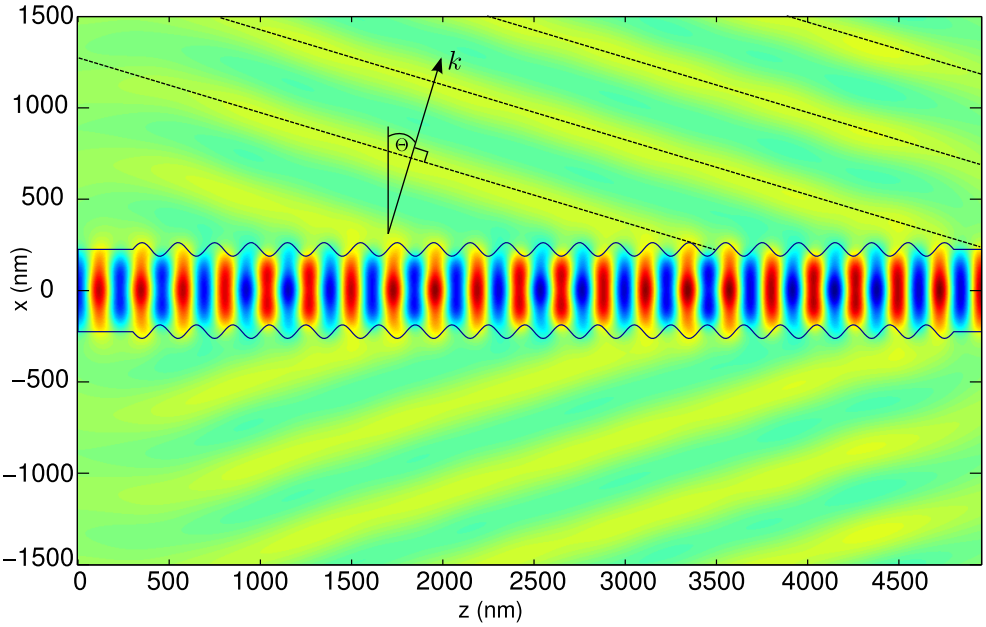


Figure 5.5.: E-Field (Re($E_y$)) at maximum of radiation losses at $k = 1.4 \cdot 10^7/m$ (compare dip in Fig. 5.4 b). Plane waves radiate out of the waveguide (dashed lines). The expected $k$-vector from Eq. (5.4.2) is indicated ($\Theta = 16.78°$).

is inversely proportional to the losses.

The most striking feature is that there is a broad gap at around $k = 1.4 \cdot 10^7/\mathrm{m}$. These are the wave vectors that are coupled out of the waveguide. The Bragg condition for coupling to the radiation modes is given by

$$kn \sin\Theta + \beta_{lat} = \beta_1 \tag{5.4.2}$$

where the radiation mode longitudinal wave vector is given by $\beta_{out} = nk \sin\Theta$ and $n$ is the refractive index of the outer material. From the maximum of the gap the coupling angle can be calculated as $\Theta = 16.78°$. In Fig. 5.5 the electric field at the minimum of the gap is shown. Strong scattering out of the waveguide can be observed. The calculated angle $\Theta$ is indicated. The plain waves radiating out of the waveguide are obviously perpendicular to the calculated $k$-vector. Thus, the gap is indeed due to scattering out of the waveguide.

Further examining the scattering losses, it turns out that there are strong losses at $R_{13}^{(b)}$ which increases the impact of that reflection resonance on the transmission. The damping in the transmission is close to 80%. Both SG-Bragg gaps show small losses as well. For the $R_{13}^{(sg)}$ the reduction is about 15%. These scattering losses at the exact same position as the reflection resonances show that the reflection resonances influence the transmission in a two fold way. At first, transmission is diminished due to the backscattering. Second, the transmission is further diminished due to scattering out of the waveguide. These *Bragg-assisted* losses are not covered by previous coupled mode approaches or the approach developed in this thesis. These effects are mentioned here, because they add to the importance of the SG-Bragg scattering mechanism. It is very likely that an investigation of all three involved modes sheds light on this issue. A three mode treatment in coupled mode theory means a total of 6 coupled equations, an – in principle – manageable task.

# 6. Summary of Part I

In this part, a new scattering mechanism in dielectric waveguides was derived. It is based on previous observations of scattering effects in perfectly electric conducting (PEC), hollow waveguides with corrugated boundaries with very peculiar statistical properties [IMR06]. Here, a general theory was brought forward, which is an extension of the coupled mode theory. The theory is in accordance with all previous experiments [FKS+74; DSK+12]. It predicts the Square Gradient (SG)-Bragg scattering mechanism for dielectric waveguides, as well as for PEC waveguides. It shows that the scattering mechanism is not an effect of certain statistical properties of the boundary, but can be calculated for arbitrary boundaries. The theoretical results were compared with numerical simulations. The simulations are in good agreement with the theory. They support the prediction that there exist previously unknown reflection resonances in dielectric waveguides. These findings can be directly applied to (waveguide) grating couplers and waveguides, for example as filters for integrated optics. As a result of this work, these findings have been reported in [DKN+15] (accepted for publication in Physical Review B).

# 7. Outlook and open questions of Part I

Several questions were raised in this part of the thesis, which are worth further investigation.

## Underestimation of inter-mode scattering

The coupled mode approach developed here and in previous approaches [Kog75] cannot explain an inter-mode scattering that is stronger than scattering into the same mode. Including more modes, e.g., incident, backscattered, and (lossy) out scattered modes, within coupled mode theory, might answer that question.

## Bragg-assisted scattering to substrate modes

The Bragg assisted losses mentioned in Sec. 5.4 are not covered by the two mode coupled mode approach. Here, further investigation into the three-mode coupled mode could shed some light on this issue.

## Additional neglected terms

The additional terms in Eq. (5.2.15), (5.2.17) that have been neglected in this thesis might have additional influence on the Bragg scattering. So far, the good agreement with previous experiments [FKS+74] seems to rule out this possibility.

## Overestimation of SG-Bragg scattering

The presented theory overestimates the influence of SG-Bragg scattering. It is normalized in such a way that the Fourier transformation and the Fourier series yield the same result. This is, in fact, choosing a proper normalization for the Fourier transformation. There might be a better way to normalize the SG-Bragg reflection peaks.

# 8. Appendix to Part I

## 8.1. Previous experiments: Sinusoidal boundary profile in dielectric waveguide

Here, the results of [FKS+74] are compared with derivation in this thesis. For a sinusoidal boundary the normalized boundary function takes the form

$$\xi = \sqrt{2}\sin\left(\frac{2\pi}{\Lambda}\tilde{z}\right)$$

The physical waveguide spans from $x = \sigma\xi$ to $x = d - \sigma\xi$. For a sine function the coefficients $p_m$ take especially simple forms, summarized in Tab. 8.1.

The integrals $I_{kl}^{(b)/(sg)}$ (Eq. (5.2.44) and (5.2.26)) are calculated in Tab. 8.2. In the case of a PEC waveguide the expression can be further simplified, since $E_s = 0$ and $\kappa_f = \frac{\pi m}{d}$. The expressions for the PEC waveguide are shown in Tab. 8.3. Note that the results are independent of $\xi$.

The coupling coefficients can then be calculated for given $d, L, E_f, n_s, n_f, N_{eff}$. For comparison with published experiments, the properties of Filter No. 1 in [FKS+74] are chosen. Bearing in mind that only the modulus of the coupling coefficient is

| Coefficient | | $p_0^{(sg)}$ | $p_1^{(b)}$ | $p_2^{(sg)}$ | numerical value |
|---|---|---|---|---|---|
| $p^{(b)}(z) =$ | $-4\frac{\sigma}{d}\xi$ | 0 | $-4\frac{\sigma}{d}\frac{1}{\sqrt{2}}i$ | 0 | $-0.054i$ |
| $p^{(sg)}(z) =$ | $\frac{\sigma^2}{d^2}\left(\frac{\partial\xi}{\partial\tilde{z}}\right)^2$ | $\frac{\sigma^2}{d^2}\left(\frac{\pi}{\Lambda}\right)^2$ | 0 | $\frac{\sigma^2}{d^2}\left(\frac{\pi}{\Lambda}\right)^2\frac{1}{2}$ | $\{2,1\}\cdot 5.27\cdot 10^{10}/m^2$ |

Table 8.1.: Coefficients $p_0^{(sg)}, p_1^{(b)}, p_2^{(sg)}$ calculated for $\xi = \sqrt{2}\sin\left(\frac{\pi}{\Lambda}\tilde{z}\right)$. Numerical values calculated with $\sigma, d, \Lambda$ for Filter No. 1 in [FKS+74]. Note that only the modulus of the value matters for the strength of the reflection.

| Integral | $\Delta\tilde{\epsilon}$ | Film | Substrate/Cover | Value |
|---|---|---|---|---|
| - | 1 | $+\frac{1}{2}E_f^2\left(d \pm \frac{\sin(d\kappa_f)}{\kappa_f}\right)$ | $+\frac{1}{2}E_{c,s}^2\frac{1}{\gamma_{c,s}}$ | $+2.95\cdot10^{-8}m$ |
| $I_{kl}^{(b)}$ | $\frac{\partial^2}{\partial\tilde{x}^2}$ | $-\frac{1}{2}E_f^2\kappa_f^2\left(d \pm \frac{\sin(d\kappa_f)}{\kappa_f}\right)$ | $+\frac{1}{2}E_{c,s}^2\gamma_{c,s}$ | $-10.7\cdot10^{4}/m$ |
| $I_{kl}^{(sg)}$ | $3x\frac{\partial}{\partial\tilde{x}}+x^2\frac{\partial^2}{\partial\tilde{x}^2}$ | … see below | … see below | $-3.98\cdot10^{-8}m$ |
| - | $x\frac{\partial}{\partial\tilde{x}}$ | $\pm\frac{1}{4}E_f^2\left(d\cos(d\kappa_f)-\frac{\sin(d\kappa_f)}{\kappa_f}\right)$ | $-\frac{1}{4}E_{c,s}^2\left(d+\frac{1}{\gamma_{c,s}}\right)$ | $-1.61\cdot10^{-8}m$ |
| - | $x^2\frac{\partial^2}{\partial\tilde{x}^2}$ | $\mp\frac{1}{4}E_f^2\left(d\cos(d\kappa_f)\pm\frac{1}{6}d^3\kappa_f^2 -\frac{\sin(d\kappa_f)}{\kappa_f}(1-\frac{d^2\kappa_f^2}{2})\right)$ | $+\frac{1}{4}E_{c,s}^2(d+\frac{1}{\gamma_{c,s}}+d^2\frac{\gamma_{c,s}}{2})$ | $+8.57\cdot10^{-9}m$ |

Table 8.2.: Normalization integral ($\Delta\tilde{\epsilon}=1$) and the three different $I_{kl}^{(b)}$, for odd (upper sign) and even modes (lower sign) . The numerical value was calculated from data of Filter No. 1 in [FKS+74]. The total normalization is $\frac{2\beta}{u\omega\mu}\int dxE_y^2 = 1\text{W/m}$. Note that the prefactor $\frac{1}{u\omega\mu}$ is omitted in the Film and Substrate/Cover column.

| Integral | $\Delta\tilde{\epsilon}$ | inside PEC waveguide |
|---|---|---|
| - | 1 | $+\frac{1}{2}E_f^2d$ |
| $I_{kl}^{(b)}$ | $\frac{\partial^2}{\partial\tilde{x}^2}$ | $-\frac{1}{2}E_f^2\kappa_f^2d$ |
| $I_{kl}^{(sg)}$ | $3x\frac{\partial}{\partial\tilde{x}}+x^2\frac{\partial^2}{\partial\tilde{x}^2}$ | …see below |
| - | $x\frac{\partial}{\partial\tilde{x}}$ | $\pm\frac{1}{4}E_f^2d$ |
| - | $x^2\frac{\partial^2}{\partial\tilde{x}^2}$ | $\mp\frac{1}{4}E_f^2\left(d\pm\frac{1}{6}d^3\kappa_f^2\right)$ |

Table 8.3.: Normalization integral ($\Delta\tilde{\epsilon}=1$) and the three different $I_{kl}^{(b)}$ for the PEC waveguide. Derived from Tab. 8.2, for $\kappa_f=\frac{\pi m}{d}$ and $E_s=0$. Note that the prefactor $\frac{1}{u\omega\mu}$ is omitted in the last column.

relevant for the reflection in Eq. (5.2.40) this yields:

$$\hat{C}_{kl}^{(b)} = p_1^{(b)} I_{kl}^{(b)} = 2 \cdot 2903.7/m \tag{8.1.1}$$

$$\hat{C}_{kl}^{(sg)}\Big|_{m=0} = p_0^{(sg)} I_{kl}^{(sg)} = 4197.9/m \tag{8.1.2}$$

$$\hat{C}_{kl}^{(sg)}\Big|_{m=2} = p_2^{(sg)} I_{kl}^{(sg)} = 2098.95/m \tag{8.1.3}$$

$$\tag{8.1.4}$$

In comparison $\hat{C}_{kl}^{(b)} = 2793.28/m$ in [FKS+74], where the scattering was measured for a single boundary, hence half the scattering strength.

# Part II.

# Two-color folded-sandwich entangled photon pair source for quantum teleportation

# 9. Introduction

Single photons from semiconductor quantum dots have proved extremely versatile in quantum optical experiments [SKH+11]. Quantum dots can act as quantum memory [KDH+04] and as a source of entangled photons [TZO+12]. They are a promising candidate for future integrated quantum optical devices.

However, semiconductor quantum dots operate best at visible frequencies and below 1000 nm [BYR+13], because their emission wavelength is bound to available semiconductor materials. While quantum dots excel at short range, e.g. integrated application, the long range communication via optical fibers is restricted.

Quantum interfaces are intended to bridge this gap between *operational* and *transport* wavelengths. Additionally, they can directly connect optical devices that operate at different wavelengths (see Fig. 9.1 a). Quantum interfaces may convert photons directly [YHF13] or teleport the information onto a second photon [BBC93]. In the second case, quantum interfaces provide entangled, non-degenerate, i.e., two-color, photon pairs to teleport quantum information between separate quantum systems (see Fig. 9.1 b). Therefore a source of entangled photons is at the very heart of these quantum interfaces.

There are several techniques to create entangled photons. In this thesis the focus is on down-conversion in non-linear crystals, due to the flexibility in resulting wavelengths. This aim rules out atomic transitions [AD82] or quantum dots [TZO+12] as possible sources in this quantum interface scenario.

To understand pair creation of photons in non-linear crystals, a short introduction to non-linear phenomena in crystals is given in Sec. 10. In these crystals, pairs of photons are created, which are, in general, not yet entangled. The focus in this thesis is not on the creation of photons in non-linear crystals, rather on the creation of entanglement *after* the creation of these pairs. Therefore the introduction to non-linear light-matter interaction will be considerable shorter than the discussion of the entanglement techniques. To create entangled pairs the crystals have to be operated in special schemes. Schemes that are suitable for quantum interface application are discussed in Sec. 11. The detailed analysis of the optical paths will show that two of

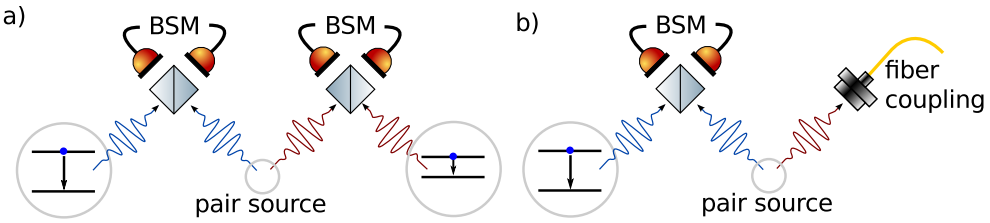


Figure 9.1.: Scheme of entanglement distribution via a two-color entangled photon pair source. a) Two Bell-state measurements (BSM) on photons from two stationary qubit/flying qubit entangled systems and two photons from a two-color entangled photon pair source establish entanglement between two stationary qubits. b) Similarly, a single Bell-state measurement on a photon from a stationary qubit/flying qubit entangled system and one photon from a two-color entangled photon pair source establishes entanglement between the stationary qubit and a telecom photon.

these schemes are very similar concerning the involved light paths. Using this insight, an improved version of the folded-sandwich is proposed in Sec. 12.

Special care has to be taken to compensate the dispersion in this setup. This is discussed in Sec. 12.3. The final theoretical Sec. 9.1 explains how entanglement can be measured in such a scheme. Sec. 13.1 is a detailed description of the experimental setup, followed by the results in Sec. 13.

The results of this part of the thesis are discussed in [DMK+15] (accepted for publication in Applied Physics B).

## 9.1. Quantifying and measuring entanglement

Entanglement is a quantum mechanical effect that has no classical analogy. A state is entangled when it can not be written as a product state. For example, the Bell state

$$|\phi^+\rangle = \frac{1}{\sqrt{2}}\left(|VV\rangle + |HH\rangle\right) \tag{9.1.1}$$

is a superposition of the two-photon state $|VV\rangle$ and the state $|HH\rangle$. To quantify the entanglement, the Bell-state fidelity can be measured. It is defined as

$$F_{\phi^+} = \langle\phi^+|\rho|\phi^+\rangle \tag{9.1.2}$$

If the fidelity is greater than $\frac{1}{2}$ the state $\rho$ is entangled [WGP+07; TH00]. This will be shown in two different ways. After a general approach, the fidelity will be calculated directly for an entangled and a separable state.

## 9.2. Schmidt rank and fidelity

Any two particle state $|\psi\rangle$ within the Hilbert space $H_1 \otimes H_2$, i.e., $|\psi\rangle \in H_1 \otimes H_2$, can be written as a Schmidt decomposition.

$$|\psi\rangle = \sum_{i=1}^{m} \alpha_i |u_k\rangle \otimes |v_i\rangle \tag{9.2.1}$$

where $|u_k\rangle \in H_1$, $|v_i\rangle \in H_2$, and $\alpha_i \geq 0$. For example the Bell state $|\phi^+\rangle$ is a Schmidt decomposition with two non-zero $\alpha_1 = \alpha_2 = \frac{1}{\sqrt{2}}$ and $|u_1\rangle = |v_1\rangle = |H\rangle$ and $|u_2\rangle = |v_2\rangle = |V\rangle$. The Schmidt rank is now defined as the number of non-zero coefficients $\alpha$. Consequently states with Schmidt rank greater than one are entangled. Now it can be proven that if the fidelity of some state $\rho$

$$F_{\phi^+} = \langle \phi^+ | \rho | \phi^+ \rangle > \frac{1}{2} \tag{9.2.2}$$

then the state $\rho$ is entangled. The proof (see [TH00], and [WGP+07] for an introduction) is general but provides little physical insight. Therefore it won't be discussed here. It is more instructive to calculate the fidelity directly for the desired setup. This is done in the next section.

## 9.3. Fidelity analysis of mixed and entangled state

The condition sketched in the last section is unsatisfying because it has no intuitive explanation. Therefore, two states are directly analyzed to see under which condition the fidelity exceeds $\frac{1}{2}$. Here, the discussion is restricted to pairs of horizontally and vertically polarized photons, which resembles the experimental setup, the folded sandwich source, described in the upcoming sections. This folded-sandwich source creates horizontally and vertically polarized photons. If properly set up, the photons are entangled. Otherwise, the source may as well create a random mixture of horizontally and vertically polarized pairs with equal probability. The density matrix of such a mixture is

$$\rho_{rand} = \frac{1}{2}|HH\rangle\langle HH| + \frac{1}{2}|VV\rangle\langle VV| \tag{9.3.1}$$

This state is obviously not entangled, because there are no "off-diagonal" elements such as $|VV\rangle\langle HH|$. The fidelity of that state is calculated as

$$F_{\phi^+} = \langle\phi^+|\rho_{rand}|\phi^+\rangle = \frac{1}{2} \tag{9.3.2}$$

Now suppose that the source is producing entangled photons, but not exclusively. Some pairs are entangled, while others are still a random mixture. Then the density matrix reads

$$\rho_p = p|\phi^+\rangle\langle\phi^+| + (1-p)\rho_{rand} \tag{9.3.3}$$

Using the definition $\rho_{off} = \frac{p}{2}(|HH\rangle\langle VV| + |VV\rangle\langle HH|)$ this expression simplifies to

$$\rho_p = \rho_{rand} + \rho_{off} \tag{9.3.4}$$

The fidelity of that state is

$$\begin{aligned} F_{\phi^+} &= \langle\phi^+|\rho_p|\phi^+\rangle && (9.3.5)\\ &= \langle\phi^+|\rho_{rand}|\phi^+\rangle + \langle\phi^+|\rho_{off}|\phi^+\rangle && (9.3.6)\\ &= \frac{1}{2} + \langle\phi^+|\rho_{off}|\phi^+\rangle && (9.3.7)\\ &= \frac{1}{2} + \frac{p}{2} && (9.3.8) \end{aligned}$$

Note that $p$ was introduced as fraction of the mixture that is entangled. Hence, if any part of the state is entangled, then the fidelity is greater than $\frac{1}{2}$.

## 9.4. Extracting the fidelity from the count rates

In the last sections it was shown that entangled and separable states can be distinguished by looking at the fidelity of the state. This raises the question: How can the fidelity be measured? In this section it is shown that the Bell state fidelity

$$F_{\phi^+} = \langle\phi^+|\rho|\phi^+\rangle \tag{9.4.1}$$

can be expressed in terms of the two-photon visibilities

$$= \frac{1}{4}(1 + V_{HV} + V_{DA} - V_{LR}) \tag{9.4.2}$$

The two-photon visibilities

$$V_{ij} = \frac{N_{ii} + N_{jj} - (N_{ij} + N_{ji})}{N_{ii} + N_{jj} + N_{ij} + N_{ji}} \tag{9.4.3}$$

are defined in terms of the count rates $N_{ij}$ for polarization state $i$ and it's orthogonal counter part $j$. This is, tuples of horizontal (H)/vertical (V), diagonal (D)/anti-diagonal (A), or circular left (L)/right (R) polarization. To see the relationship between the fidelity and the two-photon visibilities, the density matrix is written as

$$\rho = \sum_{k,l=1}^{4} \rho_{kl} |u_k\rangle\langle u_l| \tag{9.4.4}$$

The $|u_k\rangle$ are chosen as the two-photon polarization states

$$|u_1\rangle = |HH\rangle \tag{9.4.5}$$
$$|u_2\rangle = |HV\rangle \tag{9.4.6}$$
$$|u_3\rangle = |VH\rangle \tag{9.4.7}$$
$$|u_4\rangle = |VV\rangle \tag{9.4.8}$$

With these, the fidelity can be written as

$$F_{\phi^+} = \sum \rho_{kl} \langle \phi^+ | u_k \rangle \langle u_l | \phi^+ \rangle \tag{9.4.9}$$
$$= \frac{1}{2} (\rho_{11} + \rho_{14} + \rho_{41} + \rho_{44}) \tag{9.4.10}$$
$$= \frac{1}{2} (P_H + \rho_{14} + \rho_{41} + P_V) \tag{9.4.11}$$

In the chosen $HV$ basis, the diagonal elements $\rho_{11}$ and $\rho_{44}$ are the probability $P_H$ and $P_V$ to find a photon in the state $|HH\rangle$ and $|VV\rangle$, respectively. This probability can be measured as

$$P_i = \frac{N_{ii}}{N_{ii} + N_{ij} + N_{ji} + N_{jj}} = \frac{N_{ii}}{N_{tot}} \tag{9.4.12}$$

In contrast $\rho_{14}$ and $\rho_{41}$ can not directly be expressed as such probabilities. Therefore additional bases come into play. These are

$$|D\rangle = \frac{|H\rangle + |V\rangle}{\sqrt{2}} \tag{9.4.13}$$

$$|A\rangle = \frac{|H\rangle - |V\rangle}{\sqrt{2}} \tag{9.4.14}$$

$$|R\rangle = \frac{|H\rangle + i|V\rangle}{\sqrt{2}} \tag{9.4.15}$$

$$|L\rangle = \frac{|H\rangle - i|V\rangle}{\sqrt{2}} \tag{9.4.16}$$

The corresponding two particle state is obtained as

$$|DD\rangle = |D\rangle|D\rangle \tag{9.4.17}$$

$$= \frac{1}{2}\left(|HH\rangle + |HV\rangle + |VH\rangle + |HH\rangle\right) \tag{9.4.18}$$

and for $|LL\rangle, |RR\rangle, |LL\rangle$ accordingly. Calculating

$$P_D + P_A = \langle DD|\rho|DD\rangle + \langle AA|\rho|AA\rangle \tag{9.4.19}$$

and using $\mathrm{Tr}\,\rho = \rho_{11} + \rho_{22} + \rho_{33} + \rho_{44} = 1$, yields

$$= \frac{1}{2}\left(1 + \rho_{14} + \rho_{41} + \rho_{23} + \rho_{32}\right) \tag{9.4.20}$$

The third basis yields

$$P_R + P_L = \frac{1}{2}\left(1 - \rho_{14} - \rho_{41} + \rho_{23} + \rho_{32}\right) \tag{9.4.21}$$

and thus

$$P_D + P_A - (P_R + P_L) = \rho_{14} + \rho_{41} \tag{9.4.22}$$

Using these results, the Bell state fidelity can be written as

$$F_{\phi^+} = \frac{1}{2}\left(P_D + P_A - (P_R + P_L) + P_H + P_V\right) \tag{9.4.23}$$

The fidelity is now expressed as a function of the probabilities in the three different bases. To express the fidelity in terms of the two-photon visibilities the definition of the two-photon visibilities (Eq. 9.4.3) is rewritten as

$$V_{ij} + 1 = \frac{2\left(N_{ii} + N_{jj}\right)}{N_{tot}} \tag{9.4.24}$$

using Eq. (9.4.12), this can be written as

$$= 2\left(P_i + P_j\right) \tag{9.4.25}$$

Plugging this into Eq. (9.4.23) yields

$$F_{\phi^+} = \frac{1}{4}\left(1 + V_{HV} + V_{DA} - V_{LR}\right) \tag{9.4.26}$$

To determine the fidelity, the one-photon visibilities are measured (see Sec. 13.4) in three different bases. The one-photon visibility is defined as

$$v_i = \frac{N_{ii} - N_{ij}}{N_{ii} + N_{ij}} = \frac{A_i}{C_i} \tag{9.4.27}$$

In the measurement the basis in one arm is fixed, while the basis in the other arm is rotated between $i$, and its orthogonal counter part $j$. The one-photon visibilities are then fitted with a sine function $A_i \sin(4\phi_{HWP} + \Theta) + C_i$. Since $C_i = (N_{ii} + N_{ij})/2$ and $A_i = (N_{ii} - N_{ij})/2$, the two-photon visibilities can be rewritten as

$$V_{ij} = \frac{A_i + A_j}{C_i + C_j}\,. \tag{9.4.28}$$

## 9.5. Single measurement to quantify entanglement

In general, six probabilities $P_i$ (see Eq. (9.4.23) have to be measured, to determine the fidelity. From the six probabilities $P_i$, all four Bell state fidelities can be calculated, for an arbitrary state $\rho$. For a single Bell state fidelity, such as $F_{\phi^+}$, fewer measurements are necessary. The fidelity $F_{\phi^+}$ is determined by only four matrix elements, as calculated in Eq. (9.4.10). Therefore four measurements should be sufficient. Here, it is assumed that the source produces a state like the one defined in Eq. (9.3.3) Under this assumption as single measurement should be sufficient to determine entanglement. Such a measurement is described in the following.

Setting both polarizers in each arm to the same at angle $\Theta$, projects the state into

$$|P_\Theta\rangle = \cos\Theta|HH\rangle + \sin\Theta|VV\rangle \tag{9.5.1}$$

this yields

$$\langle P_\Theta|\rho_{rand}|P_\Theta\rangle = \frac{1}{2}\cos^2\Theta + \frac{1}{2}\sin^2\Theta \tag{9.5.2}$$
$$= \frac{1}{2} \tag{9.5.3}$$
$$\langle P_\Theta|\rho_{off}|P_\Theta\rangle = \frac{p}{2}\cos\Theta\sin\Theta + \frac{p}{2}\sin\Theta\cos\Theta \tag{9.5.4}$$
$$= \frac{p}{2}\sin 2\Theta \tag{9.5.5}$$
$$\langle P_\Theta|\rho_p|P_\Theta\rangle = \frac{1}{2} + \frac{p}{2}\sin 2\Theta \tag{9.5.6}$$

Consequently, any oscillation with periodicity $2\Theta$ in the measurement indicates entanglement. Note, that the projection state $P_\Theta$ is in fact the Bell state $\phi^+$ for $\Theta = \pi/4$. Therefore $\langle P_{\pi/4}|\rho_p|P_{\pi/4}\rangle = F_{\phi^+}$. This single measurement is sufficient to calculate the fidelity.

Now the coincidences are measured, while changing the angle $\Theta$. Then, the value of $p$ can be extracted from a sinusoidal fit $f(\Theta) = A\sin 2\Theta + C$. The minimum $N_{min}$ and maximum count rates $N_{max}$ are given by

$$N_{max}/N_{tot} = \frac{1}{2} + \frac{p}{2} = C + A \tag{9.5.7}$$
$$N_{min}/N_{tot} = \frac{1}{2} - \frac{p}{2} = C - A \tag{9.5.8}$$
$$\tag{9.5.9}$$

This yields

$$\frac{N_{min} - N_{max}}{N_{min} + N_{max}} = p = \frac{A}{C} \tag{9.5.10}$$

This is exactly the definition of the one-photon visibility

$$v_\Theta = \frac{N_{max} - N_{min}}{N_{max} - N_{min}} \tag{9.5.11}$$

So it turns out that $p$ can be identified as the one-photon visibility, measured in the Bell-state basis $|\phi^+\rangle$, $|\phi^-\rangle$

$$v = \frac{A}{C} = p \tag{9.5.12}$$

Consequently the relationship between the measured probability and the visibility reads

$$\langle P_\Theta | \rho_p | P_\Theta \rangle = \frac{1}{2}(1 + v \sin 2\Theta) \tag{9.5.13}$$

which is correctly used but incorrectly typed in [SRJ+13].

# 10. Photon pair creation in non-linear periodically poled crystals

As discussed in the preface, the higher order contributions to the polarization

$$P = \epsilon_0 \chi E + \epsilon_0 \chi^{(2)} E^2 + \epsilon_0 \chi^{(3)} E^3 + \cdots \tag{10.0.1}$$

can mix different frequencies. This can easily be seen when assuming the E-Field to be a superposition of two monochromatic waves of frequencies $\omega_1, \omega_2$

$$E = E_1 \exp(-i\omega_1 t) + E_2 \exp(-i\omega_2 t) + \text{c.c.} \tag{10.0.2}$$

which yields

$$\chi^{(2)} E^2 = \chi^{(2)} \left( \underbrace{E_1^2 e^{-i2\omega_1 t} + E_2^2 e^{-i2\omega_2 t}}_{SHG} + \underbrace{E_1 E_2 e^{-i(\omega_1 - \omega_2)t}}_{DFG} + \underbrace{E_1 E_2 e^{-i(\omega_1 + \omega_2)t}}_{SFG} + \text{c.c.} + \text{const.} \right) \tag{10.0.3}$$

The different parts are the second-harmonic (SHG), the difference (DFG) and sum frequency generation (SFG). Here, the DFG is of importance and will be discussed in the following. For two incident waves $\omega_1$, $\omega_2$ the non-linear interaction generates a third wave, with frequency $\omega_1 - \omega_2$. But even in the absence of a second wave $\omega_2$, the process takes place spontaneously. As a result two photons of frequency $\omega_2$ and $\omega_3 = \omega_1 - \omega_2$ are created [Boy03]. This process is called spontaneous parametric down-conversion. The general convention is that the short wavelength photon is called signal, while the other is called idler. The frequency relation between pump, signal and idler photon fulfills the energy conservation.

For efficient photon conversion, the momentum conservation needs to be fulfilled. If the momentum conservation is not fulfilled, i.e.

$$\Delta k = k_p - k_s - k_i \neq 0 \tag{10.0.4}$$

then the amplitude, and consequently the power of the generated waves oscillates around zero. Therefore creating photon pairs requires a delicate *phase-matching*.

To enable more flexible photon-pair creation periodically poled crystals are used. In these crystals the crystallographic $c$-axis is periodically inverted ("poled"). When the poling coincides with twice the coherent build up length [Boy03] it circumvents the oscillation around zero. The poling length can be adjusted by temperature tuning, such that

$$\Delta k = k_p - k_s - k_i - \frac{2\pi}{2L_{coh}} = 0 \tag{10.0.5}$$

where $L_{coh}$ is the coherent build up length. In the momentum picture, this periodic lattice balances out the momentum mismatch. This technique is therefore called *quasi phase-matching*.

The highest conversion efficiency in bulk crystals can be achieved with periodically poled $LiNbO_3$ (ppLN). ppLN has a very high susceptibility $\chi^{(2)}_{333}$ [Boy03], which can result in high efficiency for conversation, where all three photons have the same polarization (type-0) [FNM+07].

Non-linear crystals can be used to create entangled photons directly [KMW+95]. In this case entanglement is created in the crystal by overlapping the paths of vertically and horizontally polarized photons. Here, another common approach will be followed. Entanglement will be created by overlapping paths of horizontally and vertically polarized photons created in different crystals.

# 11. Different schemes for entangling photons from down-conversion sources

There exists a number of different schemes to create entangled photons from down-conversion sources. Quantum interfaces should be able to send at least one of its photons into a fiber for long range communication. Fiber coupling is best achieved using collinear down-conversion schemes. Furthermore the collinear alignment enables further integration and can be used in monolithic design (such as [HHP+09]). These designs will become increasingly important for satellite based quantum key distribution [WYL+13], where certain space technology readiness levels have to be met.

Historical there are two different basic collinear arrangements, the Sagnac [ST04] and the crossed-crystal configuration [TW08; KFW06]. Both have their advantages and their problems. Both schemes have been optimized and used to create novel schemes.

Recently, *Steinlechner, et al.* presented the folded-sandwich configuration, which simplifies the crossed-crystal scheme, while adding inherent phase stability [SRJ+13]. The phase stability has so far being the advantage of the Sagnac configuration. The folded-sandwich was proposed as a folded version of the crossed-crystal configuration, which is often referred to as "sandwich" configuration. The folded-sandwich is based on wavelength-dependent polarization rotation [SRJ+13].

The basic Sagnac configuration is not well suited for quantum interface application which requires strongly non-degenerate photons that are several hundred nanometers apart [SSB+13]. So far only setups with nearly non-degenerate photons have been proposed. To overcome this restriction, *Stuart et al.* presented a two-crystal Sagnac source [SSB+13], which produces highly non-degenerate photons.

So far the two-crystal Sagnac source seems to be the most suitable source for quantum interface applications, as it is the only collinear source that has so far being demonstrated to create highly non-degenerate photons. In the next section, it is argued

that the two-crystal Sagnac source is in fact equivalent to the folded-sandwich, up to one extra crystal passage. In the section thereafter this insight is used to propose a novel scheme, the *geometrical* folded-sandwich

## 11.1. Similarities between the different schemes

In this section it will be shown that the two-crystal Sagnac and the crossed crystal (and consequently the folded-sandwich) configuration are equivalent, up to an extra passage through the non-linear crystal. The two schemes are shown in Fig. 11.1 a) and b). The two possible paths in the two-crystal Sagnac configuration (clockwise, and counter-clockwise) are shown. The spatial separation of these two paths yields the fundamental paths of the crossed-crystal configuration. The only difference is that in the crossed-crystal configuration the first pair $|HH\rangle$ takes a "detour" through the second crystal. The rotation of the second crystal can be replaced by a half wave plate. Replacing the half wave plate by a quarter wave plate and a mirror yields the folded-sandwich scheme. So the only difference between the two setups is one additional passage through the non-linear crystal. For that reason, the folded sandwich configuration includes a compensation crystal, which compensates the additional dispersion acquired in this passage. This compensation is necessary to delete which-way information, acquired by the first pair when passing through the vertical crystal in Fig. 11.1 b) and c). The compensation crystal is crucial and discussed in detail in Sec. 12.3. In the two-crystal Sagnac configuration the second non-linear crystal acts as compensation crystal. An additional compensation crystal is not necessary. Either way, both setups require two crystals.

The use of two non-linear crystals in a Sagnac loop has the advantage that no extra compensation is needed. The compensation is strongly wavelength dependent, therefore, it poses a strong restriction on the tunability. However, the three different wavelengths in the Sagnac loop require a special three-color beam splitter. Besides being expensive, it may introduce wavelength dependence. Additionally, it is very difficulty to align a three color Sagnac interferometer [SRJ+13]. Thus, it is desirable to use the simple folded-sandwich configuration. In the next section, it is shown how the folded-sandwich configuration can be optimized to yield strongly degenerate photons and tunability.

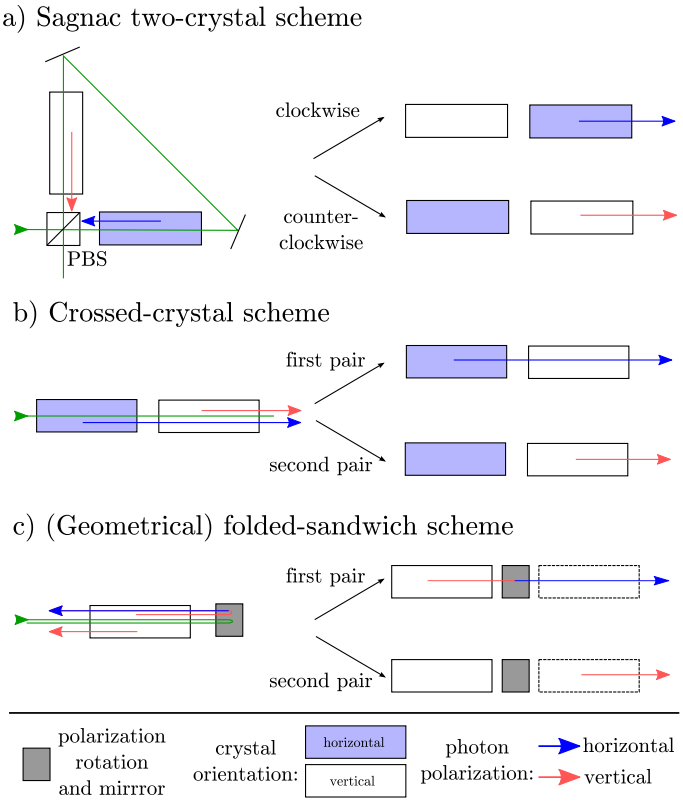


Figure 11.1.: Different collinear down-conversion schemes. A photon can be created if a horizontally (vertically) polarized pump photon passes through a horizontally (vertically) oriented crystal (type-0). In all schemes, a pair is created in the first *or* in the second crystal. a) The two possible paths in the two-crystal Sagnac loop. In both paths the photon pair is generated in the second crystal. In the (counter) clockwise path, the photon pair is generated vertically (horizontally) because the second crystal has vertical (horizontal) orientation. b) The two paths in the crossed-crystal scheme. The first photon pair (horizontally polarized) is created in the first crystal and accumulates an extra phase while passing through the second crystal. The second photon pair is created in the last crystal, just as the counter-clockwise photon in the Sagnac configuration. The only difference between the two schemes is the extra crystal passage of the horizontal photon. c) Folded-sandwich configuration. The polarization rotation (gray box) rotates the first pair. This is equivalent to the first pair in the crossed-crystal scheme, only that instead of the crystal the light polarization is rotated. In the folded-sandwich configuration the second crystal is the mirrored first crystal. The (diagonal or unpolarized) pump beam is depicted in green.

# 12. Geometrical folded-sandwich scheme and setup

## 12.1. Principles

The folded-sandwich scheme is based on a wavelength dependent polarization rotation. An achromatic quarter wave plate is used, which acts on signal and idler as a $\lambda/4$ and on the pump photon as a $\lambda$-plate. Thus, it is chosen in such a way to have no effect on the pump photon [SRJ+13]. Using such quarter wave plates makes the setup wavelength dependent.

In this thesis a wavelength-independent source is proposed. The setup can be made wavelength-independent in two steps. Instead of "rotating" the vertically polarized pump light by $\lambda$, the pump beam can be set to diagonal polarization. The diagonal polarization is on the fast axis of the quarter wave plate. Thus no rotation will occur. Consequently, the quarter wave plate acts as a wavelength independent rotator. Unfortunately the angle of the fast axis of the achromatic wave plate is wavelength dependent [Pan55]. Fig. 12.1 a) shows the wavelength-dependence of the angle of the fast axis for a typical (super) achromatic quarter wave plate. For pump light of 532 nm, the shift of the angle of the fast axis is still acceptable, but for 405 nm, another typical pump frequency, the offset diverges.

Custom made achromatic wave plates might yield the desired properties. But there is a much simpler solution. A Fresnel rhomb is a suitable replacement for the achromatic wave plate. The Fresnel rhomb yields a rotation of $\lambda/4$ after two consecutive internal reflections. This rotation is wavelength dependent, as shown in Fig. 12.1 b). However, the "fast axis" of the rhomb is defined geometrically, an thus it it is wavelength independent.

Replacing the wavelength dependent polarization rotation with a wavelength independent counter-part makes the scheme a *geometrically* folded sandwich. It makes the folded-sandwich ready for highly non-degenerate photon creation. Furthermore, wavelength-independence is an important requisite to create a tunable source. With

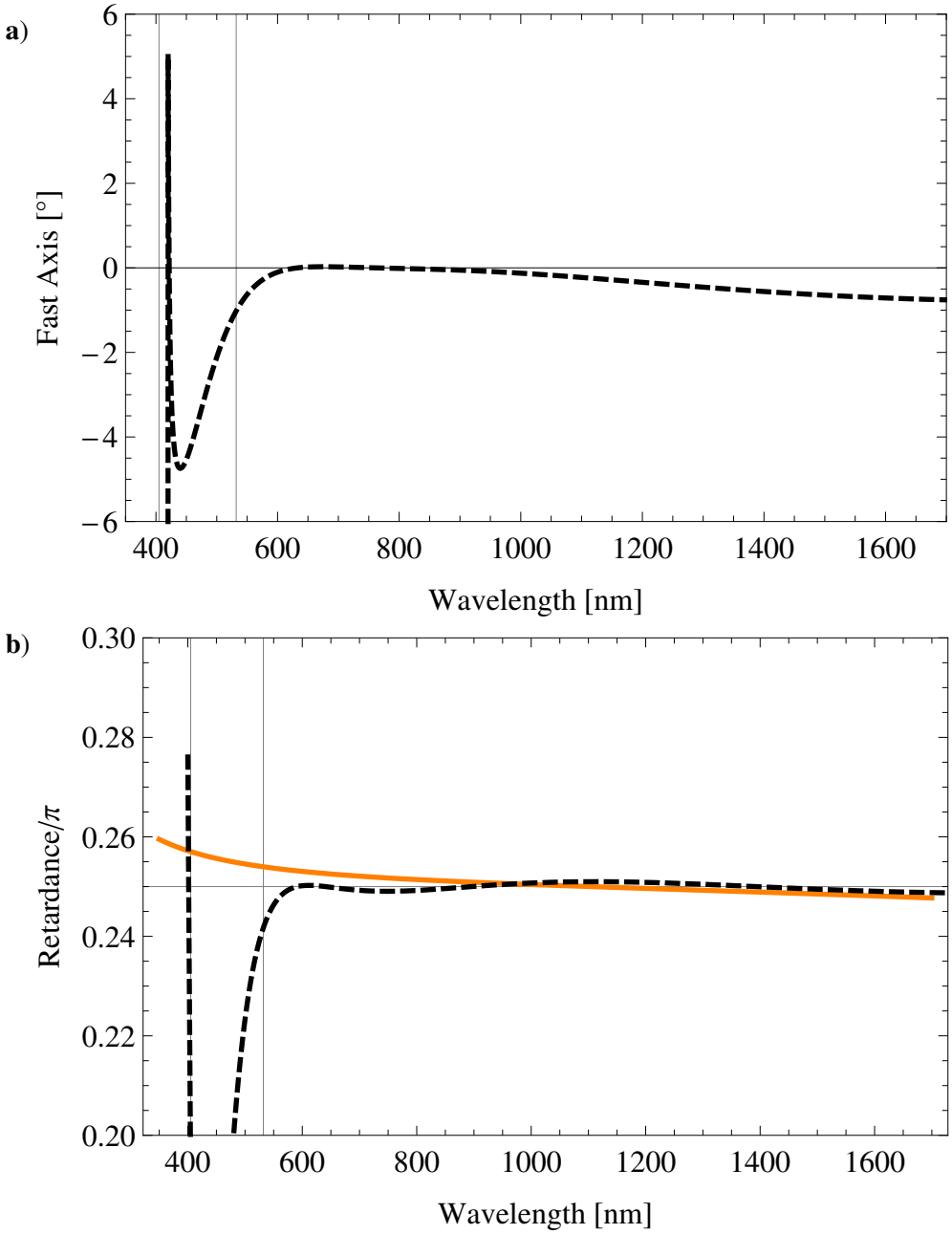


Figure 12.1.: a) Wavelength dependence of the angle of the fast axis of an achromatic quarter wave plate. b) Wavelength dependence of retardance of Fresnel rhomb (orange, ——) and achromatic quarter wave plate (dashed black, - - -). Data for typical achromatic wave plate (Thorlabs SAQWP05M-1700) and BK7 Fresnel rhomb (B. Halle RFV500 cut for shear angle 54.8°). Vertical lines indicate typical laser wavelength at 405 nm and 532 nm.

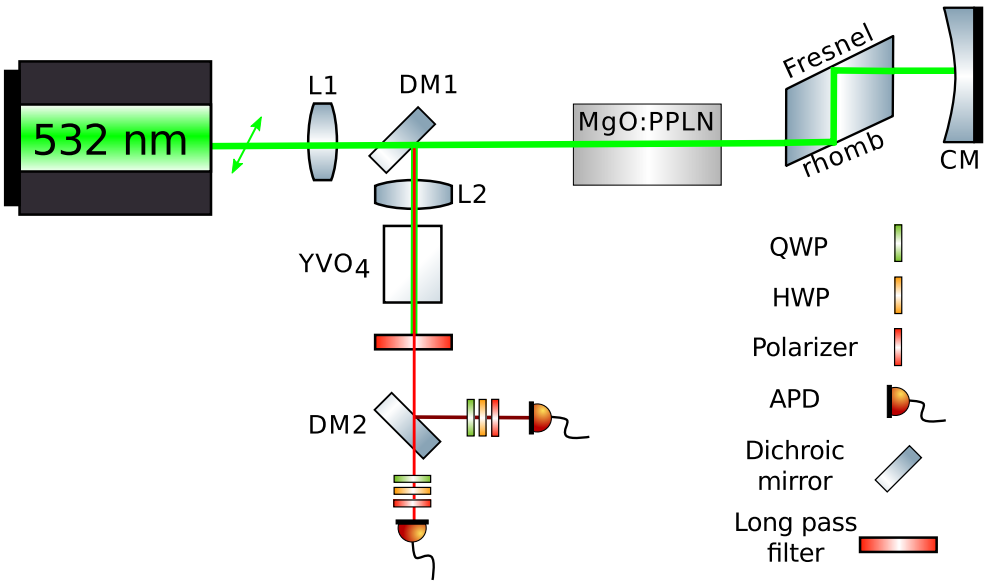


Figure 12.2.: Setup based on one periodically poled lithium niobate crystal (ppLN) doped with approx. 5% magnesium oxide (MgO), of length $L = 40$ mm. The crystal temperature is controlled via a crystal oven (not shown). The Fresnel rhomb acts as a geometrical quarter wave plate. The concave mirror (CM) reflects the light back into the crystal. The focusing (L1) and collimation (L2) lenses adjust the beam width. The first dichroic mirror (DM1) separates pump and down converted photons. The second dichroic mirror (DM2) separates signal and idler photons. The phase compensation crystal consists of several $YVO_4$ slabs to allow for broad tunability, with additional crystal oven (not shown). Component icons from [Ale].

these features the geometrical folded-sandwich becomes a suitable candidate for quantum interface application. Optimizing existing schemes with geometrical components is a technique that has been successfully demonstrated for single-crystal Sagnac sources [HHP+09].

## 12.2. Setup

The setup is shown in Fig. 12.2. The diagonal polarized pump (532 nm CW) light is focused into the non-linear crystal. The crystal is periodically poled $LiNbO_3$, (ppLN) doped with 5% MgO (hcp Photonics) of length 40 mm with a facet 4 mm×1 mm. It is type-0 phase matched, i.e., pump and created photons all in plane. The poling period is 7 µm, with multiple gratings.

In this first pass, the vertical components of the diagonal pump beam create a vertically polarized pair with a certain probability, depending on the pump power. This pair and the pump beam propagate through the Fresnel rhomb. The Fresnel rhomb is oriented at 45°, such that it acts on the vertically polarized photons as a quarter wave plate. The vertical pair leaves the rhomb circularly polarized. The diagonal pump beam passes the Fresnel rhomb without modification.

The concave mirror (CM) reflects the light back onto the Fresnel rhomb and into the crystal. On the way back the Fresnel rhomb rotates the circularly polarized pair into a horizontally polarized pair. The diagonal pump beam and the horizontally polarized pair pass the non-linear crystal a second time. Again, the vertical part of the diagonal pump beam can create a vertically polarized pair with a certain probability. The probability can be adjusted with the pump power. The pump power is chosen such that, on average, only one pair is created for the double pass through the crystals. The pump beam and one photon pair exit the crystal to incident on the dichroic mirror (DM1). Here, the pump light is separated from the photon pair. The photon pair is collimated and directed onto a compensation crystal. The compensation crystal compensates the difference in dispersion of the first and the second pass. This is explained in detail in the next section. After the compensation crystal, the beam is directed onto a polarization filter and wave plates for entanglement measurement (see Sec. 9.1).

## 12.3. Compensation crystal: Deleting which-crystal information

The photon pair is not yet entangled. The desired entangled state is

$$\psi = \frac{1}{\sqrt{2}}\left(|VV\rangle + e^{i\phi}|HH\rangle\right) \tag{12.3.1}$$

However, due to the extra passage trough the rhomb and the non-linear crystal the second pair acquired not only a different phase $\phi$, but a different dispersion $\frac{d\phi}{d\lambda}$. The dispersion, i.e., the broadening of the first photon wave packet, leaks which-crystal information, which destroys the entanglement.

The compensation crystal has to eliminate the difference in the dispersion, to delete the which-crystal information. The extra phase $\phi$ of the first pair $|VV\rangle$ is given by

$$\phi(\lambda_s, \lambda_i, T) = \left(\frac{n_o(\lambda_s, T)}{\lambda_s} + \frac{n_o(\lambda_i, T)}{\lambda_i}\right) L_{crystal} \tag{12.3.2}$$

$$+ \left(\frac{n_r(\lambda_s, T)}{\lambda_s} + \frac{n_r(\lambda_i, T)}{\lambda_i}\right) 2L_{rhomb} \tag{12.3.3}$$

where $n_r$ is the refractive index of the Fresnel rhomb (BK7 glass) and $n_o$ is the refractive index of the ordinary (vertical) non-linear crystal axis. The refractive index of the non-linear crystal depends on the crystal temperature $T$, and the wavelength of the down converted signal and idler photon $\lambda_{s/i}$. The compensation crystal adds another phase $\tilde{\phi}$ that has to be chosen in such a way that the flat phase condition is fulfilled

$$\frac{d}{d\lambda}\Big|_{\lambda_{s,i}} \left(\phi + \tilde{\phi}\right) = 0 \tag{12.3.4}$$

$YVO_4$ is chosen as birefringent crystal of length $\tilde{L}$, which adds a phase of

$$\tilde{\phi}(\lambda_s, \lambda_i, T) = \left(\frac{\tilde{n}_o(\lambda_s, T)}{\lambda_s} + \frac{\tilde{n}_o(\lambda_i, T)}{\lambda_i} - \left(\frac{\tilde{n}_e(\lambda_s, T)}{\lambda_s} + \frac{\tilde{n}_e(\lambda_i, T)}{\lambda_i}\right)\right) \tilde{L} \tag{12.3.5}$$

$$\tag{12.3.6}$$

where $\tilde{n}_{o/e}$ is the refractive index of ordinary and extra-ordinary axis of $YVO_4$.

There are very different estimations of the refractive index of $YVO_4$ in the literature. For example, for a signal and idler wavelength of $\lambda_s = 894.3\,\text{nm}$ and $\lambda_i = 1313.1\,\text{nm}$, the predicted length of the compensation crystal $\tilde{L}$ varies between 138.3 mm (manu-

facturer specification [Foc]), 154.0 mm [ZLC+10], and 172 mm [ST14]. The crystal length dependence of the flat phase condition is shown in Fig. 12.3. For ±1 mm crystal length, the flat phase position varies around ±50 nm. Thus with a few 1 mm slabs the compensation crystal can be tuned by several hundred nanometer.

Note that the acquired phase $\phi + \tilde{\phi}$ depicted in Fig. 12.3 is several thousands times $2\pi$. To fine tune the phase between 0 and $\pi$, i.e., between the Bell states

$$|\phi^+\rangle = \frac{1}{\sqrt{2}}(|VV\rangle + |HH\rangle) \tag{12.3.7}$$

and

$$|\phi^-\rangle = \frac{1}{\sqrt{2}}(|VV\rangle - |HH\rangle) \tag{12.3.8}$$

the temperature of the compensation crystal is tuned. A phase shift of $\pi$ is expected for $\sim 2.4°C$ temperature difference [SRJ+13; ZLC+10], which is in good agreement with our measurement (see master thesis [Mül15] for details).

After the compensation crystal, signal and idler are separated at a dichroic mirror (DM2). In each of the separate arms, $\lambda$-plates and polarizer allow for measurement of different polarization states. Each arm is then coupled to a single mode fiber. The single mode fibers are connected to a spectrograph or APD for spectral or statistical measurement.

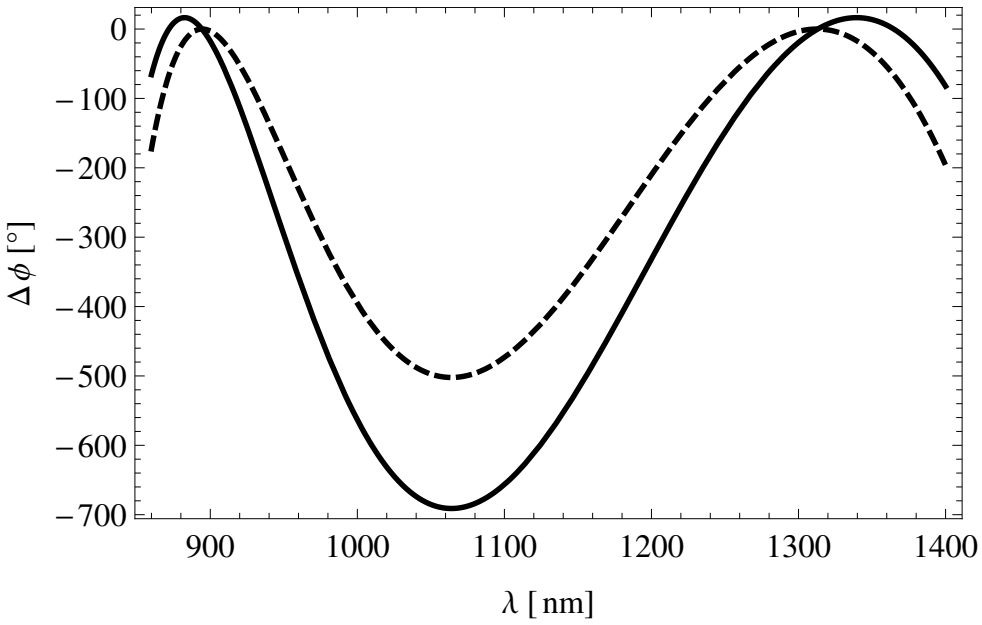


Figure 12.3.: Compensated phase $\Delta\phi = \phi + \tilde{\phi}$ is plotted against the wavelength for different lengths of the compensation crystal. Calculated for $\tilde{L} =$ 138 mm (black, ——) and $\tilde{L} = 139$ mm (dashed black, - - -).

# 13. Results

## 13.1. Tunability

The crystal oven of the non-linear crystal can be heated up to 160°$C$. The measured signal photon wavelength is shown in Fig. 13.1. The tuning range for the chosen 7 µm grating, ranges from 870 nm to 1100 nm, this is roughly 130 nm. The corresponding idler wavelength span from 1345 nm to 1124 nm (see master thesis [Kre15] for details). The measurement was performed without the compensation crystal.

## 13.2. Ensuring indistinguishable photons

To create entangled photons, photons created in the first and in the second path have to be indistinguishable. Signatures of the individual paths yields which-crystal, i.e., which-path, information, which suppresses the entanglement. There are two major sources of which-path information, the shape of the photons in the spectral domain and in the time domain. The spectral width of the photons is mainly determined by the length of the crystal [TC95] (for this setup calculated in [Mül15]). Even though the crystal length is obviously the same for both ways through the crystal, the *effective* crystal length may differ. This is especially the case when the beam width in the two passes differs. If the beam is focused too tightly, it diverges rapidly after the focal point. It will thus experience an effectively shorter crystal. Careful alignment is necessary to ensure comparable focusing conditions in each pass. The resulting spectra of the first and the second pass after careful alignment are shown in Fig. 13.2.

The second source of which-crystal information is the dispersion in the setup, discussed in Sec. 12.3. The optimal crystal length is unknown, but it is most likely between 14 cm and 17 cm. The optimal crystal length is an additional optimization, which can further enhance the entanglement. For a proof-of-principle measurement the entanglement is now examined without further optimization.

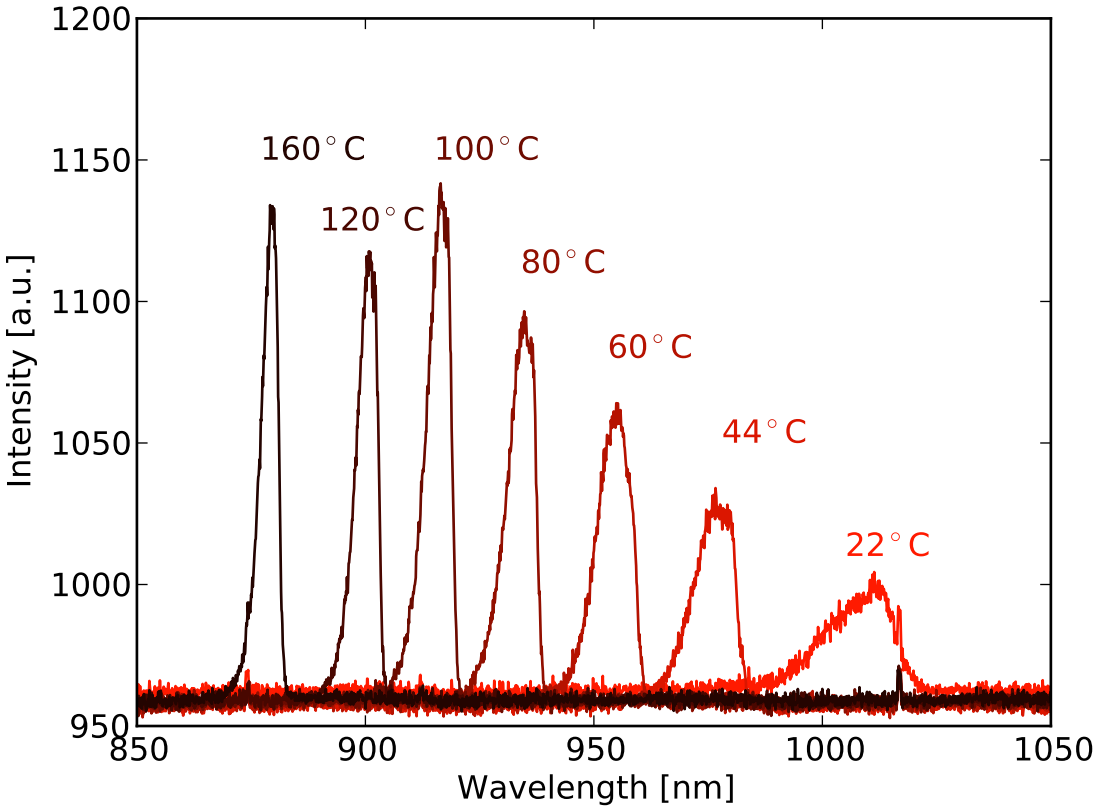


Figure 13.1.: Spectra of signal photons for different non-linear crystal temperatures. The decreasing intensities are due to decreasing sensibility of the spectrometer CCD camera. The broadening of the spectrum is due to the increasing degeneracy [SRJ+13]. At 1064 nm the signal and idler photons are degenerated.

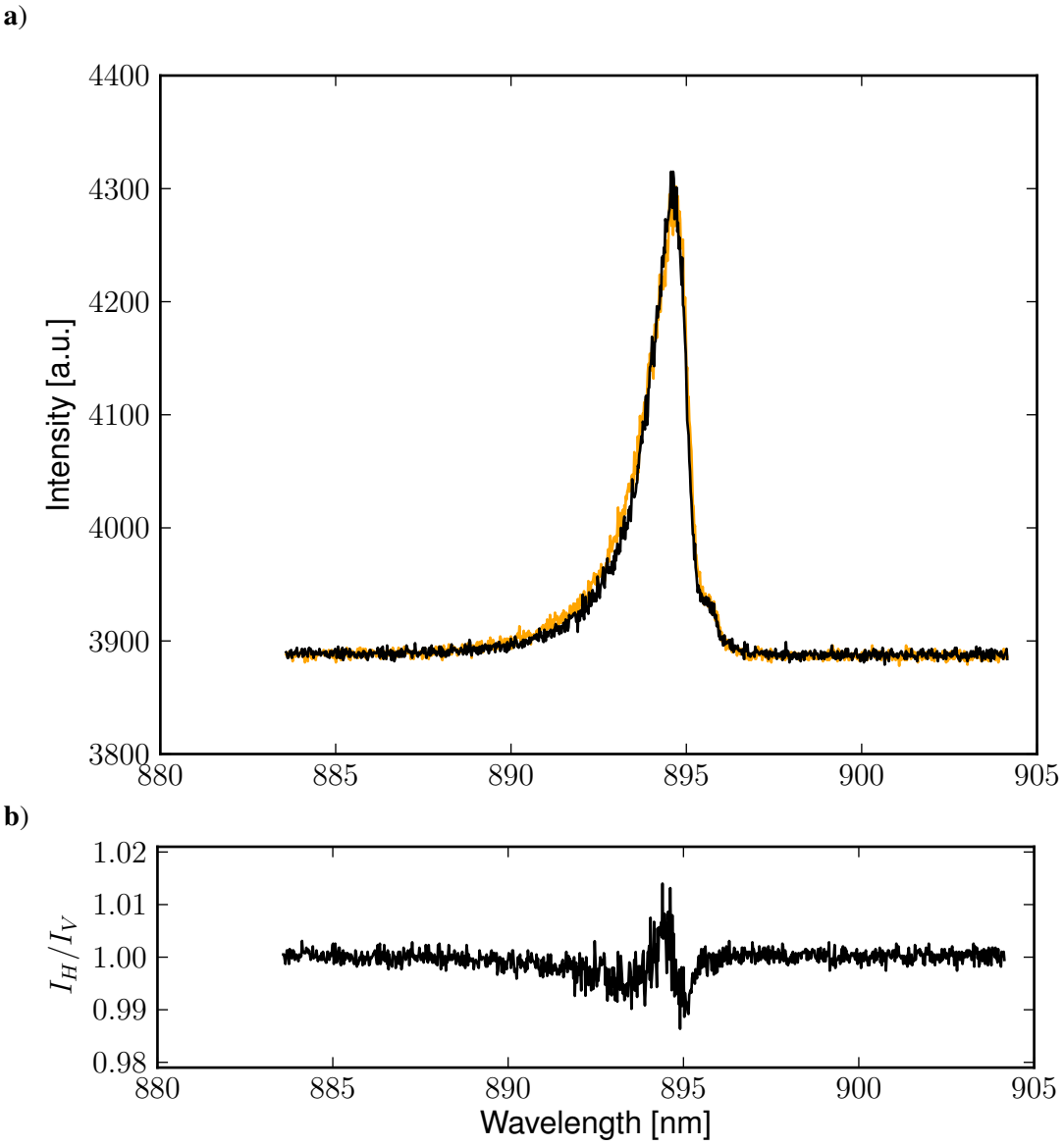


Figure 13.2.: a) Spectra of photons created in the first pass (horizontally polarized, orange, —) and the second pass through the non-linear crystal (vertically polarized, black, —). b) Comparison (ratio) of both spectra.

## 13.3. Optimal crystal length

To find the right compensation crystal length, a visibility measurement is performed in the $|L\rangle$ basis, as shown in the lower right panel of Fig. 13.3. For a certain wavelength pair $\lambda_{i/s}$, slabs of $YVO_4$ of different thickness are placed in the beam. By rotating one of the polarizers the signal is minimized (indicates $|\phi^+\rangle$). If properly done, a signal of zero indicates maximum fidelity. The maximum fidelity was found for a compensation crystal length of 153 mm. This coincides with the measured value of the refractive index of $YVO_4$ in [ST14]. For this pair of wavelength, other studies [ZLC+10] and specifications [Foc] fail to give the correct values for the compensation crystal by approximately 10 mm.

After verifying the crystal length for one pair of wavelengths, the compensation crystal length for all other pairs can be estimated. Adjusting this length by adding or removing crystal slabs or changing the compensation crystal temperature, allows for measuring the entanglement at different frequencies in future experiments.

## 13.4. Measuring entanglement

To measure the fidelity, the visibility of a single basis is measured (as discussed in Sec. 9.5). The visibility measurement and the sinusoidal fit is shown in Fig. 13.3 for different bases. The measured fidelity is $F_{\phi^+} = 0.753 \pm 0.021$ The value of $p$ is thus $p = 0.53$. The raw count rate at the signal APD is 300 000 cps. The quantum efficiency of the APD is 10%. Consequently, the corrected (actual) rate of created photons is $3 \cdot 10^6$ cps. This values was measured for 0.6 mW pump power. Which yields a brightness of 5 Mcps/mW. Compared to the theoretical possible pump rate of 61 Mcps/mW this is rather low (see [Kre15], where the rates for this setup are estimated using [Ben10]). However in preliminary measurements [Kre15] a brightness of 20 Mcps/mW was measured, before one of the fiber coupled APDs had to be temporarily replaced. This indicates that 80% of the signal was lost due to a less optimal coupling. Having a spectral width of $\Delta\lambda = 1.5$ nm, the spectral brightness is approximately 3.3 Mcps/(mW nm). Assuming a brightness of 20 Mcps/mW, the spectral brightness is 13.3 Mcps/(mW nm). In comparison to state-of-the-art sources (as compiled in [SRJ+13]) the corrected brightness (20 Mcps/mW) is of the same order of magnitude. The spectral width is comparable to other sources, however the non-linear crystal in this setup was much longer. Therefore the spectral brightness should exceed the other sources. This is not the case, because the focusing conditions

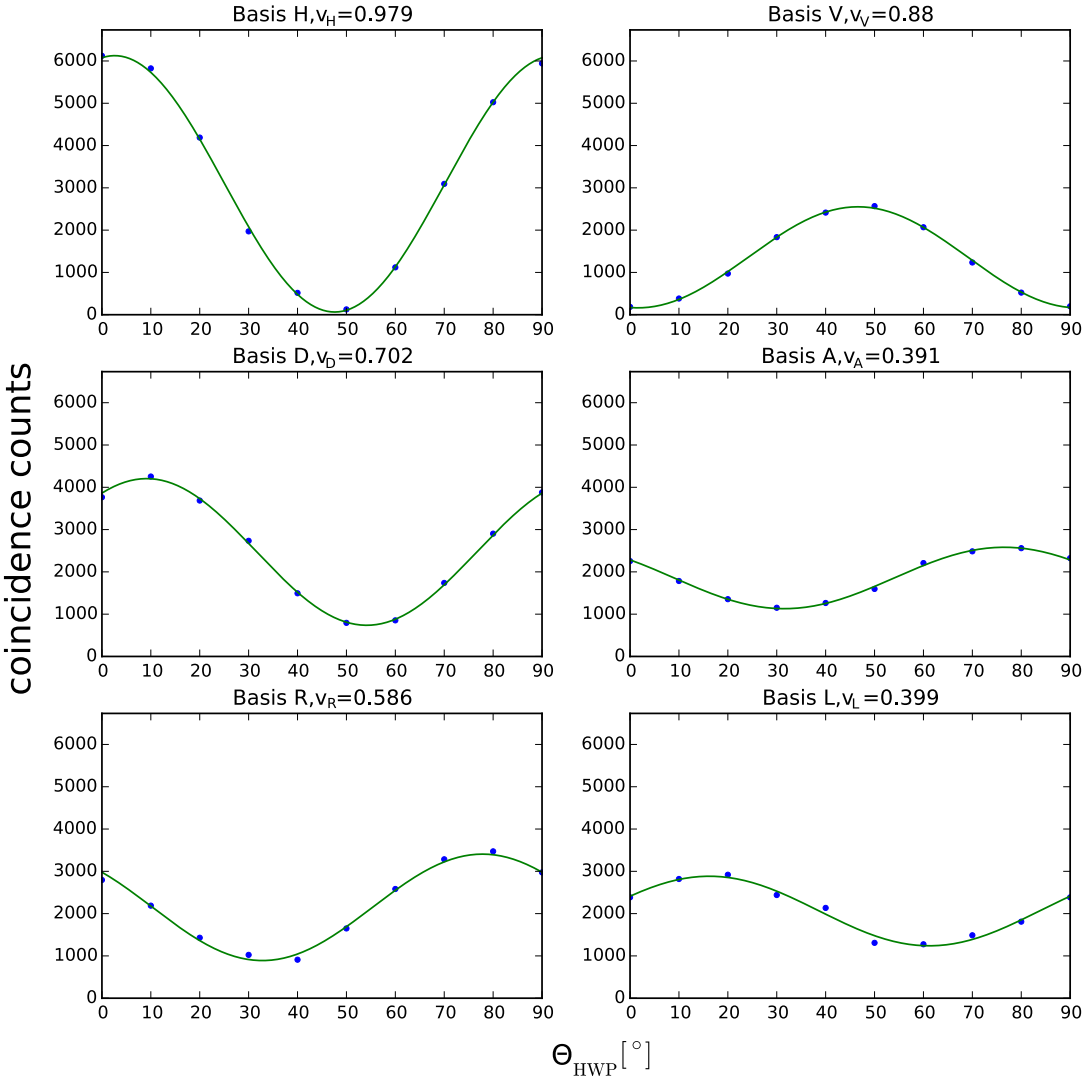


Figure 13.3.: Measured coincidence counts in different bases. The polarization in one arm is fixed, while the half-wave plate in the other arm is rotated by $\Theta_{HWP}$ (see Fig. 12.2). Compensation crystal length is 153 mm. The one-photon visibility is extracted from the sinusoidal fit, and indicated for each measurement as $v_i, i = \{H, V, D, R, L\}$. The resulting fidelity is $F = 0.753 \pm 0.021$.

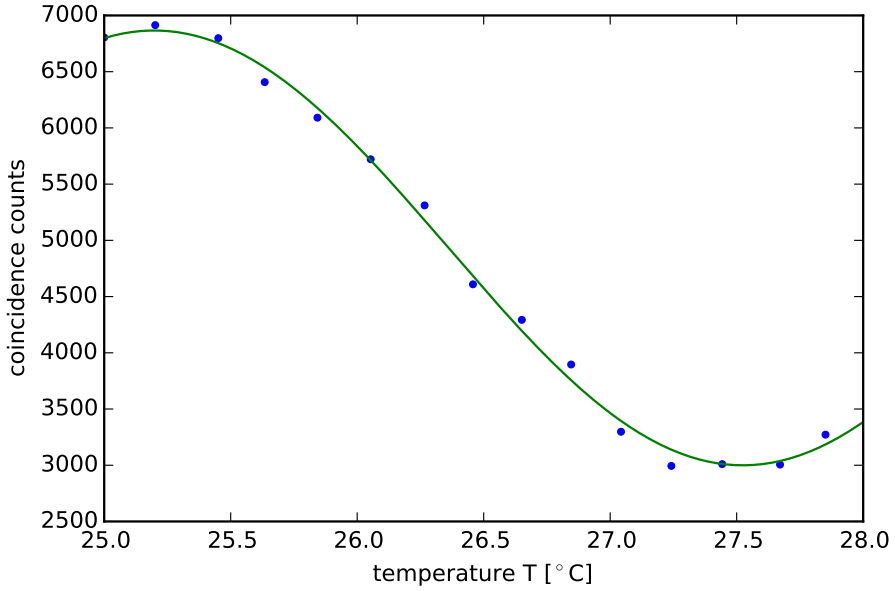


Figure 13.4.: Coincidence measurement in the diagonal basis $|AA\rangle$. The changes is the count rates indicates a change from the $\phi^+$ to the $\phi^-$ state.

were not fully optimized.

## 13.5. Flipping the Bell state

The phase $\phi$ in the Bell state Eq. (12.3.1) can be manipulated by changing the compensation crystal temperature. If the temperature changes, the difference in the refractive indices of both axes changes. This changes the phase factor between the first and the second pair. In this experiment 30 mm of the entire 153 mm of the compensation crystal are in placed in a tunable oven. Setting both detection polarizations to diagonal, i.e., basis $|AA\rangle$, the change in the coincidence counts can be tracked for changing temperatures. In Fig. 13.4 the transition from $\phi^+$ to $\phi^-$ is depicted for a temperature change of approximately 2.4° C.

# 14. Summary of Part II

In this part of the thesis, a novel scheme for creating entangled photon pairs was proposed, designed and demonstrated. This proof-of-principle experiment shows that the *geometrical* folded-sandwich is a suitable candidate for quantum interface applications. The setup extends its predecessor, the folded-sandwich [SRJ+13]. It is wavelength independent and therefore tunable. Its ability to create entangled photons has been demonstrated. The probability of entanglement is not yet as high as in other sources in the literature (see references in [SRJ+13]), but can further be increased by choosing different focusing parameters. Better focusing should also increase the brightness of the source.

Another issue is the temperature stability of the compensation crystal. Steinlechner et al. suggest that temperature stability of 0.1 K is needed to achieve fidelities as above 99.5% [SRJ+13]. In this experiment only 30 mm out of 153 mm compensation crystal were operated in an oven. The restricted oven length is due to the fact that the total length of the compensation crystal was not a priori clear. As mentioned in the introduction several studies reported very different values. Now that the exact length was experimentally verified, it turns out that only [ST14] makes valid predictions for this setup. With this knowledge a new oven can be designed that hosts all crystal slabs.

The source itself persuades by its simple, yet powerful design. Entangled photons are created with purely geometrical means.

# 15. Outlook of Part II

It is planned to use the folded-sandwich source of highly non-degenerate photons presented in this thesis as a quantum interface. This quantum interface could then teleport a flying qubit from a quantum dot at 894,3 nm to the telecom band at 1.3 μm. Besides the actual application of the source, the source itself can be further improved. At first the spectral width of the created photons can be further reduced. The possible spectral width for a 40 mm non-linear crystal is 0.5 nm at a wavelength of 894 nm (see diploma thesis for details [Mül15]) This can be achieved by choosing different focusing parameters. The focusing in the setup presented here was chosen relatively strong, for high pair creation rate. Focusing the beam less allows for a longer Rayleigh length. This means the beam is collimated over a longer range. Preferably the collimation should be (nearly) the same over the entire crystal length.

Furthermore, the visibility can be improved. In this setup the visibility is diminished due to slightly different paths in the first and in the second pass through the crystal. This problem might be solved when adjusting the beam width, as discussed above. If the beams are less tightly focused, differences in the focal position should have less effect.

Concerning the tunability, it is interesting to find a tunable dispersion compensation material. Right now, the crystal slabs have to be inserted or removed for every detuning of the source. Maybe liquid crystals, that are ac-driven, can be used to allow for automatic detuning.

# 16. Epilogue to Part I and II

In this thesis certain aspects of the linear and non-linear properties of light were investigated. The question tackled in Part I and Part II seem to be distant aspects of light. However, these two unrelated effects may be just different building blocks used in future optical system.

In Part I, the influence of boundary corrugation was investigated. Boundary corrugations are often used to influence transmission in integrated optical devices. They are equally important for in- and outcoupling applications. In this thesis it was shown that the Square Gradient Bragg scattering effect appears in dielectric waveguides. The theoretical derivation in the coupled mode framework put this effects of curvature of corrugated boundaries on solid theoretical grounds. The numerical calculations presented here help to pave the way for proof-of-principle experiments. These experiments will be another step, before the Square Gradient Bragg scattering mechanism can be successfully applied in integrated optical devices.

In Part II the non-linear effect in a crystal were used to generate photon pairs. The non-linear crystal was set up in the so called folded-sandwich configuration to yield entangled photons. Here the folded-sandwich configuration was enhanced by making the polarization rotation wavelength independent. This enhanced *geometrical* folded-sandwich is able to yield photons at strongly different wavelength. Furthermore, since the setup is wavelength independent the created pairs are tunable over a broad range of wavelength. In this proof-of-principle experiment it was shown that the setup created entangled photons with a fidelity of above 75%. The highly non-degenerate photons and the tunability makes this setup a possible candidate for application in hybrid quantum architectures.

# Part III.

# Bibliography

# Bibliography

[AD82] A. Aspect and J. Dalibard. “Experimental test of Bell’s inequalities using time-varying analyzers”. In: *Physical review letters* 49.25 (1982).

[And58] P. W. Anderson. “Absence of Diffusion in Certain Random Lattices”. In: *Physical Review* 109.5 (1958), pp. 1492–1505. DOI: 10.1103/PhysRev.109.1492.

[BB13] W. H. Bragg and W. L. Bragg. “The Reflection of X-rays by Crystals”. In: *Proceedings of the Royal Society of London A: Mathematical, Physical and Engineering Sciences* 88.605 (July 1913), pp. 428–438. DOI: 10.1098/rspa.1913.0040.

[BBC93] C. H. Bennett, G. Brassard, and C. Crépeau. “Teleporting an unknown quantum state via dual classical and Einstein-Podolsky-Rosen channels”. In: *Physical Review Letters* 70.13 (1993).

[Bee97] C. W. J. Beenakker. “Random-matrix theory of quantum transport”. In: *Reviews of Modern Physics* 69.3 (July 1997), pp. 731–808. DOI: 10.1103/RevModPhys.69.731.

[Ben10] R. S. Bennink. “Optimal collinear Gaussian beams for spontaneous parametric down-conversion”. In: *Physical Review A* 81.5 (2010), p. 053805. DOI: 10.1103/PhysRevA.81.053805.

[Boy03] R. W. Boyd. *Nonlinear Optics*. Academic Press, 2003.

[BYR+13] M. Benyoucef, M. Yacob, J. P. Reithmaier, J. Kettler, and P. Michler. “Telecom-wavelength (1.5 μm) single-photon emission from InP-based quantum dots”. In: *Applied Physics Letters* 103.16 (Oct. 2013), p. 162101. DOI: 10.1063/1.4825106.

[DKHH+12] O. Dietz, U. Kuhl, J. C. Hernández-Herrejón, and L. Tessieri. “Transmission in waveguides with compositional and structural disorder: experimental effects of disorder cross-correlations”. In: *New Journal of Physics* 14.1 (Jan. 2012), p. 013048. DOI: 10.1088/1367-2630/14/1/013048.

[DKN+15] O. Dietz, G. Kewes, O. Neitzke, and O. Benson. “Coupled mode approach to square gradient Bragg reflection resonances in corrugated dielectric waveguides”. In: *arXiv: 1506.01206* (June 2015). Accepted for publication in Physical Review A.

[DKS+10] O. Dietz, U. Kuhl, H.-J. Stöckmann, F. M. Izrailev, and N. M. Makarov. “Transport in Quasi-One Dimensional Correlated Random Media”. In: *Mesoscopic Physics in Complex Media* 03010 (2010), p. 03010. DOI: 10.1051/iesc/2010mpcm03010.

[DKS+11] O. Dietz, U. Kuhl, H.-J. Stöckmann, N. M. Makarov, and F. M. Izrailev. “Microwave realization of quasi-one-dimensional systems with correlated disorder”. In: *Physical Review B* 83.13 (Apr. 2011), p. 134203. DOI: 10.1103/PhysRevB.83.134203.

[DMBF+14] J. Doppler, J. A. Méndez-Bermúdez, J. Feist, O. Dietz, D. O. Krimer, N. M. Makarov, F. M. Izrailev, and S. Rotter. “Reflection resonances in surface-disordered waveguides: strong higher-order effects of the disorder”. In: *New Journal of Physics* 16.5 (May 2014), p. 053026. DOI: 10.1088/1367-2630/16/5/053026.

[DMK+15] O. Dietz, C. Müller, T. Kreißl, U. Herzog, T. Kroh, A. Ahlrichs, and O. Benson. “A folded-sandwich polarization-entangled two-color photon pair source with large tuning capability for applications in hybrid quantum architectures”. In: *arXiv: 1507.03370* (July 2015). Accepted for publication in Applied Physics B.

[DSK+12] O. Dietz, H.-J. Stöckmann, U. Kuhl, F. M. Izrailev, N. M. Makarov, J. Doppler, F. Libisch, and S. Rotter. “Surface scattering and band gaps in rough waveguides and nanowires”. In: *Physical Review B* 86.20 (Nov. 2012), p. 201106. DOI: 10.1103/PhysRevB.86.201106.

[Duf01] D. G. Duffy. *Green’s Functions with Applications*. CRC Press, May 2001.

[Ebe92] K. J. Ebeling. *Integrierte Optoelektronik: Wellenleiteroptik, Photonik, Halbleiter*. German. Berlin: Springer, 1992.

[FKS+74] D. C. Flanders, H. Kogelnik, R. V. Schmidt, and C. V. Shank. “Grating filters for thin-film optical waveguides”. In: *Applied Physics Letters* 24.4 (Feb. 1974), pp. 194–196. DOI: 10.1063/1.1655150.

[FNM+07] G. Fujii, N. Namekata, M. Motoya, S. Kurimura, and S. Inoue. "Bright narrowband source of photon pairs at optical telecommunication wavelengths using a type-II periodically poled lithium niobate waveguide". In: *Optics express* 15.20 (2007), pp. 12769–12776.

[HHP+09] M. Hentschel, H. Hübel, A. Poppe, and A. Zeilinger. "Three-color Sagnac source of polarization-entangled photon pairs". In: *Optics express* 17.25 (2009), pp. 23153–23159.

[IMR06] F. M. Izrailev, N. M. Makarov, and M. Rendón. "Manifestation of the roughness-square-gradient scattering in surface-corrugated waveguides". In: *Physical Review B* 73.15 (Apr. 2006), p. 155421. DOI: 10.1103/PhysRevB.73.155421.

[Joh87] S. John. "Strong localization of photons in certain disordered dielectric superlattices". In: *Physical Review Letters* 58.23 (June 1987), pp. 2486–2489. DOI: 10.1103/PhysRevLett.58.2486.

[Joh91] S. John. "Localization of light". In: *Phys. Today* 44.5 (1991), pp. 32–40.

[KDH+04] M. Kroutvar, Y. Ducommun, D. Heiss, M. Bichler, D. Schuh, G. Abstreiter, and J. J. Finley. "Optically programmable electron spin memory using semiconductor quantum dots". In: *Nature* 432.7013 (Nov. 2004), pp. 81–84. DOI: 10.1038/nature03008.

[KFK+14] S. Karbasi, R. J. Frazier, K. W. Koch, T. Hawkins, J. Ballato, and A. Mafi. "Image transport through a disordered optical fibre mediated by transverse Anderson localization". In: *Nature Communications* 5 (Feb. 2014). DOI: 10.1038/ncomms4362.

[KFW06] T. Kim, M. Fiorentino, and F. N. C. Wong. "Phase-stable source of polarization-entangled photons using a polarization Sagnac interferometer". In: *Physical Review A* 73.1 (Jan. 2006). DOI: 10.1103/PhysRevA.73.012316.

[KMW+95] P. G. Kwiat, K. Mattle, H. Weinfurter, A. Zeilinger, A. V. Sergienko, and Y. Shih. "New High-Intensity Source of Polarization-Entangled Photon Pairs". In: *Physical Review Letters* 75.24 (1995), pp. 4337–4341. DOI: 10.1103/PhysRevLett.75.4337.

[Kog75] H. Kogelnik. “2. Theory of dielectric waveguides”. In: *Integrated Optics*. Topics in Applied Physics 7. Springer Berlin Heidelberg, Jan. 1975, pp. 13–81.

[Kre15] T. Kreißl. “Erzeugung von Zwei-Farben-Polarisationsverschränkung mit einem nichtlinearen Kristall in Folded Sandwich Geometrie”. Diplomarbeit. Humboldt-Universität zu Berlin, 2015.

[KS72] H. Kogelnik and C. V. Shank. “Coupled-Wave Theory of Distributed Feedback Lasers”. In: *Journal of Applied Physics* 43.5 (May 1972), pp. 2327–2335. DOI: 10.1063/1.1661499.

[KSM+15] G. Kewes, M. Schoengen, G. Mazzamuto, O. Neitzke, R.-S. Schönfeld, A. W. Schell, J. Probst, J. Wolters, B. Löchel, C. Toninelli, and O. Benson. “Key components for nano-assembled plasmon-excited single molecule non-linear devices”. In: *arXiv:1501.04788 [physics]* (Jan. 2015). arXiv: 1501.04788.

[LZD+14] S. Lavdas, S. Zhao, J. B. Driscoll, R. R. Grote, R. M. Osgood, and N. C. Panoiu. “Wavelength conversion and parametric amplification of optical pulses via quasi-phase-matched FWM in long-period Bragg silicon waveguides”. In: *Optics Letters* 39.13 (July 2014). arXiv: 1405.7434, p. 4017. DOI: 10.1364/OL.39.004017.

[Mül15] C. Müller. “Two-color entangled photon pair source”. Master’s Thesis. Humboldt-Universität zu Berlin, 2015.

[Pan55] S. Pancharatnam. “Achromatic combinations of birefringent plates. Part I. An achromatic circular polarizer”. In: *Proceedings of the Indian Academy of Sciences, Section A*. Vol. 41. Indian Academy of Sciences, 1955, pp. 130–136.

[RIM07] M. Rendón, F. Izrailev, and N. Makarov. “Square-gradient mechanism of surface scattering in quasi-one-dimensional rough waveguides”. In: *Physical Review B* 75.20 (2007). DOI: 10.1103/PhysRevB.75.205404.

[RM12] M. Rendón and N. M. Makarov. “Discrimination of surface-scattering mechanisms in waveguides with a rough boundary of rectangular power spectrum”. In: *physica status solidi (c)* 9.6 (June 2012), pp. 1507–1514. DOI: 10.1002/pssc.201100708.

[RMI11] M. Rendón, N. Makarov, and F. Izrailev. "Ballistic, diffusive, and localized transport in surface-disordered systems: Two-mode waveguide". In: *Physical Review E* 83.5 (2011), pp. 1–15. DOI: 10.1103/PhysRevE.83.051124.

[SKH+11] G. A. Steudle, S. Knauer, U. Herzog, E. Stock, V. A. Haisler, D. Bimberg, and O. Benson. "Experimental optimal maximum-confidence discrimination and optimal unambiguous discrimination of two mixed single-photon states". In: *Physical Review A* 83.5 (2011), p. 050304. DOI: 10.1103/PhysRevA.83.050304.

[SRJ+13] F. Steinlechner, S. Ramelow, M. Jofre, M. Gilaberte, T. Jennewein, M. W. Mitchell, V. Pruneri, and J. P. Torres. "Phase-stable source of polarization-entangled photons in a linear double-pass configuration". In: *Optics Express* 21.10 (2013), p. 11943. DOI: 10.1364/OE.21.011943.

[SSB+13] T. E. Stuart, J. A. Slater, F. Bussières, and W. Tittel. "Flexible source of nondegenerate entangled photons based on a two-crystal Sagnac interferometer". In: *Physical Review A* 88.1 (July 2013). DOI: 10.1103/PhysRevA.88.012301.

[ST04] B.-S. Shi and A. Tomita. "Generation of a pulsed polarization entangled photon pair using a Sagnac interferometer". In: *Physical Review A* 69.1 (Jan. 2004), p. 013803. DOI: 10.1103/PhysRevA.69.013803.

[ST14] Y. Sato and T. Taira. "Highly accurate interferometric evaluation of thermal expansion and dn/dT of optical materials". In: *Optical Materials Express* 4.5 (2014), pp. 876–888. DOI: 10.1364/OME.4.000876.

[Stö10] H.-J. Stöckmann. "Microwave billiards and quantum chaos". In: *Scholarpedia* 5.10 (2010), p. 10243. DOI: 10.4249/scholarpedia.10243.

[TC95] C. L. Tang and L. K. Cheng. *Fundamentals of Optical Parametric Processes and Oscillations*. Amsterdam: Harwood Academic Press, Mar. 1995.

[TH00] B. M. Terhal and P. Horodecki. "Schmidt number for density matrices". In: *Physical Review A* 61.4 (2000), p. 040301. DOI: 10.1103/PhysRevA.61.040301.

[TIS+08] D. T. H. Tan, K. Ikeda, R. E. Saperstein, B. Slutsky, and Y. Fainman. "Chip-scale dispersion engineering using chirped vertical gratings". In: *Optics letters* 33.24 (2008), pp. 3013–3015.

[TW08] P. Trojek and H. Weinfurter. "Collinear source of polarization-entangled photon pairs at nondegenerate wavelengths". In: *Applied Physics Letters* 92.21 (May 2008), p. 211103. DOI: 10.1063/1.2924280.

[TZO+12] R. Trotta, E. Zallo, C. Ortix, P. Atkinson, J. Plumhof, J. van den Brink, A. Rastelli, and O. Schmidt. "Universal Recovery of the Energy-Level Degeneracy of Bright Excitons in InGaAs Quantum Dots without a Structure Symmetry". In: *Physical Review Letters* 109.14 (2012), p. 147401. DOI: 10.1103/PhysRevLett.109.147401.

[Wei] E. W. Weisstein. *Wiener-Khinchin Theorem*. From MathWorld–A Wolfram Web Resource.

[WGP+07] A. G. White, A. Gilchrist, G. J. Pryde, J. L. O'Brien, M. J. Bremner, and N. K. Langford. "Measuring two-qubit gates". In: *JOSA B* 24.2 (2007), pp. 172–183.

[WR90] K. A. Winick and J. Roman. "Design of corrugated waveguide filters by Fourier-transform techniques". In: *IEEE Journal of Quantum Electronics* 26.11 (Nov. 1990), pp. 1918–1929. DOI: 10.1109/3.62111.

[WYL+13] J.-Y. Wang, B. Yang, S.-K. Liao, L. Zhang, Q. Shen, X.-F. Hu, J.-C. Wu, S.-J. Yang, H. Jiang, Y.-L. Tang, B. Zhong, H. Liang, W.-Y. Liu, Y.-H. Hu, Y.-M. Huang, B. Qi, J.-G. Ren, G.-S. Pan, J. Yin, J.-J. Jia, Y.-A. Chen, K. Chen, C.-Z. Peng, and J.-W. Pan. "Direct and full-scale experimental verifications towards ground-satellite quantum key distribution". In: *Nature Photonics* 7.5 (2013), pp. 387–393. DOI: 10.1038/nphoton.2013.89.

[YHF13] W.-B. Yan, J.-F. Huang, and H. Fan. "Tunable single-photon frequency conversion in a Sagnac interferometer". In: *Scientific Reports* 3 (2013). DOI: 10.1038/srep03555.

[YY03] A. Yariv and P. Yeh. *Optical waves in crystals: propagation and control of laser radiation*. Hoboken, N.J.: John Wiley and Sons, 2003.

[ZLC+10] D. E. Zelmon, J. J. Lee, K. M. Currin, J. M. Northridge, and D. Perlov. "Revisiting the optical properties of Nd doped yttrium orthovanadate". In: *Applied optics* 49.4 (2010), pp. 644–647.

[Ale] Alexander Franzen. *ComponentLibrary: a free vector graphics library for optics. Licensed under a Creative Commons Attribution-NonCommercial 3.0 Unported License.*

[Foc] Foctek Photonics, Inc. *Product Specification YVO4*. foctek.net/products/YVO4.htm.

# Part IV.

# Appendix

# 17. List of own publications

## Publications related to this thesis

- O. Dietz, C. Müller, T. Kreißl, et al. “A folded-sandwich polarization-entangled two-color photon pair source with large tuning capability for applications in hybrid quantum architectures”. In: *arXiv: 1507.03370* (July 2015). Accepted for publication in Applied Physics B, cited as [DMK+15]

- O. Dietz, G. Kewes, O. Neitzke, et al. “Coupled mode approach to square gradient Bragg reflection resonances in corrugated dielectric waveguides”. In: *arXiv: 1506.01206* (June 2015). Accepted for publication in Physical Review A, cited as [DKN+15]

- J. Doppler, J. A. Méndez-Bermúdez, J. Feist, et al. “Reflection resonances in surface-disordered waveguides: strong higher-order effects of the disorder”. In: *New Journal of Physics* 16.5 (May 2014), p. 053026. DOI: 10.1088/1367-2630/16/5/053026, cited as [DMBF+14]

- O. Dietz, H.-J. Stöckmann, U. Kuhl, et al. “Surface scattering and band gaps in rough waveguides and nanowires”. In: *Physical Review B* 86.20 (Nov. 2012), p. 201106. DOI: 10.1103/PhysRevB.86.201106, cited as [DSK+12]

## Earlier publications – not related to this thesis

- O. Dietz, U. Kuhl, J. C. Hernández-Herrejón, et al. “Transmission in waveguides with compositional and structural disorder: experimental effects of disorder cross-correlations”. In: *New Journal of Physics* 14.1 (Jan. 2012), p. 013048. DOI: 10.1088/1367-2630/14/1/013048 cited as [DKHH+12]

- O. Dietz, U. Kuhl, H.-J. Stöckmann, et al. “Microwave realization of quasi-one-dimensional systems with correlated disorder”. In: *Physical Review B* 83.13 (Apr. 2011), p. 134203. DOI: 10.1103/PhysRevB.83.134203 cited as [DKS+11]

- O. Dietz, U. Kuhl, H.-J. Stöckmann, et al. “Transport in Quasi-One Dimensional Correlated Random Media”. In: *Mesoscopic Physics in Complex Media* 03010 (2010), p. 03010. DOI: 10.1051/iesc/2010mpcm03010 cited as [DKS+10]

# 18. Acknowledgements

I'd like to thank Stefan Rotter for his exceptional hospitality during my stay in Vienna. Discussions with Stefan were the source of numerous ideas. His remarks on my research have been important guidelines during the last 5 years. The stay at University of Vienna would not be the same without the collaboration with Jörg Doppler. Jörg did not only provide valuable backup when referees went wild. He ensured that I remember Vienna not only as a scientific but as a cultural hot spot as well.

While in Vienna, I had the opportunity to meet Amir Moqanaki at VCQ. He shared his vast knowledge of non-linear optics with me and introduced me to the art of entanglement creation. He did not miss to end his 3-days private lecture with an appropriate after-hour tour through Vienna. After being introduced to non-linear optics, Fabian Steinlechner and Sven Ramelow took plenty of time to discuss the new design of the folded sandwich source, presented in this work. The idea of creating a geometrical folded sandwich came up during such a thrilling discussion. In the aftermath of my visit, they both continued their support throughout the time I spent working on that project.

In Berlin, I enjoyed the support of a team of smart and committed students, Tim Kroh (Master 2012), Chris Müller (Bachelor 2013, Master 2015), Moritz Stange (Bachelor 2014) and Thomas Kreißl (Diploma 2015). Ulrike Herzog helped me to solve some tricky theoretical problems. And when the problems I was facing were not as tricky as I suspected, she managed to explain them to me, in a very friendly and instructive manner. Thank you, Ulrike. I am especially indebted to Günter Kewes who helped me continuously with my research on dielectric waveguides. He not only performed the numerical simulations, more importantly, he took plenty of time to discuss, encourage and even guide my work. I am grateful to my colleagues here at the Institute of Physics, the Nanos, QOMs, and TOPs, who made this just a great time. I am especially endebted to Alexander Kuhlicke, Ben Sprenger, Oliver Neitzke, Andreas Ahlrichs, Nikola Sadzak, Tim Kroh, Simon Schönfeld, Gesine Steudle, Matthias Leifgen, Klaus Palis, Regina Rheinländer, Achim Peters, Christian Freier, Moritz Nagel, Matthias Moeferdt, Dan-Nha Huynh, Rogelio Rodriguez-Oliveros and Kurt Busch.

And last but not least, I'd like to thank my thesis adviser Oliver Benson. Oliver gave me incomparable freedom to pursue my research. He enabled me to think about problems that were originally not on our road map. He encouraged the development of my own ideas. Besides that scientific patronage, I am grateful how he encouraged and supported my paternal leaves.

# 19. Selbständigkeitserklärung

Ich erkläre, dass ich die vorliegende Arbeit selbständig angefertigt habe und alle wichtigen Quellen, Literatur und Hilfsmittel angegeben habe.

Berlin, den _____ _____

Otto Dietz